The role of protein dielectric relaxation on modulating the electron transfer process in photosynthetic reaction centers

by

Zhi Guo

A Dissertation Presented in Partial Fulfillment
of the Requirements for the Degree
Doctor of Philosophy

Approved May 2012 by the
Graduate Supervisory Committee:

Neal W. Woodbury, Chair
Stuart M. Lindsay
Robert Ros
Banu S. Ozkan
Thomas A. Moore

ARIZONA STATE UNIVERSITY

December 2012

ABSTRACT

The photosynthetic reaction center is a type of pigment-protein complex found widely in photosynthetic bacteria, algae and higher plants. Its function is to convert the energy of sunlight into a chemical form that can be used to support other life processes. The high efficiency and structural simplicity make the bacterial reaction center a paradigm for studying electron transfer in biomolecules. This thesis starts with a comparison of the primary electron transfer process in the reaction centers from the *Rhodobacter shperoides* bacterium and those from its thermophilic homolog, *Chloroflexus aurantiacus*. Different temperature dependences in the primary electron transfer were found in these two type of reaction centers. Analyses of the structural differences between these two proteins suggested that the excess surface charged amino acids as well as a larger solvent exposure area in the *Chloroflexus aurantiacus* reaction center could explain the different temperature depenence. The conclusion from this work is that the electrostatic interaction potentially has a major effect on the electron transfer. Inspired by these results, a single point mutant was designed for *Rhodobacter shperoides* reaction centers by placing an ionizable amino acid in the protein interior to perturb the dielectrics. The ionizable group in the mutation site largely deprotonated in the ground state judging from the cofactor absorption spectra as a function of pH. By contrast, a fast charge recombination assoicated with protein dielectric relaxation was observed in this mutant, suggesting the possibility that dynamic protonation/deprotonation may be taking place during the electron transfer. The fast protein dielectric relaxation occuring in this mutant

complicates the electron transfer pathway and reduces the yield of electron transfer to Q_A. Considering the importance of the protein dielectric environment, efforts have been made in quantifying variations of the internal field during charge separation. An analysis protocol based on the Stark effect of reaction center cofactor spectra during charge separation has been developed to characterize the charge-separated radical field acting on probe chromophores. The field change, monitored by the dynamic Stark shift, correlates with, but is not identical to, the electron transfer kinetics. The dynamic Stark shift results have lead to a dynamic model for the time-dependent dielectric that is complementary to the static dielectric asymmetry observed in past steady state experiments.

Taken together, the work in this thesis emphasizes the importance of protein electrostatics and its dielectric response to electron transfer.

DEDICATION

Dedicated to my family, for their love.

ACKNOWLEDGMENTS

I am greatly indebted to my PhD. Advisor, Dr. Neal Woodbury, a man with amazing leadership charisma, strong academic capability, and a nice personality. In the past five years, you provided me the best you can gave without any reservations. I received financial aids from you so that I could focus on research; I enjoyed the freedom you gave to me to try and explore new things. You tried all you could to teach me how to do research, how to write, and amused me with the anecdotes about those photosynthesis people. There is much more that I cannot put here because I have to leave space for others.

Dr. Su Lin, you introduced me into this group, and I am so lucky to have you as my “co-PI”. Without your warm support for all these years, I would never have been able to get through. You kept the laser running; you communicated with other research groups to help me get the samples; you spent innumerable office hours to discuss with me for these five years; you read and revised the papers for me. Thank you!

There are many other people that I need to acknowledge here. Dr. Haiyu Wang taught me how to do laser experiments hand-by-hand; Dr. Yueyong Xin and Prof. Blankenship provided me the samples for one of my work; Carole used to organize everything in the lab, and she also read and revised my papers for so many times; Thanks to Dr. Jie Pan and Christa for teaching me the site-directed mutagenesis technique; Thanks to Prof. Banu Ozkan and Prof. Dmitry Matryushov for helpful discussions in the reaction center project during my first few years, it is regretful that I was not able to keep a good balance between

experiment and theory to make more achievements; and thanks to all Woodbury lab members, Wei, Risa, and Dr. Fu Jinglin, for their support.

Lastly, my family has always been my ultimate driving force to fight for my future. I know they will always be there no matter if I am a winner or a loser.

TABLE OF CONTENTS

Page

CHAPTER Page

LIST OF TABLES

LIST OF FIGURES

Figure Page

Figure Page

Figure Page

Figure Page

PREFACE

Photosynthesis is a research field with a long history. Quantitative mechanistic research dates back to the 1930s. After all these years' development, it has grown and diverged into many sub branches. Many scientists have joint forces in this research; at the very beginning it was biologists, then chemists and physicists. This field has proven to be very productive, on both the science side and the engineering side. On the science part, and more specifically, in the contribution of physics, electron transfer and energy transfer associated with photosynthesis are clearly very important. At least two Nobel prizes are directly associated with photosynthetic electron transfer. In part, the significance is due to interface with electron transfer and because this reaction occurs in condensed phase, which are both very active fields. When the laser technology advanced into the femtosecond era, more bottom level information of the reactions was revealed. The application of this to the bacterial reaction center as a model system, promised to benefit the understanding of a large class of phenomena and give birth to new concepts and potential applications.

This thesis is a summary of the author's PhD work, focusing on the photosynthetic electron transfer process in the bacterial reaction center, with particular emphasis on the coupling of electron transfer to the dynamic protein environment. The experimental tools that are used to study this problem are basically spectroscopic techniques, assisted by some rudimentary computer simulation and modeling. The organization of this thesis is as follows:

In Chapter 1, basic knowledge and concepts of the structure and function of the bacterial reaction center and its chromophores are presented first. This is followed by a short survey on the principle of the spectroscopic technique that is used in the next chapters. Using the reaction center as an example, a concise description is given on the interpretation of photochemistry events using transient absorption spectroscopic data. Also as a technological review, some of the molecular modeling techniques associated with the reaction center system modeling is covered.

In Chapter 2, a temperature dependent study of the primary electron transfer after light excitation in a thermophilic bacterial reaction center from *Chloroflexus aurantiacus*, is presented. By comparing reaction centers of *Chloroflexus aurantiacus* with its mesophilic homolog, *Rhodobacter sphaeroides* (a well-studied bacterial strain in past decades), the possibility that the surface charges and the solvent effects could actually influence the electron transfer, particularly on longer time scale, is discussed.

In Chapter 3, the concept that protein dielectric relaxation is coupled to electron transfer pathways has been tested by placing an ionizable group inside the protein. The site-directed mutagenesis potentially perturbs the dielectric response of the protein by localizing a charge in that site.

In Chapter 4, an analysis protocol is developed to achieve some information about the time dependent internal field change elicited by charge separation in the reaction center. The variation of internal field may provide some information on the protein dielectric relaxation during the electron transfer.

In Chapter 5, preliminary trials on applying transient circular dichroism spectroscopy to the study of electron transfer in reaction centers have been described. In the end, a summary of the Marcus electron transfer theory in the reaction center protein is presented.

It is hopeful the work come out from this thesis provides some insight into the design of an artificial electron transfer system. The mimic of natural photosynthesis focuses on optimizing the energetic parameters of driving force and electronic coupling, but not reorganization energy. The reorganization energy is considerable influenced by the electrostatic interactions on the flexible protein structure, which possibly provides a new perspective to this topic.

CHAPTER 1

Introduction and background information

1 Light absorbing pigments in bacterial reaction centers

Chlorophylls have long been recognized as the photosynthetic pigments that play a crucial role in the energy production of higher plants. Their structure is very similiar to that of the porphyrins and their derivatives.

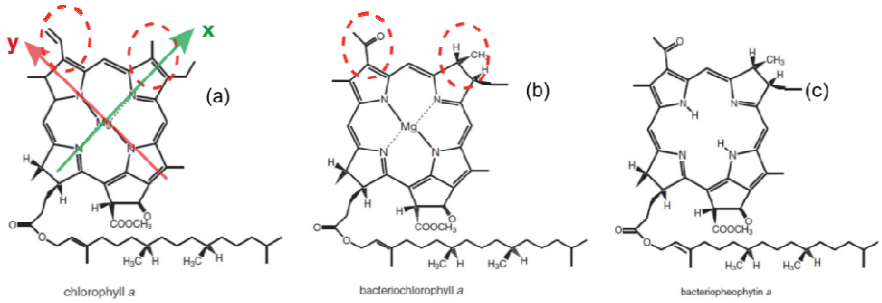

Figure 1: Molecular structures for (a) Chlorophyll-*a*, (b) Bacteiochlorophyll-*a*, and (c) Bacteriopheophytin-*a*; The arrows indicate two orthogonal molecular axes, x (green) and y (red). The red broken circles highlight where functional groups attached to the macrocycle ring to form chlorophyll derivatives.

Chlorophyll-*a* structure includes a cube-like macrocycle ring, about 10 angstroms in length on each side (Figure 1a). While the porphyrin structure features an iron atom in the center of its macrocycle ring, chlorophyll has a magnesium atom in the center, surrounded by four nitrogen atoms. Two molecular axes, **x** and **y,** define the geometry of a chlorophyll molecule's macrocycle ring. The axes are defined by the linear relationship of two sets of diagonal nitrogen atoms relative to the magnesium atom at the center. A long saturated hydrocarbon tail, referred to as the phytyl tail, is attached to the macrocycle ring. The phytyl tail can have multiple degrees of freedom as a result of rotation associated with its single bond

attachment to the macrocycle ring. In different types of bacterial photosynthetic reaction center crystal structures, as well as in the light-harvesting reaction centers of higher plants, the chlorophyll-*a* and its derivatives can take different forms based on the bending its phytyl tail[1-4]. The phytyl tail is beneficial to the assembly of the porphyrin ring within the photosynthetic proteins, which act as scaffolding for the porphyrin plane on the geometry level[5] and exert certain function in electron transfer[6]. Chlorophylls are the major light-absorbing pigments in higher plants, while in bacterial photosynthetic reaction centers, the light absorbing pigments are called bacteriochlorophylls (BChl). Bacteriochlorophyll-*a* (Figure 1b) is structurally different from chlorophyll-*a* because it has an acetyl group at the C-3 position in the macrocycle ring and a single bond between the C-7 and C-8 positions, as opposed to the C7/C-8 double bond found in chlorophyll-*a*. The chlorophyll-*a* has the lowest transition in its absorption spectrum at around 660 nm, whereas in bacteriochlorophyll this is shifted by 100 nm to the red ($660 \rightarrow$ 760 nm) as a result of those structural differences. Another light absorbing pigment in the bacterial reaction center is the bacteriopheophytin (Bphe), figure 1c, which has two protons connected to the nitrogen atoms along the y axis that take the place of the central magnesium ion found in chlorophyll. Additionally, carotenoids are also important light absorbing pigments in the reaction center and light harvesting antenna complex, but they will only be briefly mentioned in this paper since they are not cofactors that are directly associated with electron transfer.

2 The photosynthetic reaction center

The photosynthetic reaction center (RC), found in both higher plants and bacteria, is a unique photovoltaic device because it acts as the starting point for light energy to chemical energy conversion reaction, which is essentially the foundation for all organic matter. The reaction center is highly optimized for quantum efficiency in charge separation. This has been demonstrated in the wild type reaction center which produces nearly unit one quantum yield[7], although the mechanism behind this high quantum yield is not completely understood, particularly in terms of its robustness.

Reaction centers in bacteria are surrounded by a ring of antenna complex, called LH1. The accessory anttenna complex known as LH2 does not contain reaction center protein and is located nearby the LH1 complex. These two apparatus consititute an integral membrane antenna complex in the membranes of bacterial cells. In contrast, the reaction centers in higher plants and algae are embedded in a super complex known as Photosystem 1 (PSI+LHCI) or Photosystem 2 (PSII+LHCII), which also include many other photosynthetic proteins and subunits. The first reaction center complex was isolated in the purple bacterium *Rhodobacter (Rb.) sphaeroides* by Reed and Clayton in 1968. The D1-D2-cytochrome b-559 reaction center complex in PSII from spinach was subsequently isolated with success[8], but there is currently no reliable report on isolating individual reaction center of PSI. The PSII reaction center has a unique capability of oxidizing H_2O to O_2 as a result of the strong oxidizing capability of the chlorophyll-pair radical $P680^+$. Compared with higher plants, the reaction center

in bacteria is often used as a typical model for studying the electron transfer mechanism between chromophores because of its structural simplicity. Bacterial reaction centers normally incorporate no more than three subunits if the electron donor cytochrome is excluded. In addition to the primary sequences, the structure of the reaction center can vary among species. For example, in *Rb. sphaeroides*, which is a purple non-sulfur bacterium, the reaction center has three subunits[9] (see figure 2), but in *Chloroflexus (Cf.) aurantiacus*, a green non-sulfur bacterium, the reaction center has only two subunits[10] (see Chapter 2). The following section will discuss structural arrangements of the reaction center and the electron transfer flow between reaction center cofactors.

2.1 Cofactors

The bacterial reaction center includes a variety of cofactors. The basic composition of the cofactors is very similar between species, but some of the cofactors might differ in their substitution groups. Take the purple, non-sulfur *Rb. sphaeroides* reaction center 2.4.1 strain (the wild type) for example, it has 10 cofactors in its structure in total: four bacteriochlorophyll-*a* (Bchl-*a*s), two bacteriopheophytin-*a* (Bphe-*a*s), two ubiquinones (ubiquinone-10), one non-heme iron (Fe^{2+}), and a carotenoid (spheroidene). Crystallography work shows that other external, small molecules can bind to the reaction center protein and thus appear in the crystal structure. The most common binding molecule is a detergent molecule, the Laudryl Dimethylamine-N-Oxide (LDAO), used to mimic the lipid environment in protecting the isolated reaction center protein. Some other ligands

that occasionally appear in the crystal structures are cardiolipin (CDL), glycerol, and phosphate ions (PO_4) .

There are several methods of classification for the 10 reaction center cofactors. In this thesis, the cofactors are classified according to their spatial location in the cell membrane, from the periplasmic side to the cytoplasmic side (Figure 2). This method offers a most straightforward classification of cofactors and it also roughly fit in electron transfer events occur on different cofactors in a chronicle order. As discussed in the next section, one special characteristic of the reaction center protein is its pseudo-C2 symmetry. The insertion of the reaction center protein in membranes is nearly "upright" , that is, the two-fold symmetry axis is parallel to the normal axis of the membrane(within 5^{o})[11]. This two-fold symmetry axis can be approximately drawn out by connecting the symmetric Bchl-*a* dimer with the non-heme iron (Fe^{2+}).

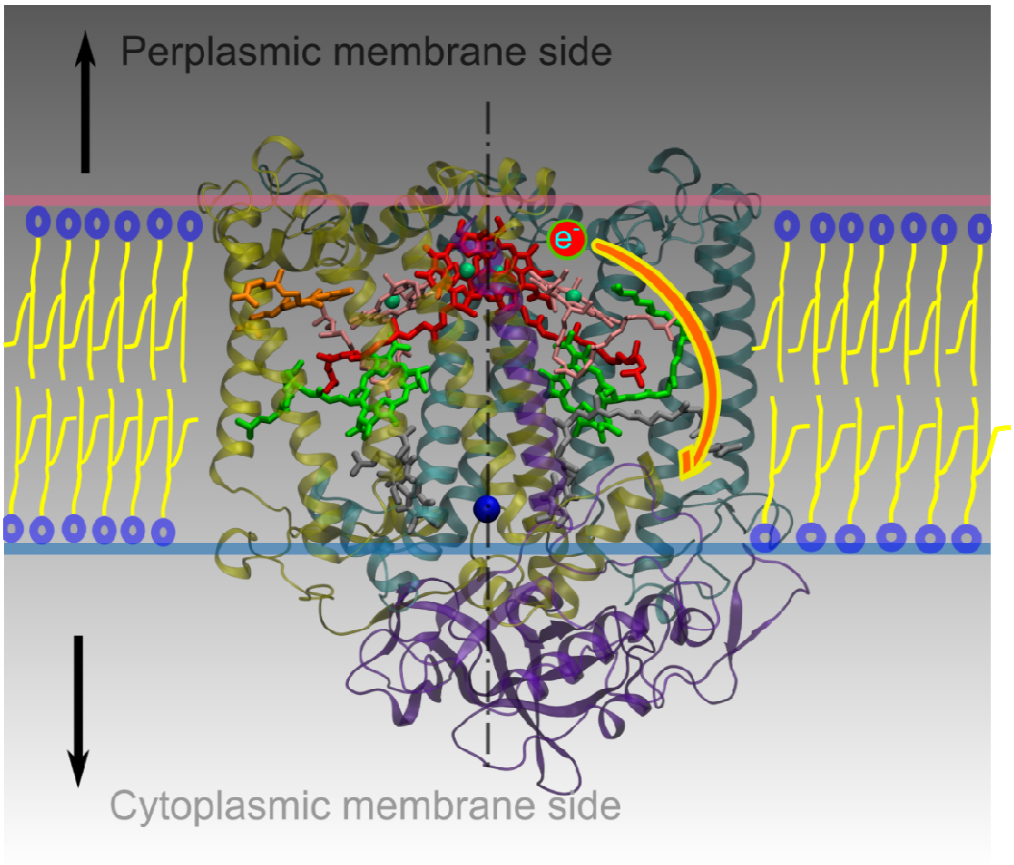

Figure 2: The reaction center structure in cartoon representation. The upward arrow indicates the periplasmic membrane side; the downward arrow represents the cytoplasmic membrane side. This figure is showing the *Rb. sphaeroides* reaction center structure, including 3 subunits: L, M and H. The L subunits (gold) and the M subunits (navy blue) are contained within the lipid bilayer membrane; H subunit is on the cytoplasmic membarne side (purple). The reaction center exhibits C2 symmetry, represented by the black dash line. The cofactors appear in stick representation. The charge separation begins at the Bchl-*a* dimer and proceeds towards the cytoplasmic membrane side (indicated by orange and yellow arrow).

The cofactors that are closest to the periplasmic side are two symmetric Bchl-*a* molecules in a pair, known as the special dimer **P** (Figure 3).

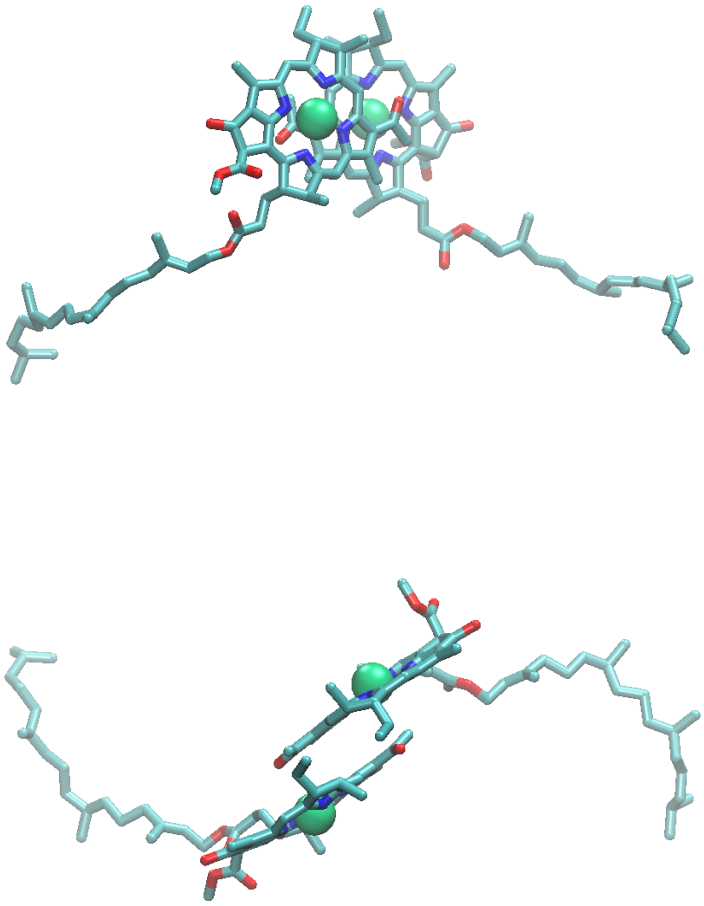

Figure 3: The special dimer **P** structure in the wild type *Rb. sphaeroides* reaction center (PDB id: 2J8C). The top image shows the Bchl-*a* molecules from a front view and the bottom image represents a top view (from the periplasmic membrane side).

The porphyrin planes from two Bchl-*a* molecules are parallel (the angle between porphyrin rings normal axes is about 8^{o}), separated by 3.5 Å. The two Bchl-*a* molecules that from two branches and have different functions in electron transfer are labelled as A and B. In native reaction centers, the electron transfer occurs

through the A branch with a > 97% yield from spectroscopic measurements[12-15], a fact that is quite surprising because it is contrary to quasi-symmetric structure observations. The stacked porphyrin planes likely form into a strong $\pi - \pi$ interaction, which is often seen in charge transfer systems with high polarizability[16-18]. Indeed, this is the starting point of charge separation in isolated reaction centers. The special dimer has the longest absorption wavelength (865 nm for *Rb. sphaeroides*, 960 nm for *Rps. viridis*) among all of the photoactive cofactors and is the most easily excited. Theoretical calculations performed by Warshel et al. show that the degenerated orbitals from two Bchl-*a* molecules cause the energy levels to split, and move one of them to the low energy side[19, 20]. As a result, the excited state P* has a strong charge transfer state capability; the charge density of P^*/P^+ is delocalized on two Bchl-*a* molecules. These observations were confirmed by Electron Paramagnetic Resonance experiments, where the P^+ lineshape is 1.4 times narrower than that of the Bchl-*a* cation radical[21].

Moving along the normal membrane axis to the cytoplasmic side, two Bchl-*a* monomers flank the special dimer along both branches. These accessory bacteriochlorophylls, or bacteriochlorophyll monomers, are represented by the symbols B_A and B_B. The absorption wavelength for the lowest excited state of B_A and B_B are both close to 800 nm (790 nm for B_A and 810 nm for B_B). The bacteriochlorophyll monomers situated between the special dimer and the bacteriopheophytin and the location make it a bridge for the charge transfer

between the special dimer and the bacteriopheophytin. The bacteriochlorophyll monomers are mirror images of each other along the C2-axis (both are 10-11 Å in distance and 60-70 degree in porphyrin orientation angle, on both sides in *Rb. sphaeroides* reaction center). Many debates in the past 20 years focused on the role of B_A in primary electron transfer (electron transferred from the special dimer P to bacteriopheophytin H_A), about whether it is a real physical intermediate electron carrier or just functions in a superexchange manner[22-25]. Early experiment facts that support the latter conclusion are largely limited by low time resolution as well as poor signal-to-noise ratio of early spectroscopy techniques. Opinions have started to converge since Zinth and his coworkers showed that, at least in the wild type reaction center, a B_A^- absorption band near the 1020 nm infrared wavelength region could be identified and decays with a very short life time (0.9 ps), which strongly supports an intermediate electron acceptor viewpoint[23, 25]. It is natural to imagine that maybe the reverse reaction also relies on B_A to return the electron back to P, and some preliminary evidence suggests that this could be true[26, 27]. This possibility is further explored in Chapter 3. The function of bacteriochlorophyll on the other branch (B_B) is much less known as discussed in the following section on the electron transfer pathway. It is speculated that it possibly performs the role of triplet sate energy transfer intermediate between P and the carotenoid[28].

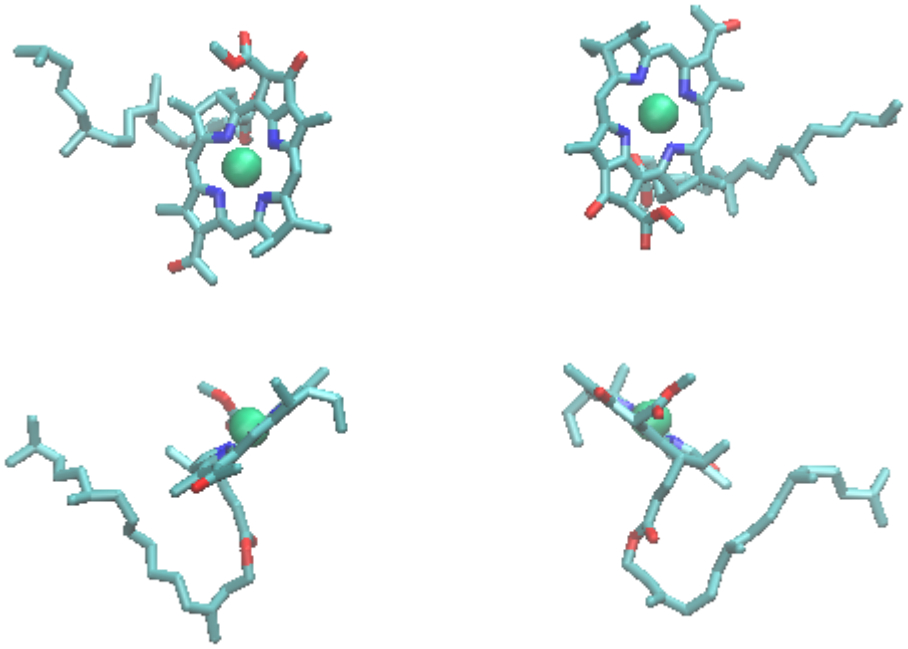

Figure 4: Structure of the bacteriochlorophyll monomers B_A (right) and B_B (left) in the *Rb. sphaeroides* wild type reaction center (PDB id: 2J8C). The top images represent the view from the front; and the bottom images represent a top view (from the periplasmic membrane side).

The bacteriopheophytin H_A , by moving even more to the cytoplasmic side in the reaction center, is the next electron acceptor following B_A in primary electron transfer (equivalent on the M branch is H_B). The lowest excitation energy level of the bacteriopheophytin is higher than that of bacteriochlorophyll, reaching 740-760 nm in the reaction center protein. Following the primary electron transfer, H_A donates the electron to Q_A in the following step in ~200 ps (wild type)[13]. The quinone is considered as the final electron acceptor in the reaction center protein. According to symmetry, there are also two quinones in two branches, and the distance between Q_A and Q_B is about 18.5 Å. Because of the asymmetry of the

electron transfer pathway in the reaction center, the quinone on the A branch (Q_A) receives the electron from the bacteriopheophytin (H_A) in the first place, and then passes it on to the B branch quinone (Q_B) in 100 μs at a pH of 7.5[29, 30]. Most early reaction center research focused on the redox chemistry of quinone[31-37], finding that one quinone can accept up to two electrons. It was also found that the protonation state of quinone affects its redox potential[38-40].

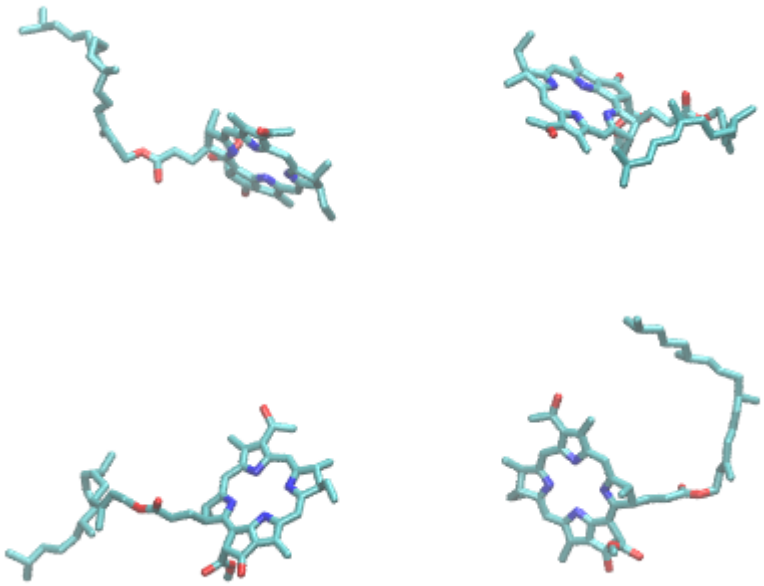

Figure 5: Structure of the bacteriopheophytins H_A (right) and H_B (left) in the *Rb. sphaeroides* wild type reaction center (PDB id: 2J8C). The top images represent the view from the front; and the bottom images represent a top view (from the periplasmic membrane side).

The non-heme iron locates between, on the cytoplasmic side of the membrane, is located between Q_A and Q_B. It is closer to Q_B, at 8.0 Å, and further away from Q_A, at 11.0 Å. Mossbauer spectroscopy[41], extended x-ray fine structure absorption[42,

[43], and EPR experiments[44, 45] indicate that it is a high spin Fe^{2+}. Surprisingly, even though the nonheme iron atom is geometrically in the middle of two quinones, it does not appear to play an important role in the electron transfer between them. Upon Fe^{2+} removal, $Q_A \rightarrow Q_B$ electron transfer is barely harmed [31]. Other divalent metal ions (e.g. Zn, Ni, Co, Mn, Cu) have been used to replace Fe^{2+} to test their affect on $Q_A \rightarrow Q_B$ electron transfer, but none appear to have a distinguishable effect[31]. This suggests that the formal charge on the metal ion rather than the detailed electronic structure of the ion is important for the reaction center function.

The last reaction center cofactor to discuss is the carotenoid. Carotenoids are important in photosynthesis because they are more than light capturing pigments; they are the main cofactors that function to quench the triplet state and perform photoprotection[46]. There are many types of carotenoids in nature, with differing lengths and terminal groups. The common structural feature of all carotenoids is a conjugate bonding system with an alternative single-double bond order. In reaction center protein, it takes the *cis* form in its center, and is inserted between B and C helices of the M branch, near B_B. The *cis* conformation facilitates the carotenoid to form its triplet state[47]. In wild type *Rb. sphaeroides* reaction center, the carotenoid is spheroidene, which has its main absorption at 440-520 nm in the visible region. In a so-called R-26 mutant strain, the carotenoid is absent in the reaction center and replaced by a lipid molecule in its binding site (or a LDAO molecule if the reaction center is isolated)[48].

2.2 Protein subunits

In the purple bacterium *Rb. sphaeroides* (will be discussed throughout this chapter, otherwise particularly mentioned), there are three protein subunits within the reaction center protein complex. These include two symmetric transmembrane subunits, L and M, and one subunit that does not belong to the transmembrane region, H. The L and M subunits have five membrane-spanning helices each. On the periplasmic side, the L and M subunits have three helical segments that connect a series of helices A and B, C and D, and the multi-part helix following helix E-- labeled ab, cd and e respectively (see figure 6).

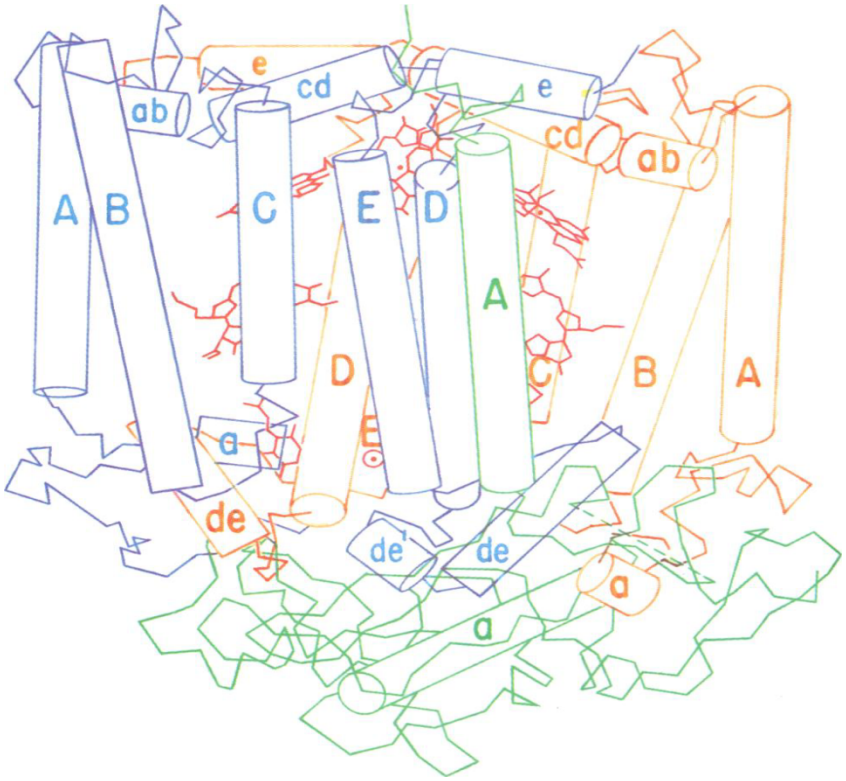

Figure 6: Labeling of each helical segment in the reaction center protein. The L subunit is shown in orange color, the M subunit in blue, and the H subunit is shown in green. The figure is reproduced from Allen et al.[9]

On the cytoplasmic side, there is one helix in the L subunit and two helices in the M subunit. The H subunit has only one transmembrane helix; its other structural regions behave more like a globular protein, composed of β-sheets, short α-helices and numerous random coils. The LM complex is capable of performing the charge separation between the special dimer (P) and the primary quinone Q_A without the presence of the H subunit. Removing the H subunit only changes the property of the quinones, for example, slowing down the $Q_A \rightarrow Q_B$ electron transfer by a factor of 10^2~10^3 [49]. The impaired $Q_A \rightarrow Q_B$ electron transfer can possibly be explained with a lower binding affinity of Q_B in the loosened structure after quinone removal. The extensive contacts of the H subunit with the LM complex probably stabilize the reaction center structure.

Generally, the hydrophilic and hydrophobic amino acid distribution in the reaction center is closely associated with its function as a membrane protein. There are no charged residues in the middle of the protein. All the charged amino acids are on the periplasmic or the cytoplasmic side of the membrane. In *Rb. sphaeroides* cells, the special dimer P is reduced by a water-soluble cytochrome *c*2. The reaction center has one cytochrome *c*2 binding site on the periplasmic side of the membrane, shared by both the L and M subunits. The binding domain on the reaction center contains negatively charged carboxylate groups that are believed to interact electrostatically, with lysine residues surrounding the heme crevice of the cytochrome *c*2.

2.3 Protein-cofactor interactions

The reaction center protein-cofactor interactions impact nearly every aspect of the cofactor photochemistry and redox chemistry. An apparent example is the ground-to-excited state transition in the ground state absorption spectrum, the coordination of histidine amino acids moves the absorption spectrum of the Bchl-*a* and Bphe-*a* molecules to the red by 30-50 nm. Regarding the structure of the special dimer P, near the central magnesium atoms are histidines M202 (assigned to P_M) and L173 (assigned to P_L). Crystal structure reveals that the His L173 is too far (4.0 Å) to coordinate directly with the magnesium atom of P_L) and but possibly forms a hydrogen bond with His L168. In *Rps. viridis*, hydrogen bonds are formed between the acetyl groups of the special dimer and His L168 and Tyr M195. It is worth noting that His L168 is well conserved in the reaction center between a multitude of species. The Tyr M195 in *Rps. viridis* corresponds to Phe M197 in *Rb. sphaeroides*, which loses the hydrogen bonding capability. It is reported that, in *Rb. sphaeroides*, the only hydrogen bond involving the dimer and the reaction center protein subunit is between the ring IV carbonyl of the propionic acid group of P_L and His L168. Most charged amino acids are at least 10 Å away from the porphyrin rings of the dimer, with the exception of Arg L135, which is 8.0 Å away. The bacteriochlorophyll momomers (B_A, B_B) in the *Rb. sphaeroides* also coordinates to the His imidazole rings. Previous research shows that the magnesium atom ligation is asymmetric for the two branches. His M182 coordinates with the magnesium atom of B_B, but His L153 is more distant

for its coordination to B_A. The hydrogen bond between Ser L178 and the carbonyl group of ring IV of B_B is the only one between the protein subunits and the bacteriochlorophyll monomers. The Bphe-*a* molecules do not have the magnesium centers, and therefore no coordination with the amino acids exists. One ionizable amino acid that is very close to one of the bacteriopheophytins, H_A, is Glu L104. Glu L104 is more likely protonated, and forms one hydrogen bond with the keto carbonyl of ring V of H_A[50]. This residue is conserved in purple bacteria, but is replaced by other amino acids in some green bacteria, like in *Cf. aurantiacus*. The presence of this residue causes

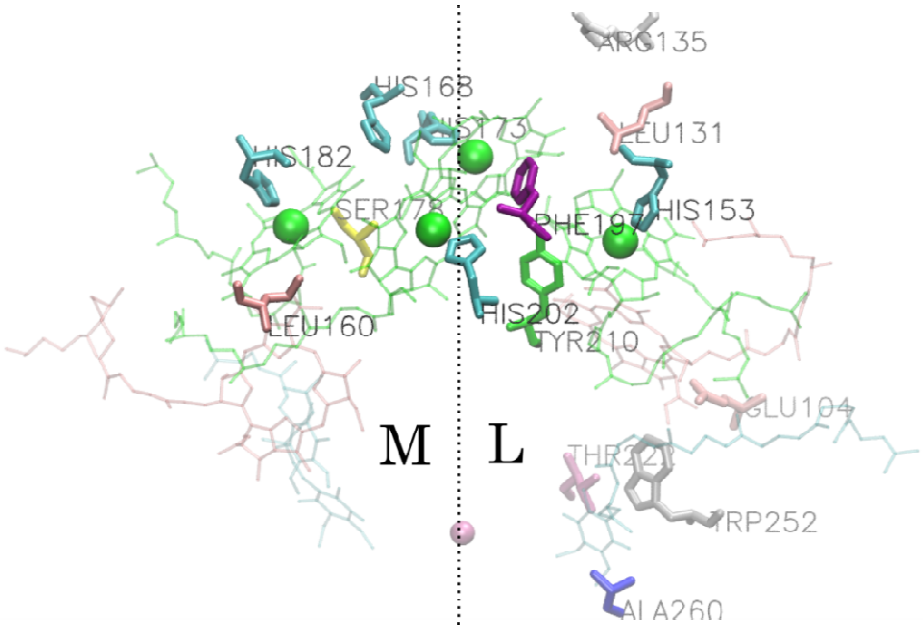

Figure 7: A structural model for major chromophores and the adjacent residues in the *Rb. sphaeroides* reaction center. Four Bchls (green), two Bphes (pink), and two quinones (cyan) are shown in a transparent line model, while the iron cofactor is represented by a sphere in purple. The C2 symmetry axis is indicated as a vertical dashed line. L branch is on its right hand side, and M is on the other side. The amino acids that have important protein-cofactor interactions with the chromophores (mentioned in the text) are highlightened and labelled.

the ground state absorption spectrum of the reaction center to split between two branches, at 532 nm on B branch and 545 nm on A branch (the difference is more apparent at low temperatures). The carotenoid, sphaeroidene, is mostly surrounded by residues with aromatic side chains, which applies strong steric constraints upon the carotenoid conformation. No charged residues were found within 10 Å from the spheroidene. Two carbonyl oxygens of Q_A are within hydrogen bonding distance from the peptide nitrogen of Ala M260 and the side chain of Thr M222, respectively. Several aromatic residues that are near Q_A are conserved between species (e.g. Phe M251 and Thr M252). Thr M252 bridges H_A and Q_A; no ionizable residues other than the histidines ligated to Fe^{2+} are located within 8 Å of the quinone ring. The one-electron semiquinone species Q_A^- and Q_B^- are protonated by interacting with amino acid residues that have pKa values perturbed by electrostatic interactions, thus resulting in the observed proton uptake. When Q_B is doubly reduced, Q_B^{2-} accepts two protons and Q_B H_2 is replaced by an unprotonated, neutral exogenous quinone. $Q_A \rightarrow Q_B$ electron transfer in bacterial reaction centers can be blocked by herbicides such as 1,10-phenanthroline. The blocking mechanism is believed to be a competition with quinone for the binding site.

2.4 Electron transfer pathway in the reaction center

In vivo, the reaction center accepts the energy transferred from the surrounding antenna and utilizes it to perform charge separation. The energy

acceptor is the special dimer P. *In vitro*, to simulate such an initial event, the dimer P of the isolated reaction center is directly excited using actinic light. The ideal excitation wavelength is usually around 860 nm (the absorption peak of P) or slightly move to the red. This largely thanks to the progress of laser technology during the past two decades. Previously, limitations of the excitation wavelength selection (for example, only 600 nm or 537 nm available) would cause undesirable side effects like simultaneously exciting multiple light absorbing cofactors. Figure 14 provides a ground state absorption spectrum from wild type *Rb. sphaeroides* reaction center strain 2.4.1. The main spectral contribution from each cofactor has been assigned in the visible and IR regions. Experiment and theoretical calculations, however, show that the 780-820 nm spectral region could have the contributions from more than one cofactor, which makes it a very complex spectral range to analyze. When P is excited by 860 nm light, the sequential forward electron transfer events occur in the following order (for an energetic/kinetic scheme, see Figure 8):

$$P^* \rightarrow (B_A) \rightarrow H_A \rightarrow Q_A \rightarrow Q_B \qquad (1)$$

This electron transfer flow is true for wild type, and a successful design of sequential electron transfer should act accordingly. A bad design, such as artificially introducing certain mutations somewhere inside the reaction center, could possibly decrease the net yield of the final charge separation product as a result of compromising to other pathways, including fluorescence or an increase in the reversed recombination process to the ground state (see also Figure 8).

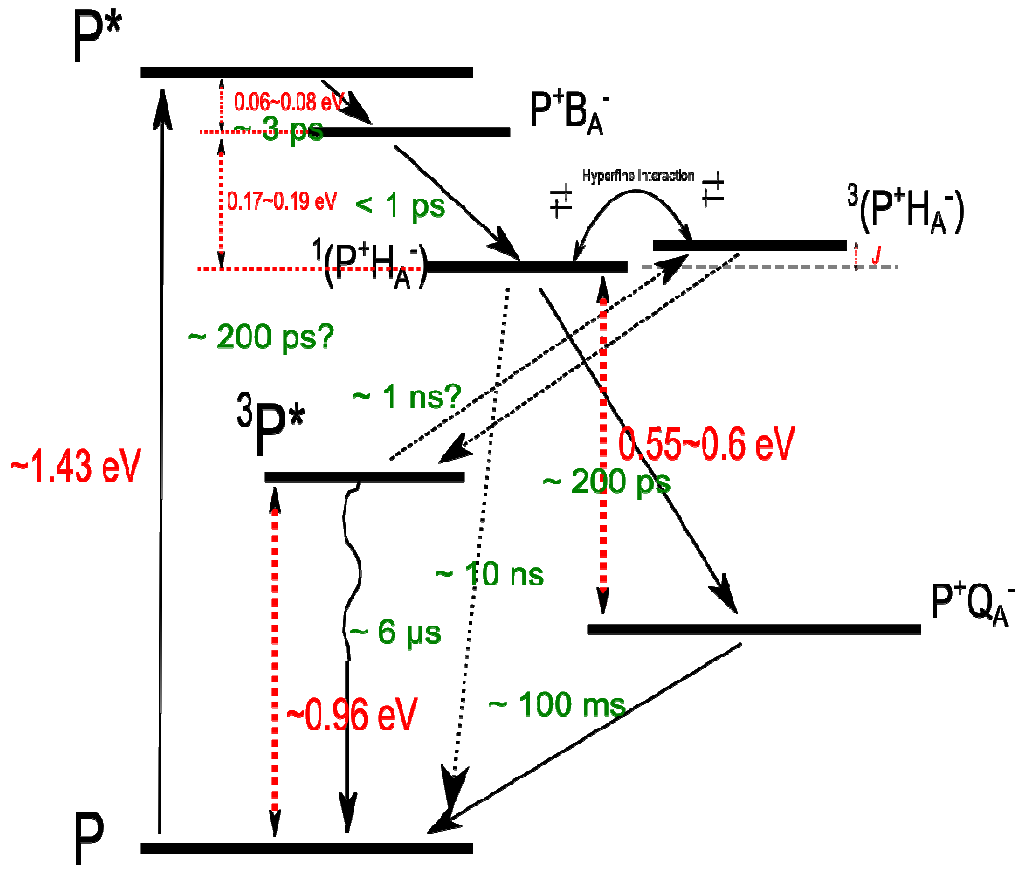

Figure 8: The energy level scheme for the electron transfer pathway that generally occurs in the wild type *Rb. sphaeroides* reaction center after light excitation occurs in the special dimer (P). ${}^3\left(P^+H_A^-\right)$ and ${}^3P^*$ represent the triplet charge separated state, $P^+H_A^-$, and its charge recombined product, triplet excited state of P, respectively. The solid arrows show the forward electron transfer process, and the broken arrows show branched electron processes that have been observed (black) and reversed charge recombination steps that could potentially occur (grey). Red numbers indicate the estimated free energy gap between two energy levels, and green numbers represent the life time constants that have been determined for some of those processes.

$$\begin{array}{ccccccccc} P^* & \leftrightarrow & (B_A) & \leftrightarrow & H_A & \leftrightarrow & Q_A & \leftrightarrow & Q_B \\ \Downarrow & & \downarrow & & & & & & \\ \Rightarrow & & P & & & & & & \end{array}$$

Another feature of the electron transfer in the reaction center is its unidirectionality—its exclusive transferrence through the A branch—which is

perplexing in terms of the symmetry cofactor arrangement of the two branches. In the past twenty years, people have been trying to understand why the electron transfer only occurs through the L(A) branch and many attempts have been made to experimentally alter the M(B) branch to try to initiate electron transfer through it. However, it appears that the unidirectionality is robust in an evolutionary sense, as mutating one or two residues does not perturb the branching ratio significantly[50, 51]. One single point mutant M182HL does increase the A:B electron transfer branch ratio from 30:1 to 2:1, yet the B side electron is stuck in B_B until it returns to P and there is no indication showing that the electron further transfers to H_B[52]. Other mutants attempted to re-activate the M(B) branch with a combination of multiple mutation sites; they implement a relatively high B branch yield by impairing the L(A) branch electron transfer [51, 53, 54]. It is possible that the M(B) branch has other important roles in photosynthesis yet unrecognized. This thesis will provide speculations in the conclusion part based on some of the observations in Chapter 4 about what those other roles could entail.

3 Site-directed mutagenesis in the reaction center protein

In order to create mutants that fulfilled the purpose for the experiments, a strain of *Rb. sphareoides* bacteria was re-engineered in various aspects. Particularly, for the mutations that were introduced into the L and M branches, the genes for both branches were removed from the wild type strain, the leftover genes were termed $\Delta LM1.1$. The genes for the L and M branches are located on a plasmid, pRKSCH-7H, which is was inserted into the $\Delta LM1.1$ strain, after being

altered to contain the desired mutation, to create the mutants. The pRK plasmid is roughly 14kb long, and has a low replication capability in living cells which makes it difficult to use for mutagenesis. Thus, a smaller plasmid, pUC, was used for the early stages of the mutagenesis. To perform a rapid isolation of reaction centers with high purity and yield, the poly-histidine tag strain, which is has a poly-histidine tag added to the C-terminal of reaction center M-subunit was utilized. The His-tags facilitate recovery of pure reaction centers in less than four hours with a commercially available Ni^{2+} resin. Traditional mutagenesis techniques were used in this experiment to generate mutant reaction centers. The theories behind some of the techniques are discussed below and include PCR, restriction digestion, electrophoresis, ligation, transformation, DNA sequencing, conjugation, and column chromatography. The overall work flow of performing a mutagenesis is indicated in Figure 9. Polymerase chain reaction (PCR) is a process by which DNA can be replicated or a point mutation can be introduced into a plasmid, a circular piece of DNA found in bacteria. A primer is a single-stranded piece of DNA which binds, or anneals, to the plasmid that will contain the desired mutation. The primers contain the DNA sequence for the desired mutation, and then a sequence complementary to the plasmid extends ~10 bp on either side of the mutation in order to facilitate annealing. Both a forward and a reverse primer are designed, one being complementary to each of the two strands of the plasmid. The primers must also be kept from forming many secondary structures at the annealing temperature, because it would prevent binding to the

plasmid. In the initial step of PCR, the parental strands of DNA are denatured, or separated, by exposure to a high temperature of $95^{o}C$.

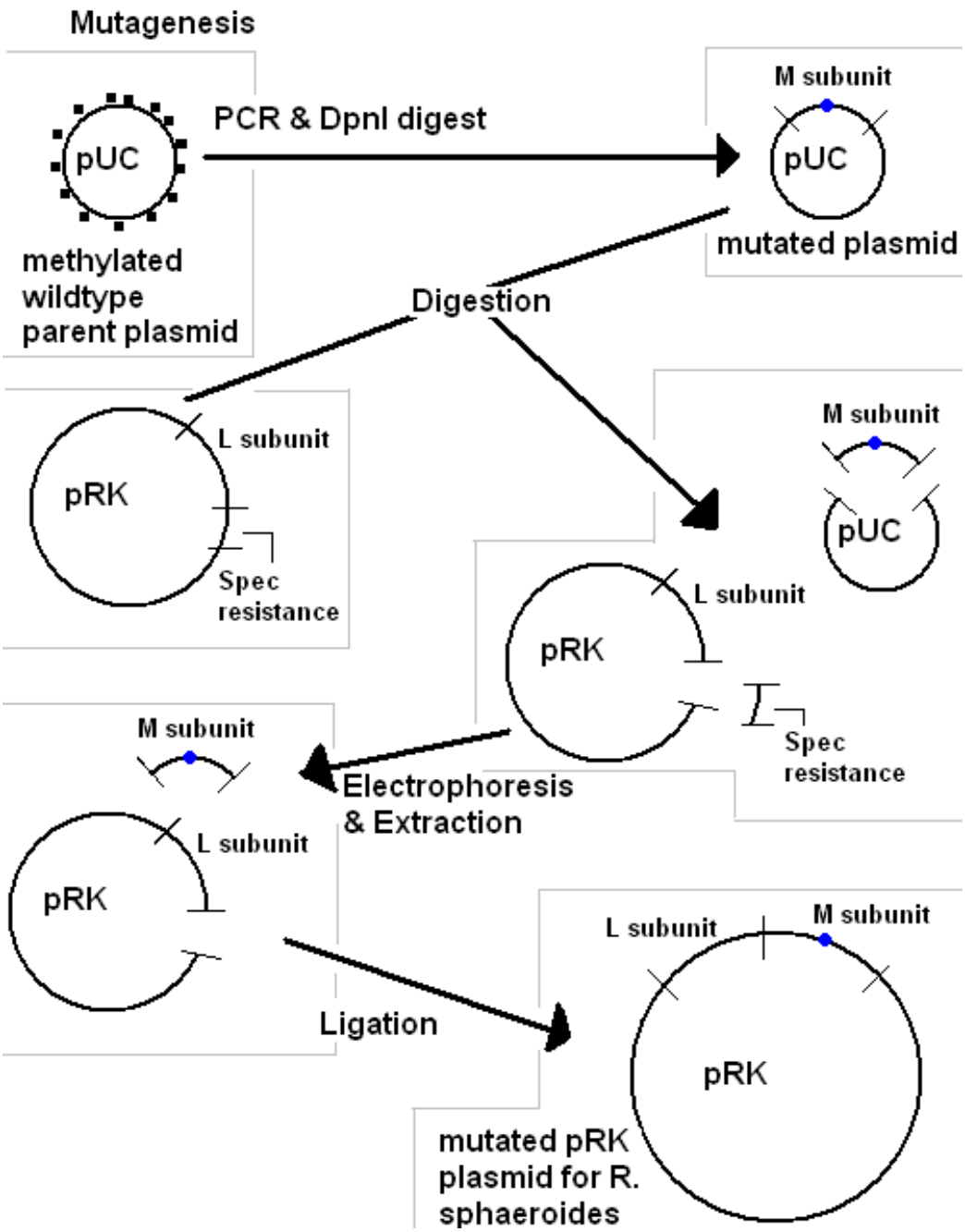

Figure 9: A flowchart for performing reaction center mutagenesis. The chart stops at a verified mutation sequence of pRK plasmid, the subsequent conjugation step is not shown.

This results in two complementary single-stranded pieces of the parent strand. The annealing phase follows at a temperature of $68^{o}C$, binding the primers to the complementary sequence on the DNA plasmid. In order to avoid nonspecific binding of the primer to an incorrect location on the plasmid, the annealing temperature should be $4 - 10^{o}C$ lower than the melting temperature of the primers, which can vary depending on the number of C-G and A-T base pairs in the primer. A thermostable DNA polymerase is used to add base pairs to the primers using free deoxynucleotide triphosphates (dNTPs) to form duplex DNA. For this elongation to occur, the temperature is raised to $72^{o}C$. When the extension period has completed, the DNA is heated to become single-stranded DNA again and the process is repeated, thus exponentially increasing the amount of DNA over many cycles. Because bacteria methylate plasmids that they reproduce, the parent strand plasmid which is used in PCR is methylated. PCR itself, however, does not generate methylated DNA; therefore, resulting PCR product contains the desired mutated plasmid without methylation and some double-stranded DNA where one of its two strands has the methylated unmutated plasmid DNA. In order to maintain only the mutated plasmid, a restriction endonuclease called DpnI is added. This enzyme cuts methylated DNA and causes it to be unable to function. Adding DpnI to a PCR product creates a solution of mutated plasmids. Another use for restriction endonucleases is to cut DNA at specific sequences, typically four or six base pairs in length. Some types of these enzymes form "sticky ends" of DNA, which contain several unpaired

bases, allowing for easy reattachment to an end cut by the same enzyme. This process allows pieces of one plasmid to be excised out and introduced into another plasmid that was cut by the same enzyme. The pUC AH plasmid has restriction endonuclease sites around the genes of the L subunit which are cut by the enzymes HindiIII and Asp718. The pUC HB plasmid has sites around the genes of the M subunit that can be cut by BamHI and HindiIII. The pRK plasmid also has similar restriction sites surrounding each subunit. As a result, a set of subunit genes can be cut from the pUC plasmid and inserted into the pRK plasmid (Figure 10).

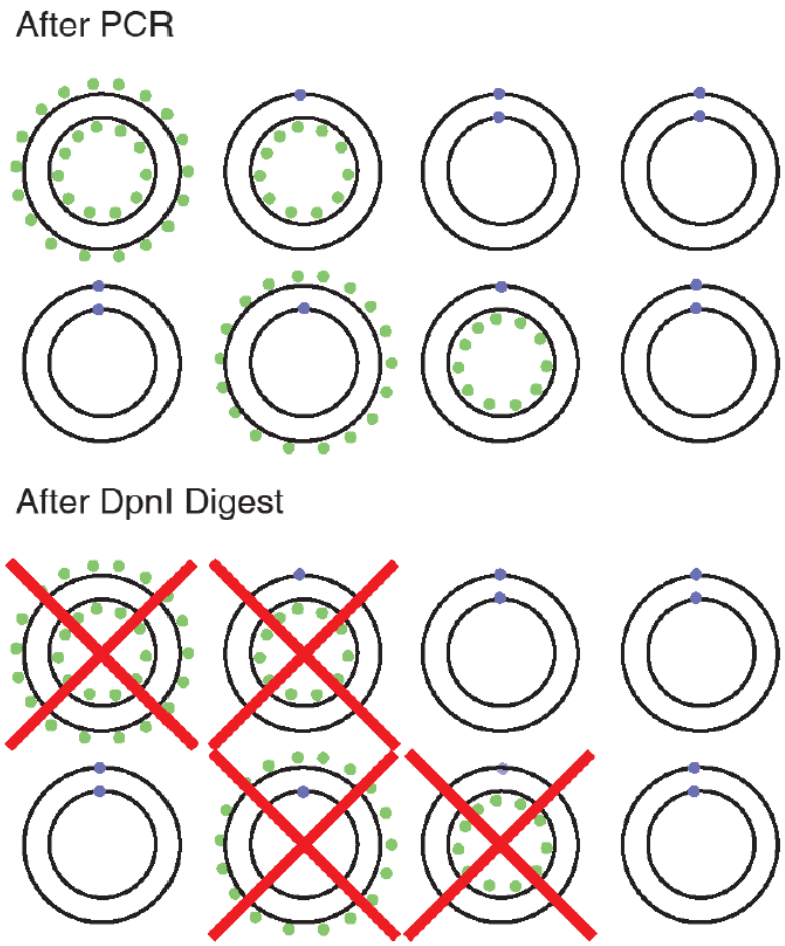

Figure 10: Sketch representing the Dpn-I digestion process of the PCR product. Two parental strands of plasmid DNA are shown as two concentric circles. The primers are shown as blue dots on the plasmids. The green dots represent the methylated sites, and the corresponding plasmids are the wild type templates. The Dpn-I restriction enzyme cuts and digests the methylated plasmids, leaving only the re-amplified, mutated plasmids.

Gel Electrophoresis

Before combining the genes, the desired subunit (insert) and the fraction of the pRK plasmid desired (vector) should be separated out. If left too long, the restriction enzymes cut the plasmid at nonspecific sites. To separate, gel electrophoresis is performed. Gel electrophores, is a method that is used for large DNA molecules such as the plasmids in this experiment. When an electric current is applied to DNA placed within agarose gel, the negatively charged DNA migrates to the positive anode through the agarose. The speed at which the DNA migrates is inversely related to its molecular weight. By staining the gel with ethidium bromide, an intercalating agent that is fluorescent under UV light, the DNA can be visualized. The distance the DNA travels indicates the location of the desired fragments, which can then be cut and extracted from the gel.

Ligation

Following gel extraction, the DNA fragments with complementary sticky ends (fragments cut by the same restriction endonuclease) can be spliced together with ligase. T4 DNA ligase is an enzyme which is used to seal nicks in DNA after the complementary overlapping ends have annealed by catalyzing the repair of the sugar-phosphate backbone. An ideal 3:1 ratio of inserted DNA to vector plasmid

must be achieved prior to starting a ligation to ensure that few unwanted ligation products form. Once ligated, the plasmid is ready to be inserted into bacteria.

Transformation

In order to replicate a plasmid, to select for a particular plasmid, or to use bacteria to make plasmid gene products, a vector plasmid must be transformed into the bacteria. Two methods of transformation can be used--depending on the bacteria--either heat shock or electroporation. In order for bacteria to take up DNA through heat shock, cells must be competent, or able to take up foreign DNA. In this process, the bacterial cells are rapidly heated, allowing DNA from the surroundings to enter the cells. Electroporation works by briefly shocking the cells with an electric current to open pores in the membrane, thus facillitating negatively charged DNA to move into the cells. Electroporation typically has a higher transformation efficiency, but requires a low medium salt condition.

Antibiotics

In order to select for the presence of the desired plasmid, the bacterial cells are plated with antibiotics. The pUC plasmid contains an antibiotic resistance gene for ampicillin, and the pRK plasmid contains an antibiotic resistance gene for tetracycline.

Sequencing

In order to verify that the desired mutation is present on the plasmid, DNA sequencing must be performed. In this experiment, the sequencing is performed in the ASU facility. The sequence result was compared with the wild type plasmid using the BLAST engine at the NCBI site (http://www.ncbi.hlm.nih.gov/blast),

thus ensuring that the target site was mutated and that there were no other unwanted mutations.

Conjugation

Once the desired sequence is verified to be present on the pRK plasmid, the plasmid is transformed into a special type of E. coli called S17. S17 has the genetic capability of mating with other bacteria. Since the conjugation process results in horizontal gene transfer, S17 is henceforth used to insert the mutated pRK plasmid into *Rhodobacter sphaeroides*.

Isolation

The *Rb. sphaeroides* carrying the mutation are then grown in the dark anaerobically for about 72 hours. The cells are then broken, and reaction centers are isolated via column chromatography. The reaction centers have been mutated to contain a His-tag, or a chain of 6-7 histidine residues, used to aid in protein isolation by a Nickel-binding column. Nickel-binding columns use affinity chromatography in which a portion of the desired protein--in this case the His-tag--has a strong binding affinity for a substance that is attached to the column in the stationary phase. When the unpurified protein is added to the column, it binds closely to the collumn and all of the undesired impurities (mostly antenna proteins) can be washed away. The purified protein is then eluted with a compound that has a higher binding affinity for the column than does the protein; the compound used was deprotonated imidazole. The elution is then dialyzed in a dialysis membrane overnight to remove excessive salts, detergents, and imidazole molecules from the product—the isolated reaction centers.

4 Basics about laser spectroscopy

According to Google dictionary, the definition for spectroscopy is “the branch of science concerned with the investigation and measurement of spectra produced when matter interacts with or emits electromagnetic radiation”. Two basic aspects of the light-matter interaction, absorption and emission, constitute the fundamental means of spectroscopy investigation. The electronic absorption is a special type of absorption, where the ``matter" in the ``light-matter" interaction, in a classical viewpoint, is specifically restricted to the transition dipole (μ_{ba}) between a lower energy state (most commonly the ground state) (a) and a higher energy state (e.g., first excited state) (b) of a molecule under investigation. In other words, the electronic absorption is a mapping of a molecule's electronic structure. The quantity $E \bullet \mu_{ba}$ (where E is the field strength applied by the electromagnetic radiation) becomes an important term within the transition probability density T_{ba}, according to Fermi's golden rule:

$$T_{ba}(\tau) = \frac{(E_0 \cdot \langle \psi_b | \mu | \psi_a \rangle)^2 \rho_v(\nu_0)\tau}{\hbar^2}$$

$$= (E_0 \cdot \mu_{ba})^2 \rho_v(\nu_0)\tau/\hbar^2$$

Where, $\rho_v(\nu_0)$ is the phonon density between v and $v + dv$,

and $\nu_0 = (E_b - E_a)/h$

Because the electronic structure of a molecule is intimately associated with its geometry, so too is the transition dipole. For molecules with regular symmetry, the orientation of the transition dipole is not very difficult to postulate based on the symmetry of the orbitals that are invovled. Conversely, the absorbing light frequency of the ground to excited state transition is also defined by the energy gaps that correspond to a combination of single-electron orbital transitions (configuration interactions). Take the Bchl-*a* molecule for example, the HOMO and LUMO are not enough to explain the energy state transitions that occur in this molecule. At least four orbitals are required to qualitatively describe the real transitions found in the spectrum. Different combinations of the orbital-to-orbital transition results in two fundamental low-lying excited state transitions Q_x and Q_y, and certain high energy excitation in the Soret band (Figure 11).

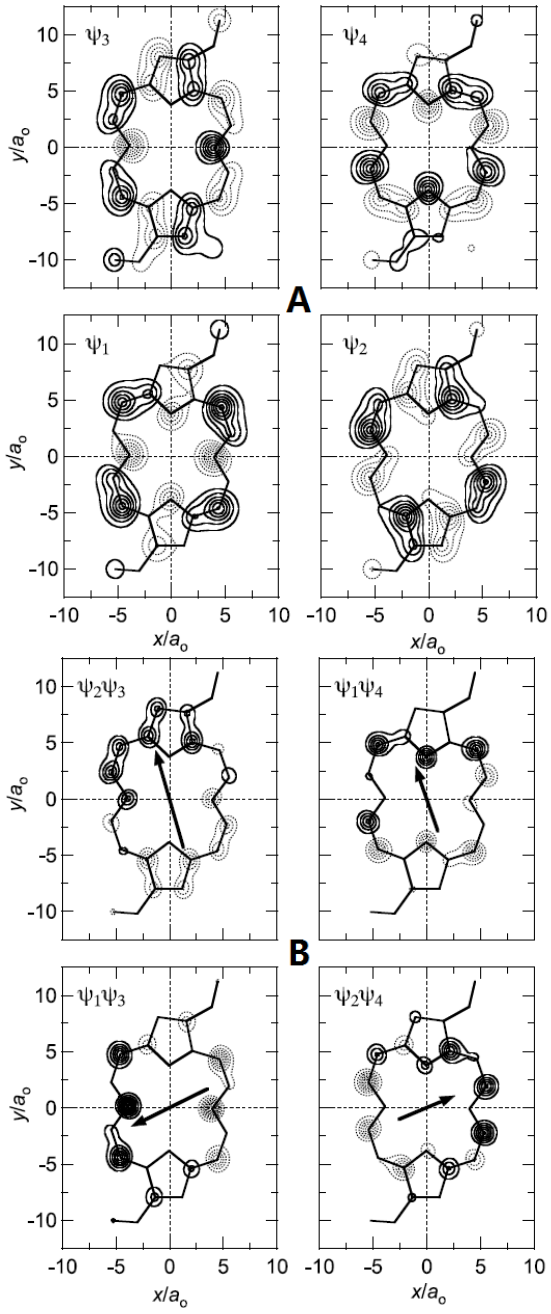

Figure 11: Schematic graph depicting (A) the molecular orbitals of HOMO+1(ψ_1), HOMO(ψ_2), LUMO(ψ_3), and LUMO-1(ψ_4) in BChl-*a*; and (B) the realistic molecular transitions found in BChl-*a* that are actually a combination of four different frontier orbitals (configuration interactions). Each transition dipole vector is indicated by a black arrow. Figure is adapted from WW Parson's book[55]

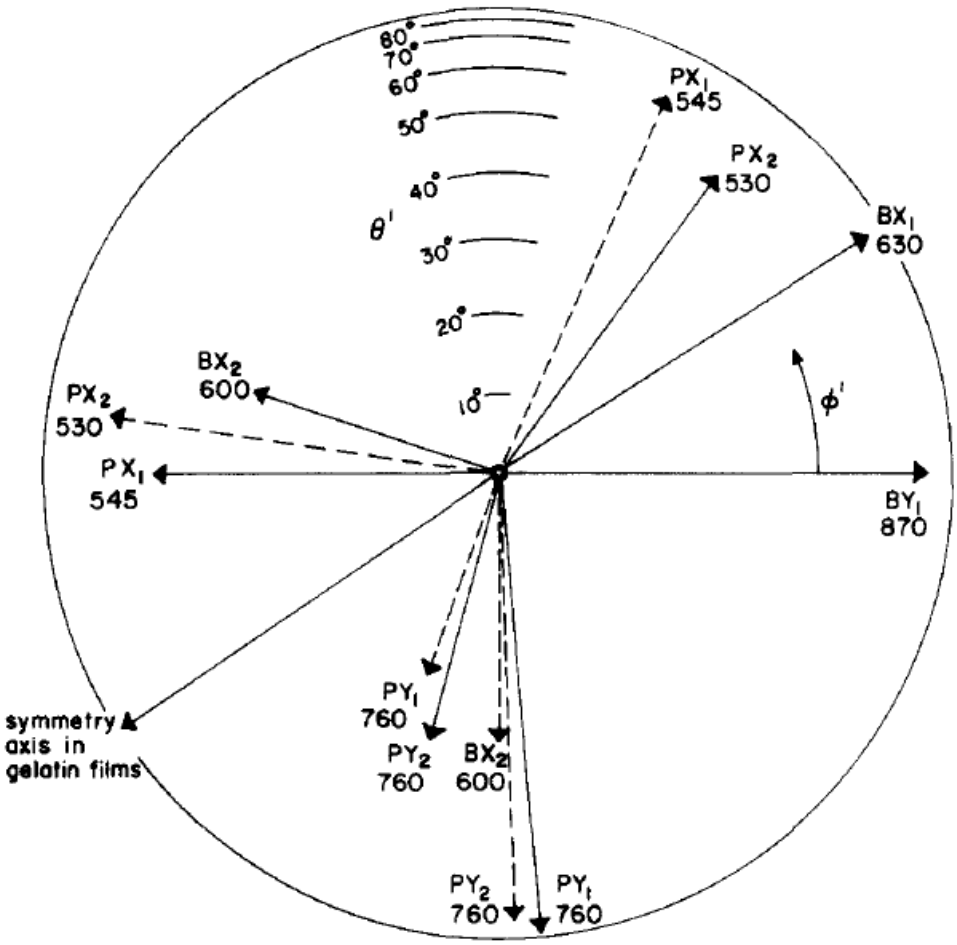

Figure 12: The orientation of different transition dipoles from all of the cofactors in *Rb. sphaeroides* reaction center. This image is ordered in a polar view, using a spherical cooridnation system where the pole is normalized with the chromophore membrane plane (C2 symmetry axis of the reaction center). Arrow lengths are scaled to the magnitude of the transition dipole moment(estimated from the absorption peak height), and the polar angles are estimated from LD/A spectra. Linear dichroism spectra was performed in air-dried gelatin film at cyrostat temperature (4 K). This figure is adapted from Rafferty et al.[56]

One special type of spectroscopy associated with absorption is dichroism, which means that the absorption coefficient changes as a function of light polarization angle. One of its origins is the change of $E \bullet \mu_{ba}$, because the following:

$$\vec{E} \cdot \overrightarrow{\mu_{ba}} = | \vec{E} \, || \, \overrightarrow{\mu_{ba}} | \cos\theta \qquad (2)$$

where θ is the angle between the molecular transition dipole (μ_{ba}) and the polarization axis of the light (orientation of **E**). Because the absorption strength depends on $\cos\theta$, if the molecules in a sample have a fixed orientation in a collective manner, the strength of the absorption can depend heavily on the angle between the orientation axis and the polarization axis of **E**. Absorbance dependence on the light polarization angle is called *linear dichroism*. Linear dichroism is not observed if the sample is isotropic. In bulk samples of random distributions of molecule orientation, integration over the azimuthal angle $\cos^2\theta$ is a constant(1/3). Anisotropic samples, such as those embedded in membranes, exhibit strong linear dichroism. In reaction center protein, once the reaction centers are immobilized in the dried gelatin film (or polyvinyl alcohol, PVA film) and are mainly oriented parallel to the membrane axis, the linear dichroism spectroscopy can provide a good estimate of the orientation of each chromophore (figure 12) [56]. When the excitation polarization in the linear dichroism experiment is selected to be parallel to the membrane axis, the cosine value of the angle between the Q_x (Q_y) transition and the membrane axis can be interpreted from the LD/A spectra (a normalization procedure, using the linear dichroism (LD) spectrum to divide the ground state absorption (A) spectrum). The geometrical orientation of each cofactor predicted from this method is very close to the crystal structure which was discovered later on, exhibiting the power of this spectroscopy[57, 58]. In addition to the response to the light electric field E, which causes linear dichroism, molecular dipoles also respond to the light magnetic field

B, which leads to the circular dichroism (CD). A corresponding physical phenomenon of this interaction is that optically active material can have different absorption for left- and right-circularly polarized light. A linearly-polarized incoming light can be decomposed into two, equal-amplitude, left- and right-circularly polarized light components. If the linearly-polarized light passed the sample, those two components shall experience different absorption in it, resulting in an elliptic outgoing light because of the less-absorbed left- or right-circularly polarized light component. The complex rotatory power detected by circularly-polarized light is given by:

$$(\varphi - i\,\varphi') = \frac{16\pi^3 N_A}{\lambda^2} \cdot \frac{n^2 + 2}{3} \cdot \beta \qquad (3)$$

where,

φ is the real part of the rotatory angle associated with sample absorption, i.e. the dichroism effect;

φ' is the imaginary part of the rotatory angle associated with sample refraction, i.e. the birefringence effect;

λ is the absorption wavelength;

n is optical refractive index;

and β is a parameter analogy to the polarizability α. Its specific form is given by the induced electric dipole $\vec{p}$ and the induced magnetic dipole $\vec{m}$:

$$\vec{p} = \alpha \cdot \vec{E} - (\frac{\beta}{c}) \cdot \frac{\partial \vec{H}}{\partial t}$$

$$\vec{m} = (\frac{\beta}{c}) \cdot \frac{\partial \vec{E}}{\partial t},$$

Where the β parameter is given by,

$$\beta_a = \frac{c}{3\pi h} \sum_b \frac{R_{ba}}{\nu_{ba}^2 - \nu^2 + 2\pi i \nu \gamma_{ba}} \qquad (4)$$

and R_{ba} is the rotatory strength in a very simple form:

$$R_{ba} = Im\{< a \mid \vec{p} \mid b > \cdot < a \mid \vec{m} \mid b >\} = \mid \vec{p} \mid \mid \vec{m} \mid \cos\theta \qquad (5)$$

For those measurements performed in the ground state, state *a* is ground state, and *b* runs over all excited states. Expression (5) reveals the most critical factor that influences the CD signal intensity, which is determined by the relative angle between the molecular electric dipole vector and the magnetic dipole vector. This also explains the microscopic origin of molecular chirality.

The third type of absorption spectroscopy that was utilized for this thesis is the electronic Stark effect. The Stark effect was discovered by Johannes Stark in 1913[59], when he found that the spectral line of hydrogen can split into symmetrical ones in a strong external electric field. This mechanism also applies to molecules. The absorption bands of the chromophores can be shifted to either higher or lower energies depending on their relative orientation to the external electric field, which is determined by the electronic orbital polarization. In anisotropic samples, this effect can be collective, and the spectral band shift reflects the individual chromophore's responses to the external field. In isotropic samples, the band shift to either direction shall lead to a spectral band broadening effect. As a special case, the chromophores in the reaction center protein are immobilized in the protein matrix, which provides both a natural probe and also a well-defined electric field (charges are localized on the chromophores). A

description of the mechanism and the expression of the Stark shift can be found in the introduction section of Chapter 3.

The opposite side of absorption is emission, which is categorized into spontaneous emission and stimulated emission. The stimulated emission process is simpler, because it is essentially a photon copy process, the photon that carries exactly the same energy as the energy gap size draws down an excited state particle to the ground state and emits another identical photon. Spontaneous emission is usually expressed as fluorescence. For particles of simple two-energy-level systems, the factors that influence the fluorescence intensity and lifetime are fully described by the rate equation and the Einstein relationship. Assuming thermal equilibrium, the radiation energy density in a confined cavity is given by Planck's formula:

$$\rho(\nu) = \frac{8\pi h n^3 \nu^3}{c^3} \cdot \frac{1}{e^{\frac{h\nu}{kT}} - 1} \qquad (6)$$

For a particle inside a cavity, the radiation field is the external electromagnetic wave. In order to achieve equilibrium, the number of absorbed photons must equal that of the emitted photons:

$$(A_{ba} + B_{ba}\rho(\nu))N_b = B_{ab}\rho(\nu)N_a \qquad (7)$$

where,

A_{ba} is the coefficient for spontaneous emission;

B_{ba} is the coefficient for stimulated emission;

and B_{ab} is the coefficient for stimulated absorption. In thermal equilibrium conditions, the population distribution of energy levels E_a and E_b satisfies the Boltzmann distribution, such that:

$$\frac{N_b}{N_a} = e^{\frac{(E_b - E_a)}{kT}} = e^{-\frac{h\nu}{kT}} \qquad (8)$$

Solving the above equations produces the ratio of the spontaneous emission coefficient A_{ba} to the stimulated absorption B_{ab}, such that:

$$\frac{A_{ba}}{B_{ab}} = \frac{8\pi h n^3 \nu^3}{c^3}$$

$$A_{ba} \propto \frac{8\pi h n^3 \nu^3}{c^3} (\vec{E} \cdot \overrightarrow{\mu_{ba}})$$

$$\propto \frac{32\pi^3 n}{3\eta\lambda^3} | \mu_{ba} |^2$$

The above expression suggests that the fluorescence intensity is not only proportional to the dipole strength in the absorption, but also emits stronger in shorter wavelengths ($\propto \nu^3$). The Einstein relationship for simple two-energy-level systems clearly does not apply to molecular systems in condensed phase (e.g. in solution), where the spectral line has been broadened to a spectrum. Similar laws, however, can still be derived for such situations. The fluorescence intensity F(ν), as a function of frequency, acts as a partition function to renormalize the ν^3 relationship, such that:

$$(\overline{\overline{\nu_f^{-3}}})^{-1} = c^3 (\overline{\nu_f^{-3}})^{-1} = \frac{\int F(\bar{\nu}) d\bar{\nu}}{\int \nu_f^{-3} F(\bar{\nu}) d\bar{\nu}}$$

$$\bar{\nu} = 1/\lambda = \nu/c$$

$$F(\nu) d\nu \propto \exp[h(\nu_{00} - \nu)/k_B T] (\frac{n(\nu)\nu}{c})^2 \varepsilon(\nu) d\nu$$

$$and, \ln[F(\nu)/\nu^2 \varepsilon(\nu)] \propto -h\nu/k_B T$$

Therefore, by plotting out $\ln[F(\nu)/\nu^2 \varepsilon(\nu)]$ versus frequency(ν), a straight line with slope $-h/k_B T$ should be resulted in, called the *Kennard-Stepanov* relationship. If excited molecules emit fluorescence before they reach thermal

equilibrium with the environment, the slope of the plot should be less than predicted. This approach is useful to reflect the conformational “hot” excited state prior to fluorescence emission, particularly at low temperature. This technique has been used to show that in some polar solvents, the Bchl-*a* molecules fluoresce from their ``hot'' excited state below a transition temperautre, which suggests a slow nuclear relaxation possibly pertinent to a conformational trapping phenomenon at low temperature (cited as a reference in Chapter 2).

The fluorescence emission spectrum of a molecule in solution usually has its peak at longer wavelengths compared to that of the absorption spectrum (Figure 13).

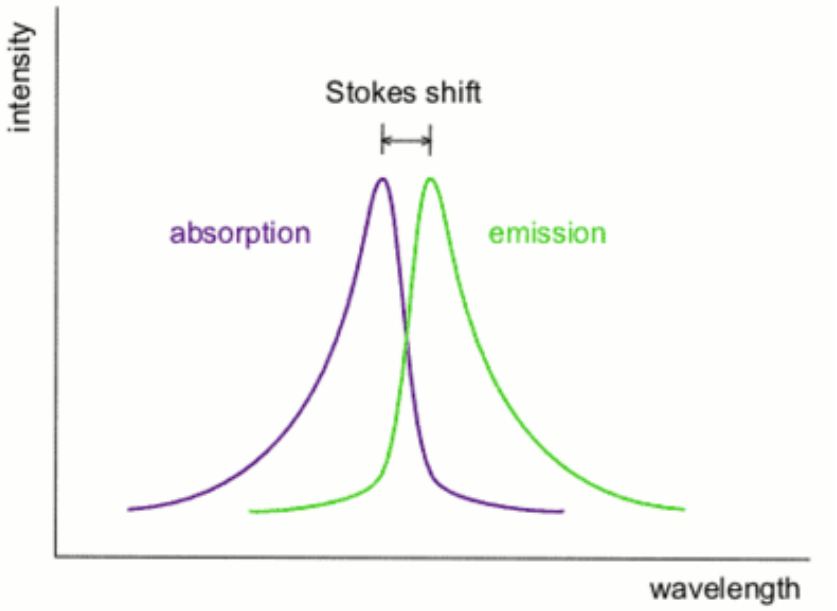

Figure 13: A general diagram demonstrating the concepts of fluorescence excitation and emission spectra. The Stokes shift is the distance between two spectral peaks.

This difference in peaks results from nuclear relaxation of the excited molecules, which dissipate energy into the environment during the fluorescence process. The red shift in the fluorescence peak is called the Stokes shift after George Stokes, who used UV light to excite mineral material and found visible light emission. The Stokes shift can have many origins, the most common of which include the intramolecular vibrational relaxations of the excited molecules and relaxations of the surrounding solvent. Other possibilities of the energy loss are excited state reaction, complex formation, and/or energy transfer. For the simplest intramolecular vibrational relaxation events, the magnitude of Stokes shift is assumed to be proportional to the reorganization energy (the electron-phonon interaction) between ground state and excited state. This concept has been further extended to the charge separated state to represent the reorganization energy associated with electron transfer, since the concept of Stokes shift generally represents some energy cost in the solvent environment resulted from an energy conservation of the entire system (solvent+solute). A painless application of the Stokes shift concept in electron transfer theory probably requires a perfect separation of “solvents” and “solutes” in both space scale and time scale. In terms of space scale separation, it implies a clear atomic division between so-called ``solvents'' and ``solutes''. The fluctuation of ideal ``solvents'' should be independent of the reaction occuring in the ``solutes'', which is the linear response assumption. For time scale separation, it means that the pace of spontaneous fluctuation of the ``solvent'' itself should be visible to the electron transfer time window to make it relevant for the reaction, otherwise it leads to a

so-called non-ergodic case. Realizing this point and the following corrections is crucial to accurately model non-equilibrium electron transfer in proteins[60].

If an excited molecule decays solely through fluorescence, its population would decrease exponentially over time. The spontaneous emission coefficient would be the decay rate, the inverse of its lifetime:

$$dN_a = A_{ba} N_b dt$$
$$\tau_{ba} = 1/A_{ba} = 1/k_{ba}$$

In practice, other decay mechanisms compete with fluorescence by exhausting the excited state population, thus decreasing the lifetime of the excited state. These mechanisms include triplet state formation (intersystem crossing, or k_{isc} for its rate), nonradiative decay to the ground state (internal conversion, or k_{ic} for its rate), energy transfer to other molecules(resonance energy transfer, or k_{rt} for its rate), and electron transfer (k_{et} for its rate). The total rate is a sum of all those above:

$$k_{total} = k_{ba} + k_{isc} + k_{ic} + k_{rt} + k_{et} + \Lambda \qquad (9)$$

The fluorescence yield ϕ from a homogeneous sample is then proportional to the fluorescence lifetime, because:

$$\phi = \frac{photons\ emitted}{photons\ absorbed} = \frac{k_{ba}}{k_{total}} = \frac{\tau}{\tau_{ba}} \qquad (10)$$

In addition to fluorescence, another photon emitting process is phosphorescence, which is the photon emission from a different electronic state, the triplet state. The dipole-light electric field interaction does not drive the

transition between singlet and triplet states, as this is forbidden by the selection rule. When a molecule is raised to an excited singlet state, relaxation into a triplet state often occurs with lifetime constants ranging from tens of nanoseconds to microseconds. The triplet state is energetically lower than the excited singlet state, but higher than the singlet ground state. When triplet state molecules return to the singlet ground state, photons are emitted as phosphorescence. Because the energy gap between the triplet state and the singlet ground state is much smaller than that of the excited and ground singlet states (spin-orbit coupling term), the decay rate is also much slower. Typical lifetimes of excited triplet states range from 10^{-5} s to more than 1 s. In the reaction center, the P^* triplet state $^3(P^*)$ decays in 6 μs at room temperature, which largely reflects a quenching by the carotenoid. Although phosphorescence process is slow, it is typically 10^6 times weaker than fluorescence which makes it difficult to measure. One technique called “delayed fluorescence” can be used to study the energy level difference between the triplet state and the ground state, which is realized by utilizing a backward thermal excitation of the triplet state back to the excited singlet state. This approach also has other applications, like being used to examine the energies and dynamics of metastable states that are created photochemically through electron transfer or other processes. In reaction center protein, those charge separated states experience thermal equilibrium and relax. As a reverse of this process, some small populations of charge separated states at low lying energy states also become excited to higher ones until the excited state via thermal equilibrium. The re-emission from those re-populated excited state reaction centers also provide some

information about the thermal equilibrium process between the charge separated state energy levels.

Each type of electromagnetic field and molecule interactions can be used to study the photochemistry of the reaction center from one aspect. Of course, this has some merits, for example, the fluorescence spectroscopy itself only involves the photons emitted from excited state to the ground state transition population, without other signal source. Simutaneous recording of other spectroscopy signals clearly will provide more information, and will be particularly powerful if all those spectroscopies are synchronized to detect the same photochemistry events. The pump-probe technique provides such a possibility, in which both the absorption change and stimulated emission change signals are indiscriminately treated as transmitted light intensity change signals received by the detector. If the overlap between the absorption spectrum and the stimulated emission spectrum from one molecule is not significant, then it is possible to find some wavelengths to characterize them individually. In a typical pump-probe experiment, a sample is excited with a pulse with frequency ω_1 and wavevector k_1, and is then probed by a second pulse with frequency ω_2 and wavevector k_2. The optical path of one of the pulses is varied to change the delay between the two pulses. The measured signal is the difference between the intensities of the transmitted probe pulses in the presence and in the absence of the excitation pulses, and usually is averaged over many pulses. In a system with only two electronic states, the difference can reflect either stimulated emission from the excited state or bleaching of the absorption band of the ground state. The reason is because of the indiscrimination

of the absorption and the emission signal sources in this technique, which has been narrated above. In a three-state system, formation of the third state (c) can induce an excited-state absorption signal (excitation from state b to state c), in addition to the stimulated emission signal or ground-state bleaching signal, if the $b \rightarrow c$ transition is allowed by the selection rule.

Spectroscopy data generally takes two or three dimensional forms (even more dimensions are possible, but are usually studied individually). For the simplest two dimensional case, the form of the rudimentary data is usually the transmitted light intensity as a function of wavelength. If the absorption is being measured, the transmitted light intensity is then replaced by a quantity A (absorbance, unit in optical density, OD) which can be directly be related to the molar absorption coefficient. This is achieved by relating the absorbance to Beer-Lambert law:

$$I = I_0 \exp(-\varepsilon' C l) = I_0 10^{-\varepsilon C l} \equiv I_0 10^{-A} \qquad (11)$$

In pump-probe experiments, the signals are all measured as difference signals (before pump and after pump). The signals are then normalized to the before-pump light intensity:

$$\Delta A = A - A_0 = -\log\left(\frac{I}{I_0}\right) \qquad (12)$$

In a three dimension spectra collection, the extra dimension can be time axis, which makes it a time-resolved spectrum. All spectra are measured by accumulating photons over time intervals. The difference between a two

dimension steady state spectrum and three dimension time-resolved spectra is the length of integration time, where the integration time for a steady state spectrum is long enough to pass and ignore all the short-lived intermediate states and the integration time for three dimension spectra is cut into small windows and witnesses a continuous change in the photoactive components. There are other physical quantities that can be used for the extra dimensions, like temperature, pH or even excitation intensity, which will provide more complex parameter-dependent studies.

5 Interpreting the experiment spectrum to understand photochemistry events

There are some commonly-used terms in spectroscopy to describe certain photochemistry events. One of them is ``bleaching". It refers to a population depletion of certain light absorbing species (if it absorbs in the visible region, then the outcome is “removal” of the color window). In the reaction center, excitation of the dimer will result in a bleaching of the ground state absorption band centered at 865 nm. In the difference spectrum, the bleaching of the dimer will show itself as a negative band signal (Figure 15).

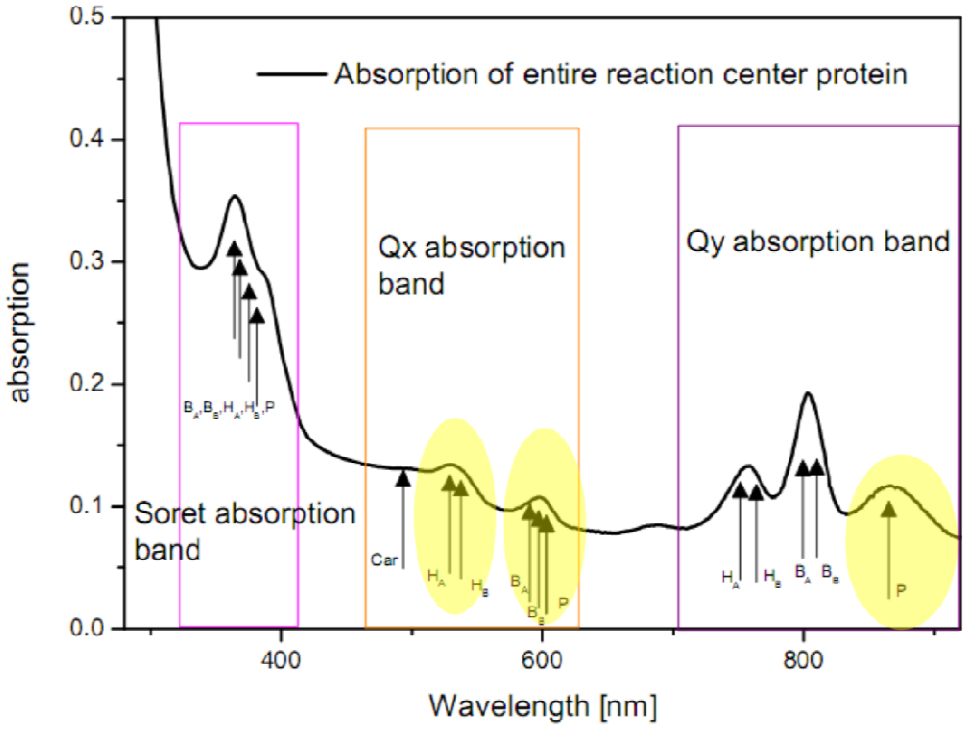

Figure 14: The ground state absorption spectrum of the *Rb. sphaeroides* wild type reaction center in the 280-920 nm wavelength region. Different transition regions are correspondingly grouped in a rectangular box (from left to right): Soret band (300-420 nm), Qx band (460-700 nm), and Qy band (700-920 nm). The absorption bands have been assigned to the electronic transitions contributed by each cofactor.

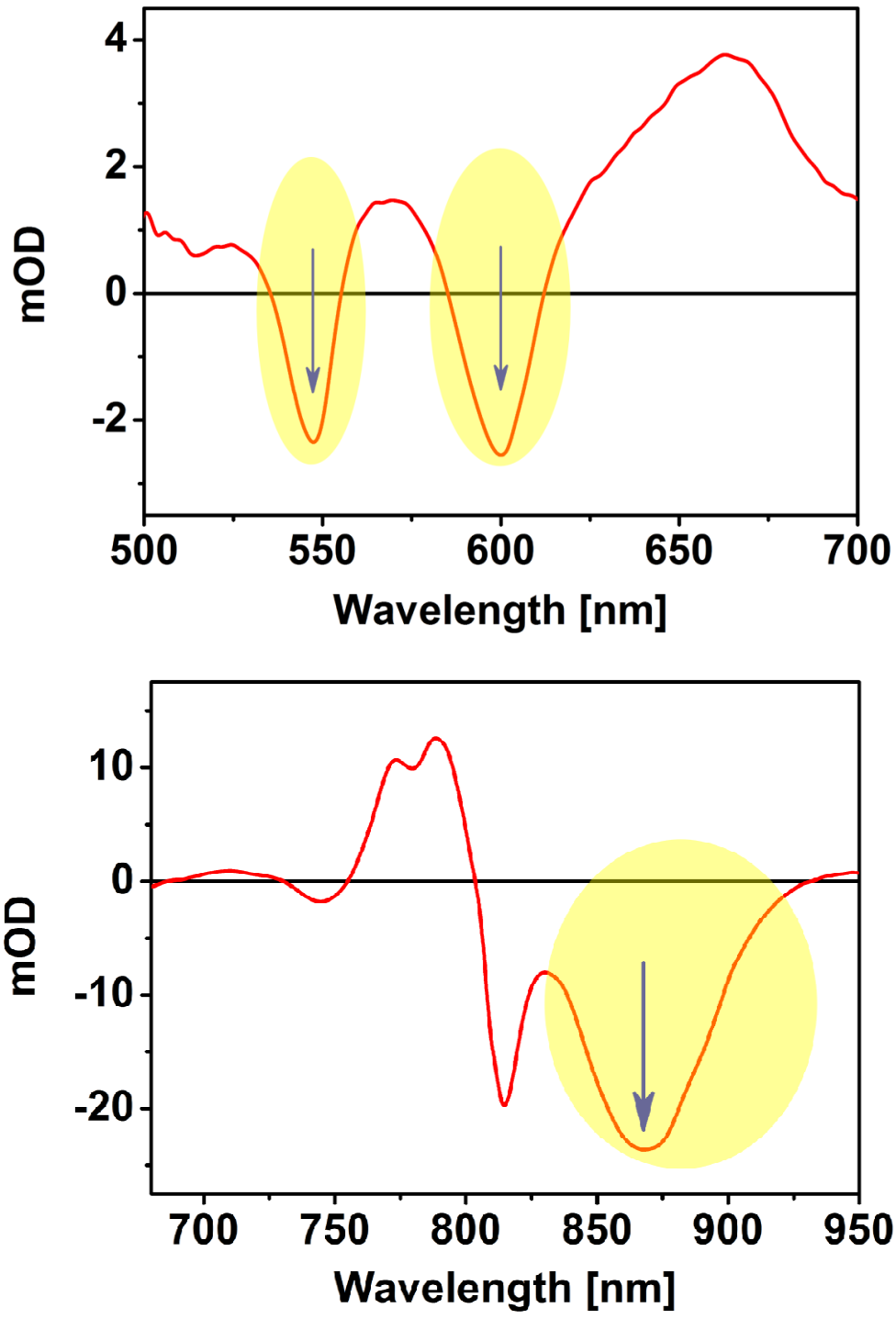

Figure 15: Difference absorption spectra recorded for the *Rb. sphaeroides* wild type reaction center in the Qx and Qy spectral bands (top graph and bottom graph, respectively), 10 ps after light excitation at 860 nm. The highlighted areas correspond to the highlighted absorption bands in the ground state absorption spectrum shown in figure 14.

To interpret the time resolved spectra and translate it into photochemistry events, a concrete example would be beneficial. Again, the electron transfer process in the reaction center protein is taken as an example to explain its correspondence to the time resolved spectra. In Figure 16, the transient absorption spectra in both the Qx and Qy spectral band regions were recorded at time delays of 1 ps, 10 ps and 6 ns after light excitation. The spectral features at these time delays majorly represent the corresponding electronic states: P*, $P^+H_A^-$, and $P^+Q_A^-$. At the initial moment, 1 ps, the excited state P* should reflect two events: the disappearance of P from the ground state, and the appearance of P*. The first event shown clearly in the absorbance change of both the Qx and Qy bands, where a ground state bleaching of P was observed (centered at 595 and 865 nm). The second event is normally expressed as a broad absorption of P* (excited state absorption due to an excitation to higher excited states P** from P*,), which does not appear to be significant in either spectral region, except for a slight absorbance change in the 800 nm region. It is also noteworthy to point out that a significant negative band--representing the generation of stimulated emssion-- overlaps with the P ground state bleaching in the Qy region (850-930 nm, more apparent when compared with the following 10-ps spectrum). Such stimulated emisson is linked to a simutaneous depletion of P* population caused by the $P^* \rightarrow P^+H_A^-$ photochemistry event occuring at this time scale. When the electron transfer proceeds to the $P^+H_A^-$ state (see 10-ps spectrum), similarly, the disappearance of the P and H_A states should be observed, and the appearance of the P^+ and H_A^-

states, becomes apparent. In the Qx and Qy spectral regions, these events appear as a bleaching of the 865 nm band (P ground state, Q_y),the 760 nm band (H_A ground state, Q_y), the 600 nm band (P ground state, Q_x), and the 540 nm band (H_A ground state, Q_x). At the same time, an absorbance increase near 660 nm (H_A^- absorption) represents an increase in the H_A^- anion population. The P^+ absorbance increase does not have an obvious contribution in either of the spectral regions currently being shown in figure 15 (500-750 nm or 700-950 nm). The final state $P^+Q_A^-$ can be analyzed in the same way as the $P^+H_A^-$ state, except that the Q_A/ Q_A^- states are basically silent in the current spectral region (Q_A/Q_A^- has absorption change around 250-280 nm[61]), leaving only the P ground state bleaching feature available. Because all three electronic states have their distinct spectral features, it is not difficult to separate them apart by looking at all of the spectra covering both wavelength regions (500-750 nm or 700-950 nm).

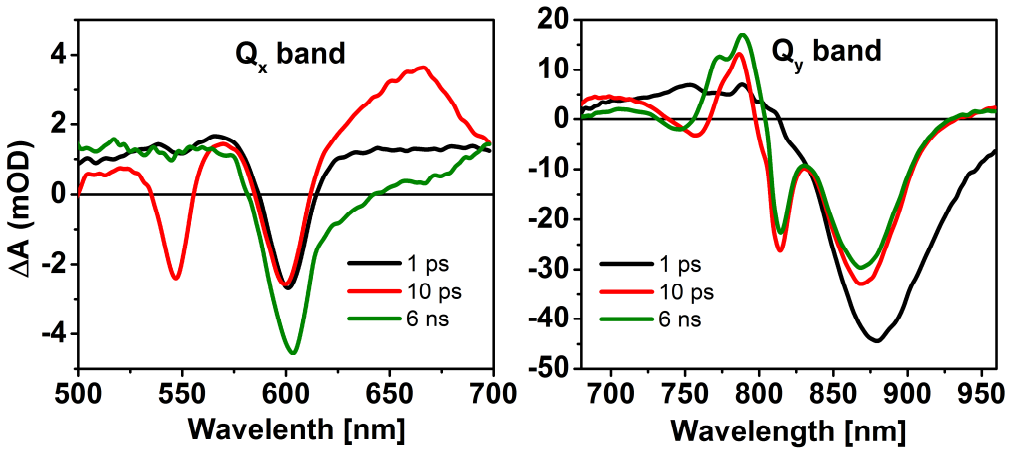

Figure 16: Time-resolved spectra of the *Rb. sphaeroides* wild type reaction center in the 500-700 nm spectral region (left), and the 680-960 nm (right) spectral

regions, at 1 ps (P^*), 10 ps ($P^+H_A^-$) and 6 ns ($P^+Q_A^-$) after laser excitation at 860 nm

As noted previously, the time resolved spectrum is often presented in either two dimensional or three dimensional formats. For two dimensional data, the kinetics can directly be related to the undergoing chemical reactions. Because many elementary chemical reactions follow an exponential relationship (either follows Arrehnius law or Marcus formula for electron transfer reaction), and more complex reactions can often be treated as a series of elementary chemical reactions, or phenomenologically, as a summation of several exponential decays. Therefore, the conventional approach involves performing multiexponential analyses to extract all of the decay lifetimes. Mathematically, there are a number of ways to implement this analysis, from a straightforward least-square fit based on assumed parameters to more parameter-independent approach by resorting to integral transform. The straightforward least-square fit, also known as the Grinvald-Steinberg re-convolution method[62], is adopted in the ASUFIT software (www.public.asu.edu/laserweb/asufit). This method utilizes a plausible functional form for the decay data (here it is a combination of several exponential functions) and adjusts the parameters until the statistical error between the fitting data and the experimental data is minimal to achieve the best fit. In the practice of fitting luminescence decay data, this is separated into two steps: convolution and fitting. Suppose that $F(t)$ is the experimental decay data, it will be equal to a convolution of the instrument response of the excitation light flash $G(t)$ and the physical decay function from the sample, $i(t)$:

$$F(t) = \int_0^t G(t-s)i(s)ds \qquad (13)$$

The critical study by Knight and Selinger has concluded that the de-convolution of $F(t)$ without a *priori* assumption concerning the functional form of $i(t)$ is not practical[63]. How to determine a proper functional form that is model-independent, when fitting low signal-to-noise ratio data, has been a long-standing question. Take multiexponential form for example, the room mean square deviation, RMS, of the following two expressions (Figure 17):

$$f(t) = \frac{1}{3}\exp(-t/2) + \frac{1}{3}\exp(-t/3.5) + \frac{1}{3}\exp(-t/6) \qquad (14)$$

$$g(t) = \frac{1}{2}\exp(-t/5.46) + \frac{1}{2}\exp(-t/2.26)$$

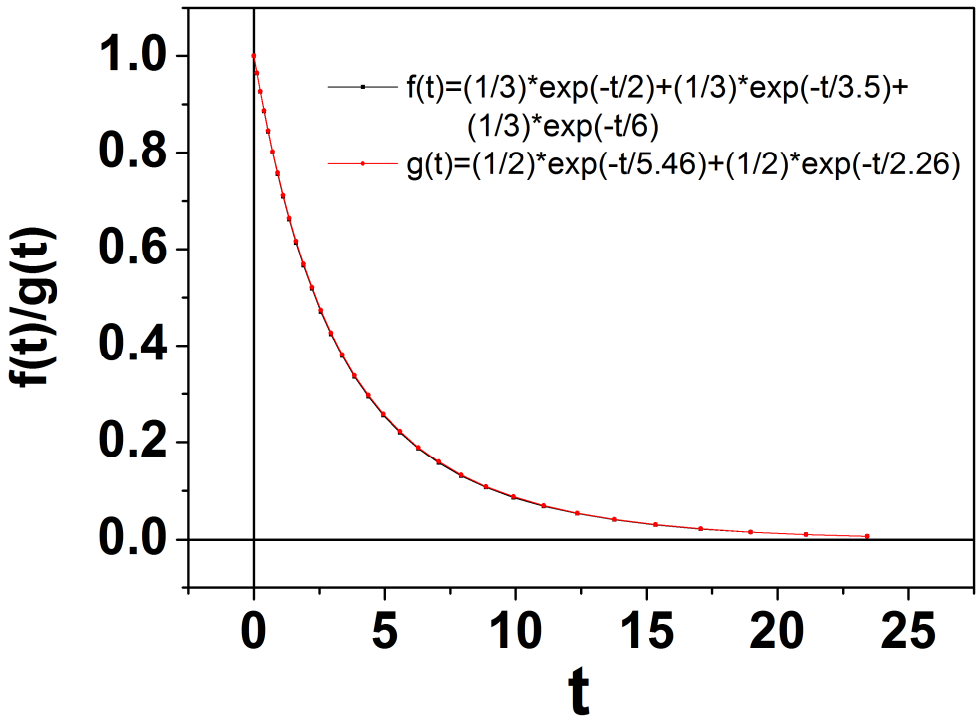

Figure 17: Overlay of discrete sampling of two function forms (f(t) and g(t), in equation 14), where t is ranged in [0, 30].

is as low as 2.1×10^{-4}, which means that if the noise level of the experiment data is larger than this value, there is an intrinsic difficulty when attempting to differentiate them simply from the experiment data itself. Such parameter uncertainty can only be solved by retrieving physical information about the system. Once a prescribed functional has been decided, in the fitting stage, the error between the convoluted fitting data and the experimental data is evaluated as:

$$\Phi = \sum_{i=1}^{n} \omega_i [F_c(t_i) - F_o(t_i)]^2 \qquad (15)$$

$$\omega_i = \frac{1}{\sigma_i^2} \Big/ \frac{1}{n} \sum_{i=1}^{n} \frac{1}{\sigma_i^2} \qquad (16)$$

The symbol ω_i represents the square deviation of the each point because, from a statistical standpoint, greater weight should be given to points where the variance of the experimental observation is small. In some simplified cases, particularly if each single data point measurement is not statistical (typical statistical case is photon-counting technique) but rather is a one-shot record (like a single kinetic trace in pump-probe experiments), the weighting factor ω_i can be ignored. The residual Φ can often appears as other symbols, such as the Chi-square χ^2, in literature.

Aside from the absolute error threshold, the residual pattern of the fitting is also important for evaluating the fitting quality. Ideally, the function $F_c(t_i)$, that describes a fluorescence decay process, would have the experimentally determined points, $F_o(t_i)$, scattered about it in a random fashion. Markedly

different analytical expressions used to describe the decay process might result in very similar values for Φ; however, the residual from the wrong expression could lead to a non-random distribution, which is explained in figure 18.

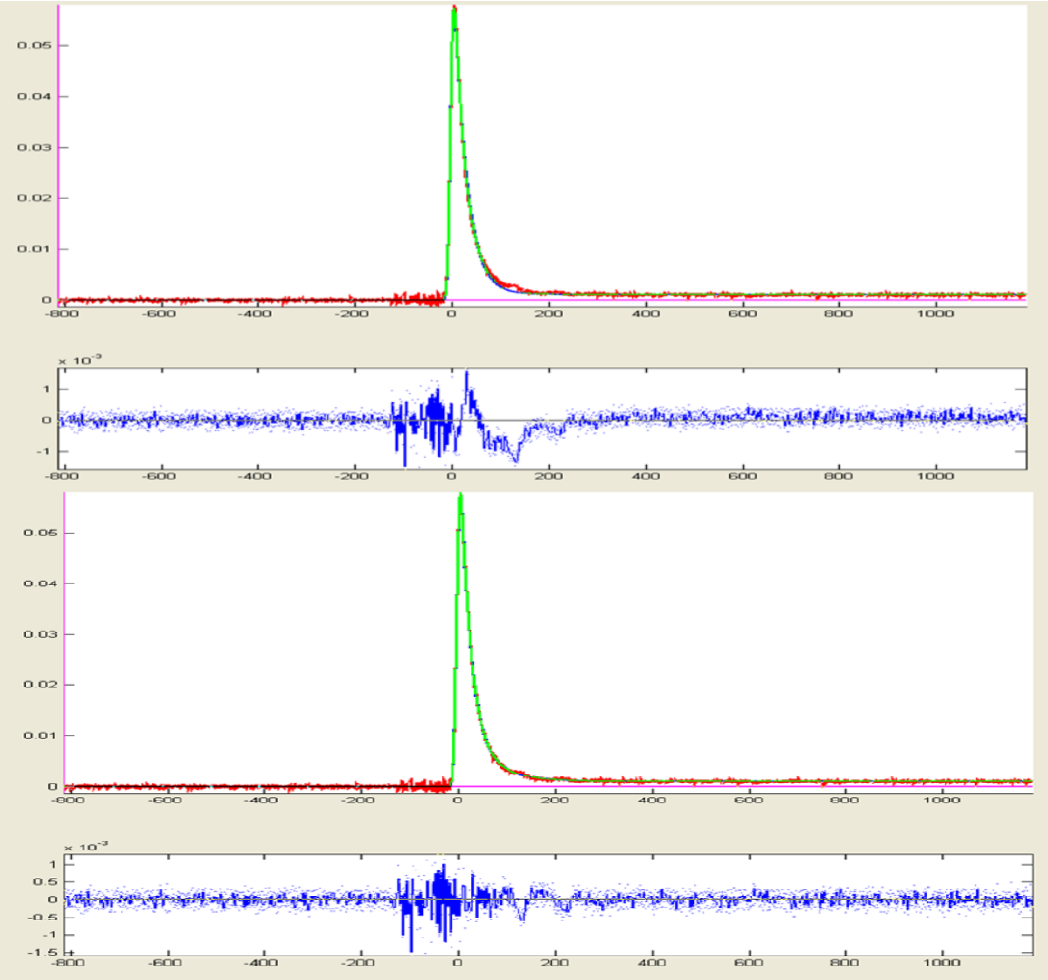

Figure 18: A kinetic curve measured in a photolysis experiment, fitted with a single-exponential function (top graph) and the same kinetic curve fit with two expoentials (bottom graph) Residuals for each graph are shown beneath the graphs. The top graph shows a non-random residual pattern, while the bottom graph shows a random residual distribution during the whole time course.

Randomness of the scattered experiment data points from a proposed function can be evaluated using the autocorrelation function of the residuals, which is defined as:

$$C(t_j) = \frac{1}{m} \frac{\sum_{i=1}^{m} (\omega_i)^{\frac{1}{2}} \Delta_i (\omega_{i+j})^{\frac{1}{2}} \Delta_{i+j}}{\frac{1}{n} \sum_{i=1}^{n} \omega_i \Delta_i^2} \qquad (17)$$

Overall, the least-square fit is an iterative approach, and its convergence to the global minimum is largely dependent upon the number of parameters in use and the initial parameter guessing. New approaches have developed in recent years that improve the initial parameter guessing simply through examination of the experiment data. These approaches employ the integral transform technique and use different stabilization techniques to address the numerical stability difficulty in the inverse Laplace transform. Two popular methods include Tikhonov regulation[64-66] and maximum entropy[67, 68], and one recent method (phase function approach[69]) invokes the Kramer-Kronig relation to recover the parameters with success. After the transform, the function is the rate constant distribution in a continuous form. Some non-iterative methods have also been applied to multiexponential analysis[70]. For a conventional approach like the Grinvald-Steinberg method, unless there is a very clear physical explanation for appending more exponentials to improve the fit, the fitting should stop at the statistical level described above. When the number of exponentials increases, the discrete rate constants can be less useful and the explanation for each of them can also be problematic. One way to alleviate the problem with this limit is to use the stretched exponential function for phenomenological descriptions, or the Kohlrausch-Williams-Watts (KWW) function:

$$f(t) = e^{-(\frac{t}{\tau})^{\beta}} = \int_0^{\infty} e^{-\frac{t}{\tau}} \rho(\tau) d\tau \qquad (18)$$

Here, τ is the characteristic time constant in the relaxation distribution, the index, β, is associated with the width of the distribution, or the variety of the relaxation processes. If β approaches 1, the decay process distribution approaches a Dirac function and the decay becomes essentially single exponential. When β decreases, the distribution of exponential decay times becomes broader, and the average lifetime produced by such a distribution is:

$$< \tau >= \beta\tau \cdot \Gamma(\beta) \qquad (19)$$

where $\Gamma()$ is the gamma function. The physical origin of multiexponential decay can be various. At least two physical mechanisms can both result in this phenomenological law[71]. Interestingly, both physical models summarized in the amorphous system have their own corresponding mapping to the existing explanations for the non-Arrehnius electron transfer decay rate in the reaction center protein. In the first model, many parallel channels decays were used to explain the static defects in the amorphous medium, and this explanation was mapped to the explanation of reaction center heterogeneity in early studies. The second model requires that the relaxation follows a hierarchical structure: certain low level relaxations can only relax after the completion of the higher level ones. This model is a mapping of the hierarchical protein energy landscape. It is also worthy to point out that the behavior of β and τ as a function of temperature or pressure can be used to determine which mechanism dominates[71]. In Chapter 2, the temperature dependence of β and τ suggests that the second explanation is more likely.

Data from the measurements in both dimentions: time (t) and wavelength (λ), provides more redundant information to reduce the uncertainty in single wavelength measurements. Particularly, for those spectral multichannel measurements, the detection of decay traces at a great number of wavelengths is performed simutaneously, allowing for low noise statistics. Many methodological reviews demonstrate the importance of simultaneous (global) analysis of multiple decay traces[72-75]. The combination of global analysis with testing of a photo-physical or photochemical model is often called target analysis. In time-resolved experiments, the recorded time- and wavelength-dependent data can be related to the molecular processes using the framework of the transient spectroscopy theories. If the time constant of the reactions is longer than the oscillation periods of the relevant molecular vibrations, one may assume that the absorption changes originate from intermediates with spectroscopically well-defined properties. Under these conditions, only exponential processes are present, and the populations of the various intermediates follow the equation:

$$\frac{dN_i(t)}{dt} = -\sum_{j=0}^{n} k_{ij} N_j(t) \qquad (20)$$

The symbol n is the number of intermediate states;

$N_i(t)$ is the population density of intermediate I_i at time t;

and k_{ij} is the rate constant for population transfer from I_j to I_i.

On the other hand, the spectroscopic properties of a mixture of intermediates are a superposition of the same properties weighted by their concentrations. In absorption this is known as the Beer-Lambert law (a forementioned above). Thus

the noise-free, time-resolved spectrum $A(t, \lambda)$ is a superposition of the contributions of the n_{comp} different components (intermediates):

$$A(t, \lambda) = \sum_{l=1}^{n_{comp}} c_l(t)\varepsilon_l(\lambda) \qquad (21)$$

where $c_l(t)$ and $\varepsilon_l(\lambda)$ denote the concentration and spectrum of component *l* respectively. Typical values for the number of components which can be studied with time-resolved spectroscopy are $1 < n_{comp} < 10$. According to equation (21), the time and wavelength properties are separable, and ΔA can be written as a sum of exponential functions:

$$\Delta A(\lambda, t) = \frac{l}{ln(10)} \sum_{j=1}^{n} \{ \sum_{i=1}^{n} [\sigma_i(\lambda) - (\sigma_0(\lambda))] N_{ij} \} e^{-\frac{t}{\tau_j}} \qquad (22)$$

The symbol *l* is the pathlength in the sample;

τ_j is the eigenvalues of the rate constant matrix k_{ij} ;

and $\sigma_i(\lambda)$ is the absorption cross-section of the intermediate I_i at λ.

The matrix N_{ij} depends on the rate constant matrix k_{ij} and on the initial conditions generated by the excitation process. The investigatory goal of this thesis is to understand the microscopic properties of the electron transfer. The primary experiment result concerns the number n of intermediate states involved, a parameter that is equal to the number of detected time constants τ_j . This

determination requires a decomposition of the time dependence of $\Delta A(\lambda,t)$ into exponentials:

$$\Delta A(\lambda,t) = \sum_{j=1}^{n} a_j(\lambda) e^{-\frac{t}{\tau_j}} \qquad (23)$$

Combining (22) and (23), the amplitudes contain information on the difference cross-section spectra of the intermediates and the initial ground state in a rather complex form:

$$\sigma_i(\lambda) - \sigma_0(\lambda) = \frac{ln(10)}{l} \sum_{j=1}^{n} a_i(\lambda)(N_{ij})^{-1} \qquad (24)$$

The difference spectra can only be determined for a known matrix N_{ij} . However, the calculation of N_{ij} requires the complete rate constant matrix k_{ij} . One obtains the decay rates, i.e. the eigenvalues of this matrix, via experiments. But the determination of the complete matrix from the eigenvalues is not possible without making assumptions on the reaction scheme.

Measurement of $A(\lambda,t)$ in equation (21) poses the inverse problem: how to recover the spectroscopic and kinetic (dynamic) properties of the components from the data. In practice various problems can arise: first, the number of components present in the system may be unknown; secondly, in general neither the concentration profiles $c_l(t)$ nor the spectra $\varepsilon_l(\lambda)$ are known. However, the experimentalists typically have a priori knowledge about which concentration profile shapes or spectra are realistic. This knowledge often amounts to common statements regarding continuity, non-negativity, and unimodality, etc.

When a priori knowledge about a detailed kinetic model is available, a linear-invariant compartment model can be used. The global analysis is equivalent to a number of noninteracting, parallel decaying compartments. In this situation, equation (20) is converted into a simplified case, where the off-diagnonal part of the rate matrix k_{ij} is ignored:

$$\frac{dc_j(t)}{dt} = -\sum_{j=1}^{n} K_j c_j(t) + s_j(t) \qquad (25)$$

Input to the system is described by vector $s(t) = i(t)[1 \quad x_2 \quad \ldots \quad x_{n_{comp}}]^T$, where x_l represents a possible extra input to compartment l, and i(t) is the instrument response. The essential step of this approach is to make an initial guess of K vector, and then the concentration evolution of each compartment is simply given by $c(t) = e^{Kt} \oplus s(t)$ through iterative convergence to the experiment spectrum. When the kinetic data is fitted with a sufficient number of exponential decays, and their amplitude $\varepsilon(\lambda)$ is called Decay Associated Spectra (DAS). Note that in general the DAS do not correspond to real spectra; this is only the case when a component decays without interconversion to other components, some times the DAS are also termed as the Decay Associated Difference Spectra (DADS).

Along with the global analysis of independent decays (1| 2| ...| n_{comp}), the simplest kinetic scheme is the unbranched, unidirectional model ($1 \rightarrow 2 \rightarrow \ldots \rightarrow n_{comp}$). Those two types of models are also termed parallel and sequential, respectively (here for model, we are still refering to mathematical model, not physical model). In the sequential model, back-reactions are ignored on the assumption that the

energy losses are large enough to block the reverse reaction rates. Note the assumption that there are no losses in the chain $1 \rightarrow 2 \rightarrow ... \rightarrow n_{comp}$, and the compartmental model for all the n_{comp}compartments in equation (25) can be solved to yield:

$$c_l(t) = \sum_{j=1}^{l} b_{jl} \exp(-k_j l) \oplus i(t) \qquad (26)$$

where k_j is the decay rate of compartment j and the amplitudes b_{jl} of the (convolved) exponential decays are defined by $b_{11} = 1$ and thus for $j \leq l$:

$$b_{jl} = \prod_{m=1}^{l-1} k_m / \prod_{n=1}^{l} (k_n - k_j)_{n \neq j} \qquad (27)$$

The spectra resolved for each compartment in this method are called Evolution Associated Difference Spectra (EADS). Like the DAS, in general the EADS do not correspond to real spectra,

The parallel model and sequential model are the mathematical models that will be frequently used in this thesis. There is essentially no physical information in the two models, and as such they are different from the ``target analysis" which has clear physical pathways including branching and bidirectional rates. However, because of the simplicity in those two approaches, it is possible to interpret the DAS and EADS from the real spectra as a combination of several physical spectral components. With simple systems the interpretation of the DADS or EADS can be straightforward. For example, when a sequential model with increasing lifetimes represents the correct physicochemical picture, the EADS correspond to true Species Associated Difference Spectra (SADS), which

characterize the intermediate states. In that case the DADS represent the decay and rise of these states.

One nice thing about the electron transfer processes in the reaction center is that the average lifetime of each step is widely separated by at least one order of magnitude (e.g. in the *Rb. sphaeroides* wild type reaction center, 3 ps, 200 ps, and >10 μs are found in figure 8), which make them separable using either global analysis (DAS) or sequential analysis (EADS). The DAS and EADS analysis with three states have clearly resolved three electronic states: P^*, $P^+H_A^-$, and $P^+Q_A^-$. The inter-conversion lifetime constants associated with those states match well with previously known values (figure 8). The spectral features corresponding to each electronic state are also consistent with the observation in the transient absorption spectra (figure 19, and for the transient absorption spectra see figure 16). The major difference between figures 19(A) and 19(B) is in the first two states (4 ps and 200 ps). The non-decay states (represents the $P^+Q_A^-$ state) are identical from both the global and sequential analysis methods. In the global analysis approach, the DAS of the 4.2 ps component features an absorption decrease of the H_A (centered at 545 nm), and an absorption increase of H_A^- (center at 660 nm), together with a minor derivative-shaped spectral feature in the 575-625 nm region. The DAS feature here suggests an electron transfer event from P* to H_A, thus converting it to anion form.

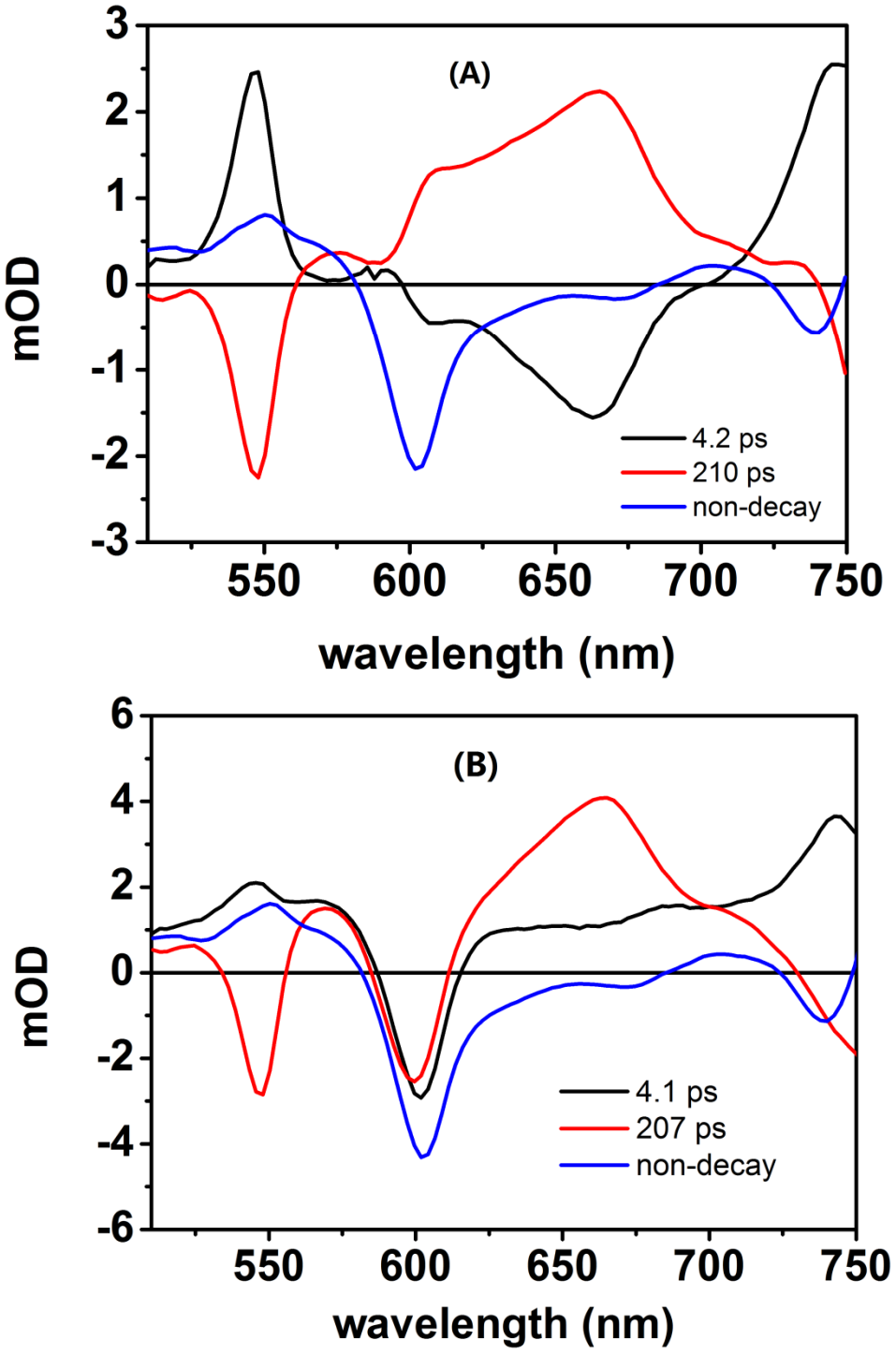

Figure 19: (A) DAS from a global analysis based on transient absorption spectra in the 500-750 nm spectral region covering a 0-6.5 ns delay after light excitation

on the *Rb. sphaeroides* wild type reaction center; (B) EADS from a sequential analysis based on the same data set.

The reason for seeing the appearance of derivative-shaped features in the spectra is not yet clear, which could be related to the Stark shift of the neutral chromophores (more likely B_A or B_B) due to a building up of an internal field associated with $P^+H_A^-$ state. The DAS decaying with a 210 ps time constant is a mirror to the 4.2-ps DAS, which suggests a recovery event of $H_A^- \rightarrow H_A$ upon electron transfer to the quinone. This speculation about the origin of the derivative-shaped feature in the 3-ps DAS can be somehow vindicated by the 200-ps DAS, as coming along with the retreat of the electron reside on H_A, the attenuation of the field causes the B_A (or B_B) spectrum to shift back. The final non-decay state exhibits a prominent bleaching at 600 nm, representing a bleaching state of P in the $P^+Q_A^-$ state. The EADS produced by sequential model analysis describe the same processes as DAS, yet they represent the spectral progression landmarks of difference states as apposed to emphasizing the simutaneous decay processes from initial states. The EADS that decays with a lifetime of 4.1 ps is clearly dominated by the spectral feature of P*, because only a strong bleaching at 600 nm has been observed. The following 207-ps EADS is very similar to the transient absorption spectra observed near 10 ps for the $P^+H_A^-$ state (refer to figure 16), and indeed, as seen in the population evolution kinetics, the maximum population occupancy of this state occurs around 10-20 ps (figure 20).

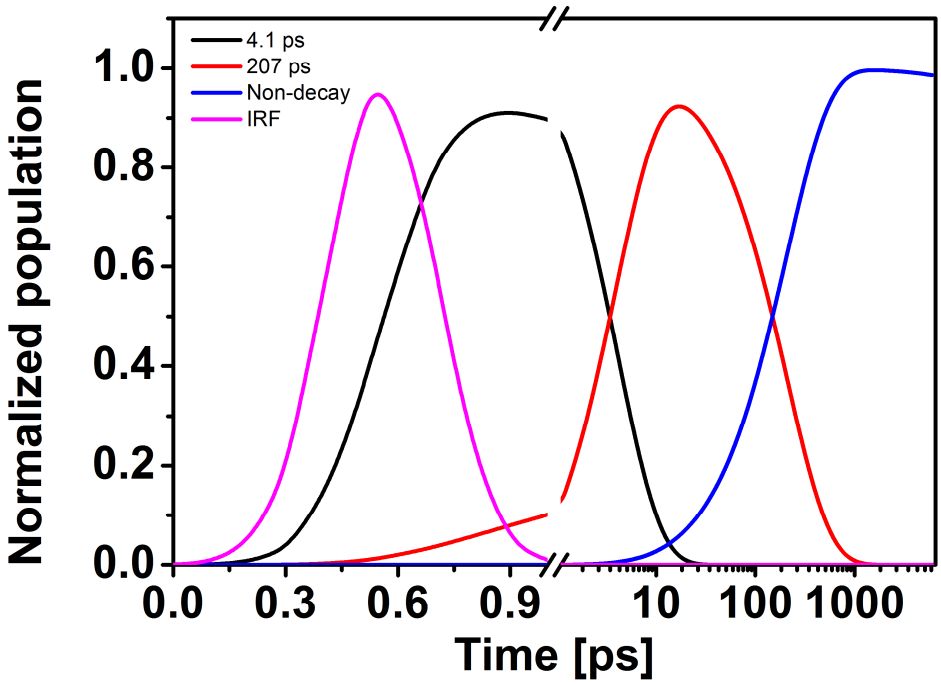

Figure 20: Normalized population evolution kinetics of each state solved in the sequential model analysis (figure 19B). The graph uses a semi-log scale, and the linear region is truncated after 1 ps. The initial gaussian peak (magenta) is the instrument response function (IRF).

6 Electron transfer, Marcus theory, and the reaction diffusion model

Electron transfer is a mechanistic description of the thermodynamic concept of the redox process. In a concrete picture, the electron moves from one atom or chemical species (e.g. a molecule) to another, during which the oxidation states of both reactants change. Early theory development focused on the chemical and electrochemical electron transfer. In the above two types, on many occasions, the reactions are largely diffusion controlled. Marcus first developed an approach to calculate the reaction rate as a function of the free energy of the system by connecting it to the transition state theory in a dielectric continuum background. The reaction system is composed of three elements: reactant,

product, and solvents. In order to make the reaction rate calculation tractable, the solvents were treated as a dielectric continuum. In the transition state, the position-dependent dielectric polarization of the solvents is considered as independent of the reactant or product states, or in other words, as background fluctuation. The electronic polarization for the solvent molecules can rapidly respond to those nuclear fluctuations. By introducing a so-called "reorganization term", λ, the reaction rate k can be written into a very elegant manner:

$$k = A\exp\left[-\frac{\Delta G^*}{k_B T}\right] \qquad (28)$$

$$\Delta G^* = \frac{\lambda}{4}\left[1+\frac{\Delta G^0}{\lambda}\right]^2 \qquad (29)$$

The A in equation (28) is a term dependent on the nature of an electron transfer reaction, either inter-molecular or intra-molecular. The term ΔG^0 is the standard free energy of reaction. The reorganization energy λ can take different expressions in different systems, which will be described in detail below. The above formula can also be derived from two parabolically shaped free energy curves as a function of a certain reaction coordinate that connects the reactant and the product (figure 21).

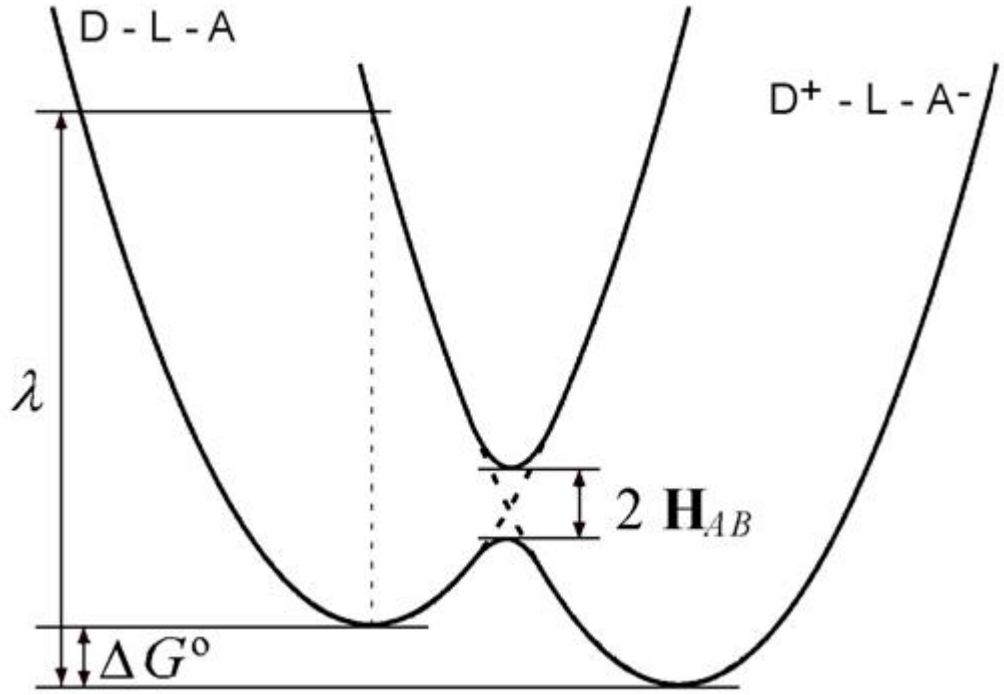

Figure 21: Free energy parabolas and the associated parameters in Marcus theory. The X axis is the reaction coordinate associated with the electron transfer, Y axis is the Gibbs free energy. ΔG° is the free energy gap, λ is the reorganization energy, and H_{AB} is the electronic coupling. Figure is taken from wikipedia (http://en.wikipedia.org/wiki/Marcus_theory)

The free energy is the vertical distance from the valleys of two parabolas. The reorganization energy is the configuration energy cost of moving the vertically excited reactant at condon approximation along the product reaction coordinate to the lowest free energy state. The sum of them is the activation energy, which is the energy cost of moving the lowest free energy reactant state along the reactant reaction coordinate to the crossing point of the two parabolas.

An important assumption underlyng the standard Marcus theory is that the nuclear configurations and the charge distribution are always “in equilibrium”, indicating that there exists only one transition state and only one reaction coordinate is sufficient to describe the reaction. In principle, the standard Marcus model is a macroscopic, thermodynamical model, not suitable for reactions that involves multiple microscopic states.

Another noteworthy thing in applying the Marcus theory is the difference in intra-molecular electron transfer and inter-molecular electron transfer, also referred to as inner-sphere electron transfer and outer-sphere electron transfer, respectively. Their difference is manifested in the pre-coefficient “A” in equation (28), which is associated with the electron coupling. Intra-molecular electron transfer has a stronger electron coupling, and normally decays exponentially with distance, while the electron coupling in inter-molecular electron transfer is usually given by the wave function overlap of the donor-acceptor (dipole-dipole interaction in the classical limit). More specifically, if the system of the reactant is coupled too tightly during reaction and the activated complex needs to be treated as an integral entity, in ab-initio quantum mechanics detail, or in other words, nothing in this system can be treated macroscopically as ``solvent'' environment, then the exponential part in expression (28) becomes less important as the free energy difference of the reactant and the product in this system equals zero in terms of the “self-exchange reaction” scenario[76].

The analytical expressions for the electron transfer in intra- and inter-molecular electron transfer usually appear in the following form:

$$k_{ET} = \frac{J^2}{\eta}\sqrt{\frac{\pi}{\lambda k_B T}} \cdot e^{-\frac{(\lambda+\Delta G)^2}{4\lambda k_B T}} \qquad (30)$$

The electronic coupling J is given by a precise quantum mechanics calculation on the overlap integral. In an artificial electron transfer system, some structures are highly ordered and people strive to find certain empirical laws for its value as a function of some simple parameters (most commonly, e.g. the distance between the donor and acceptor, or more complicated, involving bridges). The most well-known empirical form of the electron coupling related to distance is Dutton's ruler, which predicts intra-molecular electron transfer rate:

$$J^2 = J_0^2 exp(-\beta R) \qquad (31)$$

P.L Dutton found a good empirical value for β, $1.4\,\text{Å}^{-1}$, which can be used to predict the rate of many protein electron transfers, including photosynthetic reaction centers.

Electronic coupling aside, the term $(4\pi\lambda kT)^{-1/2} exp-[(\lambda + \Delta G)^2/4\lambda k_B T]$ is often referred to as the Franck-Condon weighted density of states when the solvent reorganization energy originates from harmonic oscillations of the same frequency. If the solvent environment is treated as a thermal bath populated with various vibrational modes, a spin-boson model can be used[77].

One of the most important conclusions that came out from the Marcus model, and has been verified by experiments, is the Marcus inverted region. The Marcus theory predicts that the reaction rate can actually slow down if one keeps

increasing the driving force ($-\Delta G^{o}$), thus entering a so-called inverted region. The inverted region is caused by the reappearance of an activation energy when the negative free energy is larger than the reorganization energy (figure 22). In his famous review[76], Marcus used the inverted region to explain the charge recombination that occurs in the primary stage of electron transfer in the reaction center protein.

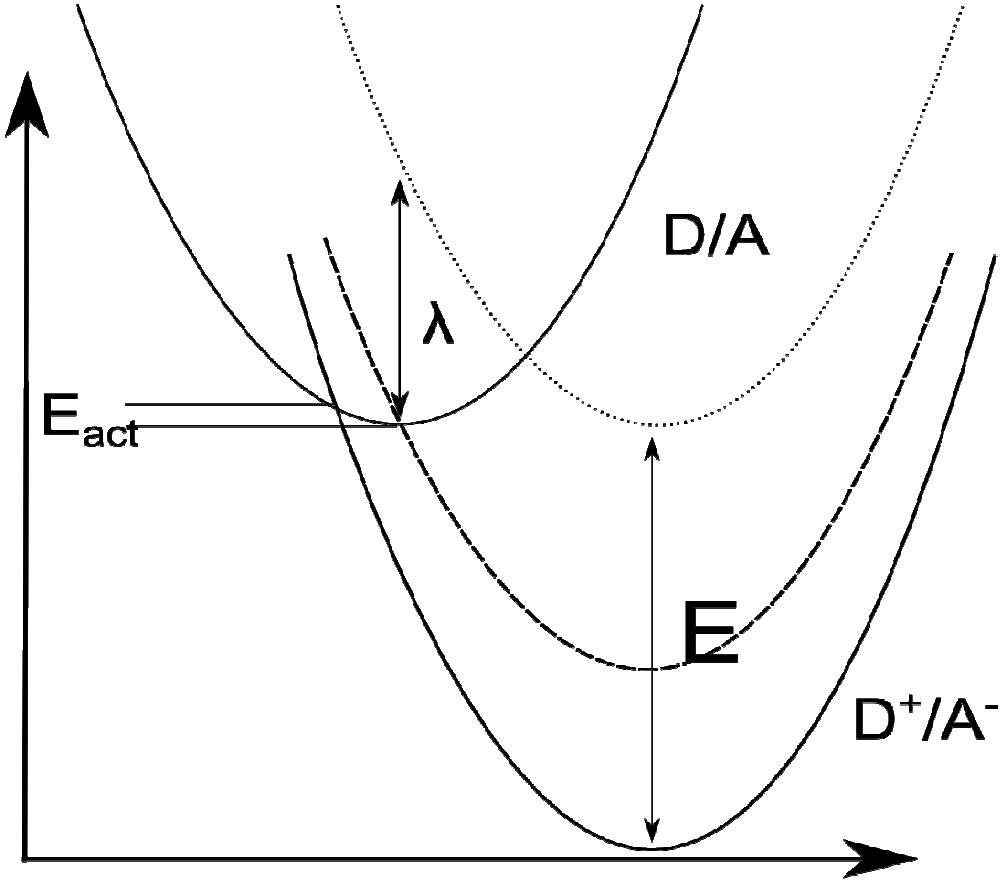

Figure 22: The Marcus inverted region. When the free energy level of the product state D^{+}/A^{-} decreases, the activation barrier E_{act} first decreases, until it decreases to zero. After passing the minimum point of the reactant parabola, the reaction enters the Marcus inverted region and the activation barrier E_{act} starts to increase again.

In Marcus's original treatment, the “solvents” have no dynamic detail, and are purely modeled using thermodynamics. In some cases, the assumption of a thermal equilibrium population of reaction states that are unperturbed by the reaction itself does not seem to be satisfied. Hans Kramers first studied the problem of finding the reaction rate at which a Brownian particle escapes from a potential well over a potential barrier[78]. Sumi et al. extended the application to realistic electron transfer models, taking into account the diffusive nature of the dielectric relaxation of the solvent[79]. More specifically, the “diffusive” motion refers to the solvent nuclear motion along a polarization coordinate. An approximation can frequently be adopted in which vibrational relaxation is treated as “fast” relative to the other molecular motions. Typically the vibrational relaxation occurs in the picosecond time scale. Compared with this time period, the molecular relaxation time for reorientation τ_L of the orientational fluctuation of the solvent molecules is longer than tens of picoseconds[80-82]. Generally, the reorganization energy is then expressed in terms of the orientational polarization contribution (slow) and the intra-molecular vibration (fast). Therefore, the reorganization energy is split into

$$\lambda = \lambda_f + \lambda_s \qquad (32)$$

In a quadratic approximation for both the polarization components and the vibrational components, it is possible to single out a scalar variable X that is proportional to a certain component of the polarization vector which passes through the two minimum energy points associated with reactants and products in the polarization coordinate space. The intra-molecular coordinates involved in the

electron transfer are represented by a coordinate q. When the reactant can be represented by one potential energy surface in (X,q), and the product by another enregy surface. When the electron coupling between those two is small, the transition state lies at the intersection of two surfaces. It is supposed that while the distribution of X on the reactant's surface may not be an equilibrium one, that of q is. Therefore, a rate constant k(X) can be defined, which involves at each X a suitable averaging over the population in the q coordinate. The resulting reaction-diffusion equation involves the coordinate X diffusing via a Brownian motion under the influence of a potential V(X), while the reaction occurs at each X with a rate constant k(X) during the diffusion. Mathematically, this is written as:

$$V_{reactant} = \frac{1}{2}(q^2 + x^2)$$

$$V_{product} = \frac{1}{2}(q - q_{prodcut})^2 + \frac{1}{2}(x - x_{product})^2 + \Delta G$$

$$\lambda_s = \frac{1}{2}x^2$$

$$\lambda_f = \frac{1}{2}q^2$$

At room temperature, the population density evolution of the reactant $\rho(x,t)$ is described by the Smoluchowski diffusion equation:

$$\frac{\partial \rho(x,t)}{\partial t} = D_p(t)\frac{\partial}{\partial x}\left[k_B T \frac{\partial}{\partial x} + x\right]\rho(x,t) - K(x)\rho(x,t) \qquad (33)$$

$$K(x) = \frac{J}{\eta^2}\sqrt{\frac{\pi}{\lambda_f k_B T}}exp\left[-\frac{(\Delta G + \lambda - 2x\sqrt{\lambda_s})^2}{4\lambda_f k_B T}\right] \qquad (34)$$

The diffusion coefficient, $D_p(t)$, can be obtained from the dielectric relaxation function of the solvent, $C_p(t)$, where:

$$D_p(t) = -C_p(t) \cdot \frac{dC_p(t)}{dt} \qquad (35)$$

The dielectric relaxation function of the solvent typically can be derived from certain experimental measurements. For example, in the study of primary electron transfer in the reaction center, the absorption change of two tryptophan residues near to the special dimer (P) can be used as a probe for the dielectric relaxation during P* decay[83, 84]. The underlying mechanism for the tryptophan absorption change could be associated with an internal Stark electric field from P* that aaffects the tryptophan dipoles. The absorption change of the tryptophans reflects the decay of the internal field strength. In most circumstances, it is impossible to solve the entire equation array analytically, and a numerical solution is convenient with the assumption of initial conditions. If an initial condition is a normal distribution of the prepared reactant state over the fast reaction coordinate upon light excitation, the expression would be $\rho(x,0) = exp[-(x + x_0)^2]$. The final observed time dependent population of the reactant concentration would then be:

$$P(t) = \int \rho(x,t)dt \qquad (36)$$

The above expressions represent the classical form of the Marcus theory. At higher temperatures, such as room temperature, these expressions hold true. At lower temperatures, when the thermal activation is not enough to overcome the activation barrier, there is still a possibility that the system can cross the barrier and result in a reaction through quantum tunneling. As a result, corrections need to be made for the quantum limit at low temperatures, and the Hopfield formula

describes this situation[85]. A major revision of the classical electron transfer formula changed the room temperature Boltzmann statistics into Fermi-Dirac statistics for low temperature limit. At the low temperature limit, the harmonic oscillator energy approaches the quantum limit, leaving only the zero-point energy, and therefore the quantum tunneling effect dominates. In the above formula, equation (34), the terms $2\lambda_f k_B T$ and $2\lambda_s k_B T$ are replaced by $\lambda_f \eta\omega coth(\eta\omega/2k_B T)$ and $\lambda_s \eta\omega coth(\eta\omega/2k_B T)$ respectively.

7 Molecular modeling techniques for studying the protein dynamics in reaction center protein

In parallel to the experimental work performed in the molecular biology wet lab and the laser lab, computational techniques have been employed to further the understanding of the reaction center system. The computational technique that can be utilized to study the reaction center system is various. Here, we are more interested in realistic, physical models of well-defined assignments rather than numerical models. More specifically, molecular dynamics simulations and quantum chemistry calculation protocols are developed and applied to study the protein dynamics and spectroscopic properties of the cofactors. In a study of the pH dependent electrostatics within the reaction center protein, the numerical Poisson-Boltzmann approach and the Monte Carlo simulation method were used.

The molecular dynamics simulation utilized in this thesis is more valuable for practical engineering purposes than for those of general mechanistic studies. The force field parameter and modeling are required to be more rigorous, while

the simulation data analyses in this work are limited to direct comparisons with the experimental data or observations.

The principle of performing a molecular dynamics simulation is simple, which is based on Newton's second law ($F = ma$):

$$\frac{d^2x_i}{dt^2} = \frac{F_{x_i}}{m_i} \qquad (37)$$

The above equation describes the motion of a particle of mass m_i along one coordinate (x_i), where F_{x_i} is the force on the particle in that particular direction. Successive configurations of the system, composed of many atoms or molecules, are generated by integrating equation (37). Numerically, there are many approaches to integrate equation (37), and all those qualified algorithms mush satisfy two conditions for robust application[86]: 1) conserving energy and momentum. 2) being time-reversible in principle. The most popular integration algorithm is the Verlet algorithm[87]. The Verlet algorithm uses the positions and accelerations at time t, along with the positions from the previous step, r(t-δt), to calculate the new position at t+δt, r+δr. The following relationship can be written down via Taylor's expansion:

$$r(t + \delta t) = r(t) + \delta t v(t) + \frac{1}{2}\delta t^2 a(t) + \Lambda \qquad (38)$$

$$r(t - \delta t) = r(t) - \delta t v(t) + \frac{1}{2}\delta t^2 a(t) - \Lambda \qquad (39)$$

adding them together yields:

$$r(t + \delta t) = 2r(t) - r(t - \delta t) + \delta t^2 a(t) \qquad (40)$$

$$v(t) = [r(t + \delta t) - r(t - \delta t)]/2\ \delta t \qquad (41)$$

Following the basic algorithm are the physical parameters that describe the interactions (the forces). The forces can be easily calculated by taking a secondary derivative of the potentials, which poses the physical potential modeling of the system as of supreme importance[88]. The selection of a force field largely depends on the problem being studied and what kind of information needs to be acquired. Most current empirical force fields are not very good tools to describe chemical reactions involving bond breaking and electron transfer. A few recent force fields like ReaxFF[89] are useful, but are still in very early stage of development. Empirical force fields have their strength in describing the non-bonded interactions and configuration distributions in the long term, which are in contrast to quantum mechanics techniques. One might ask, so long as you are studying electronic excitation and electron transfer, why not quantum mechanics? The reason is simple: it is expensive. The reaction center protein is a medium size protein wrapping 10 cofactors in its main body. Simply to calculate the coupled excited state transition of all 6 BChls/BPhes on a full quantum-mechanics level is a formidable job to do (particularly, recent work shows that this is a system that must be broken with brutal force at very expensive computational cost to get a qualitatively correct absorption spectrum[90]), let alone modeling the electron transfer coupled to protein dynamics. Therefore, it is not realistic to guide the experiments with such high level, expensive, theoretical calculations for the electron transfer by engineering trial and error. However, it is possible to evaluate the structure and stability of a reaction center mutant in the ground state (relative to the wild type) with empirical force fields, which could also be applicable to

engineering of this protein. Once a reliable trajectory is obtained, it can be used for semi-classical quantum chemistry calculations and can further predict some spectroscopic properties in a qualitative manner. The force field used in this thesis is in accordance with Ceccarelli et al.'s work[91]. For the protein and water the AMBER force field (AMBER99)[92] and the TIP3P model[93] were used, respectively. The force field parameter sets for the cofactors (including BChl-*a*, BPhe-*a*, and Ubiquinone-10) and the detergent molecule LDAO were derived in the same work, and were adopted without further changes for the ground state simulation. Preliminary studies of the charge separated states focused on parameterizations on the partial charges assigned to the the special dimer (P^+) and the BPhe anion (H_A^-) and their applications to molecular dynamics simulation. The parameterizations for the radical states of the cofactors were realized by performing un-restricted shell density functional theory (DFT) calculations with a relatively large basis set. The B3LYP hybrid exchange-correlation functional is used, and a Pople-style 6-31G(d) basis set is used for calculating the special dimer as a whole. The phytyl tail in both BChl-*a*s has been replaced by a methyl group for computational efficiency. The partial charge on each atom is acquired by doing a restrained electrostatic potential (RESP) fit[94] to the electrostatic potential (ESP) from the DFT calculation (see Appendix A). A similar protocol was used for the BPhe anion charge fitting, except that a diffuse function was appended to the basis set (6-31+G(d,p)) to account for the anion feature. The force constants for the charge separated state stayed the same as

those in ground state parameter set. Modeling for the simulation system was divided into three steps, described in detail below.

First, the reaction center structure was modified and its topological description was prepared. The reaction center crystal structure used for this modeling study is taken from Koepke et al[95], at 1.87 Å resolution, PDB id 2J8C. The non-heme iron was treated as Fe^{2+} and assigned with two positive partial charges; the Van der Waals parameter was taken from AMBER99. Protonation states of the ionizable amino acids are assumed to be at pH=7, except for those known to bind as a ligand or form certain hydrogen bonds (such as L153H, L173H, M202H, L183H, and L104E). Five missing amino acids in the M branch terminal was added by Swiss PDBviewer[96] and modeled as random coil conformation. The other missing heavy atoms, and all of the hydrogens, were rebuilt by the *tLeap* module in AmberTool[97]. When the naked protein system was modeled up, the system was put into relaxation using the conjugate gradient method for 500 steps to remove clashes. This step, and the subsequent simulation steps were performed in NAMD 2.7[98].

In the second modeling step, the naked reaction protein was wrapped in its "clothes", LDAO detergent micelles, in a stepwise manner, to achieve an equilibrium of the final system within a minimal amount of computing cpu hours. More specifically, this was carried out by first wrapping the system with 20-30 detergent molecules 3-4 Å away from the reaction center structure, followed by a MD equilibrium in 500 ps at a relatively high temperature (400 K) allowing the newly appended detergent layer to get close to the reaction center quickly (fast

annealing). The wrapping and equilibration step were repeated for several rounds until the total number of the detergent molecules reached 110, in accordance with previous literature reports(40-370 at pH 6-10, 150 c.a. at pH 8[99]).

The third modeling step involves solvating the entire reaction center protein and detergent micelle system in a water box, almost 60 Å$\times$60 Å $\times$60 Å in size, plus 6 sodium and 7 chloride ions both to neutralize the system and to reach a molar concentration of 0.13 M in accordance with experiments (0.15 M, no need to be accurate, experimental additive can fluctuate from 0-3 M and the reaction centers are amazingly robust in spectroscopy without salting out). This step is carried out by VMD software[100]. The whole system incorporates 90,191 atoms. Standard molecular dynamics simulation protocol is next applied to this system, and the simulation parameters are listed in Table 1.

Table 1: Parameter set for performing the molecular dynamics simulation during the equilibration stage

Equilibrium Simulation Parameters	Value
Integrator step size	1 fs
Trajectory recording frequency	Every 1000 steps (1 ps)
Switching distance for short-range force cut-off	10 Å
Short-range force cut-off	12 Å
Pair-list update range	14 Å
Multiple time step technique	1-2-4 scheme
Simulation ensemble	NPT
T-coupling	Langevin dynamics
T-coupling target temperature	300 K
Langevin damping coefficient	1 ps^{-1}
P-coupling	Langevin Piston
Particle-Mesh-Electrostatics	YES
Simulation Trajectory length	30 ns

Figure (23) and (24) show the results of some evaluation criteria for system equilibrium. Following Ceccarelli et al's work[101], if we define the self-diffusion coefficient of the LDAO molecule by using the mean squared displacement of its head group nitrogen atom, then:

$$< r^2(t) >= \frac{1}{N}\sum_{i=1}^{N}\left|r_i(t) - r_i(0)\right|^2 \qquad (42)$$

According to the Einstein relationship, the diffusion coefficient is given by:

$$D = lim_{t\to\infty}\frac{< r^2(t) >}{6t} \qquad (43)$$

In practice, the diffusion of the LDAO micelle appears to be separated into two linear regions. The first stage is faster, lasts for around 10 ns, with a diffusion constant of $2.4 \times 10^{-11} m^2/s$, whereas the second stage (the next 20 ns) is getting slower, decelerating to $0.5 \times 10^{-11} m^2/s$. Considering that this simulation work is more than 7 times longer than Ceccarelli et al.'s work, it is able to capture a more equilibrated phase of the micelle. In fact, if the first 4 ns trajectory is taken out for predicting the diffusion coefficient, it gives nearly the same value as reported ($7 \times 10^{-11} m^2/s$ *vs.* $5.3 \times 10^{-11} m^2/s$), yet this value incorporates a significant non-diffusion contribution (inertial regime) and can cause quite a large error. The final diffusion coefficient approaches the diffusion coefficient of the protein itself, which most likely indicates that most of the LDAO molecules are docked to the protein as an integral part (Table 2).

Table 2: Self-Diffusion constant, D[m^2/s] calculated from MD simulations for LDAO detergent micelle

	0-4 ns (value reported in Ref. [101])	2-11 ns	11-30 ns
LDAO diffusion coefficient	$7 \times 10^{-11} m^2/s$ ($5.3 \times 10^{-11} m^2/s$)	$2.4 \times 10^{-11} m^2/s$	$0.5 \times 10^{-11} m^2/s$
protein diffusion coefficient	($0.4 \times 10^{-11} m^2/s$)		

There are some other order parameters used to characterize the equilibrium of the LDAO micelle, which are compared with those values in Ceccarelli's publication (figures 23 and 24), and all of them show a sign of convergence.

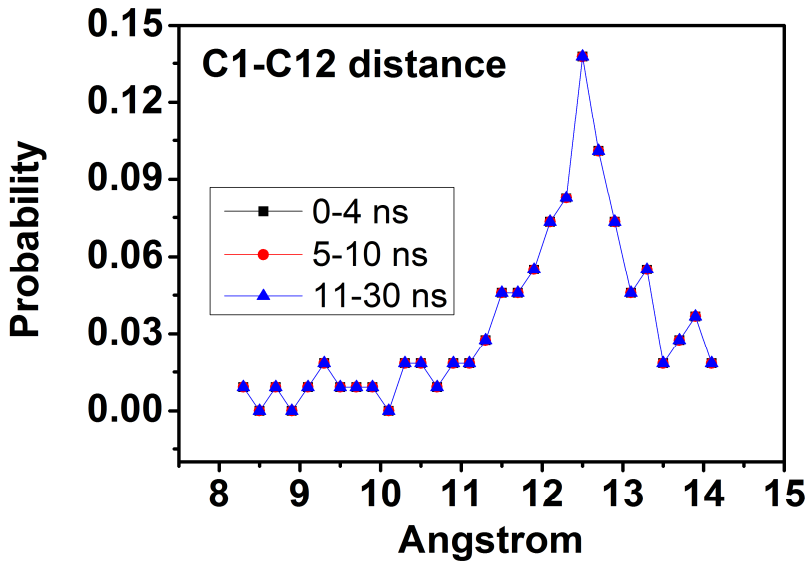

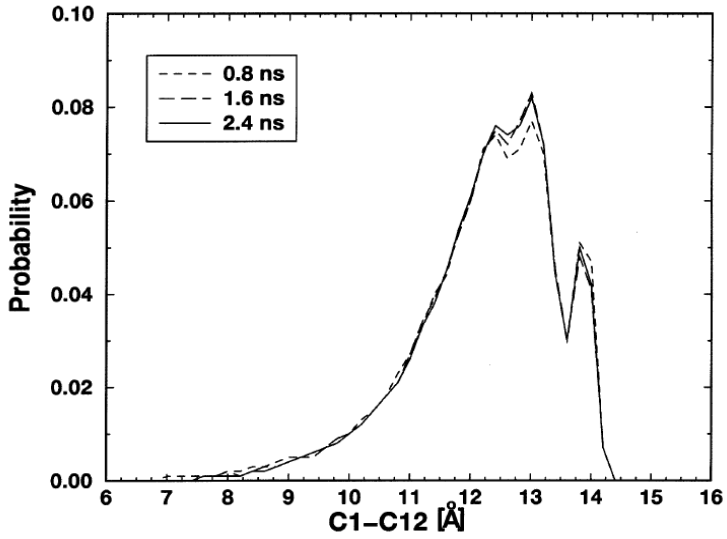

Figure 23: Normalized probability distribution of the C1-C12 distance. It characterizes the configuration of the LDAO molecules according to their tails' extension, which is related to the steric constraint on them. The top graph is the result of current work, and the bottom graph shows the results from Ceccarelli et al's work[101].

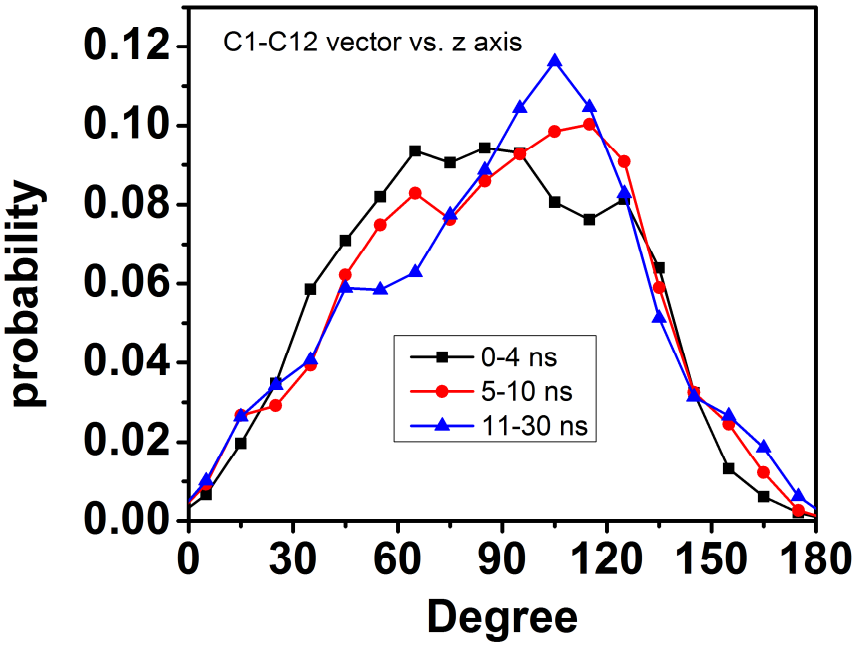

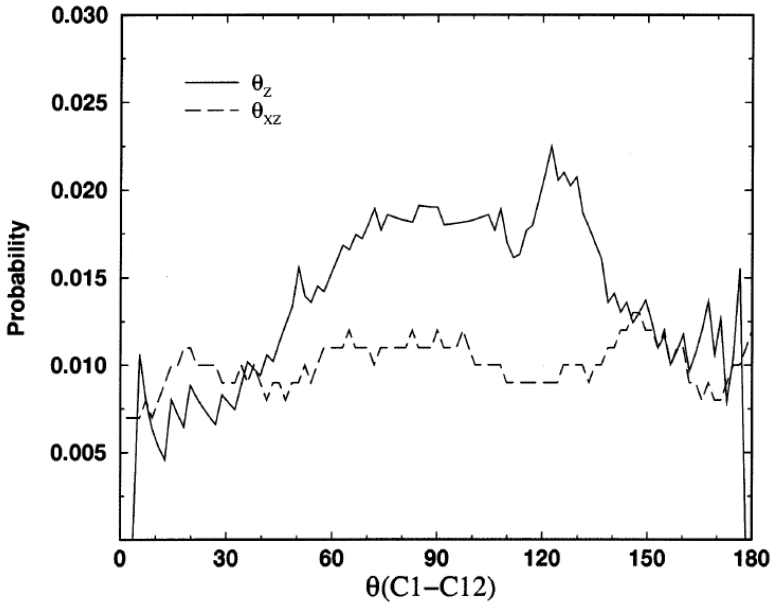

Figure 24: Normalized probability distribution of the C1-C12 orientation relative to the Z axis (θ_z).The orientation of the C1-C12 vector with respect to the Z axis (parallel to the C2 axis), allows the characterization of the LDAO orientation around the protein complex. Upper panel is the result from this simulation, lower panel is the result from Ceccarelli et al's work[101]. In their work, a relative angle between C1-C12 vector and the Z plane was also presented.

After the equilibrium, the final structure is shown as below (figure 25) in cartoon representation

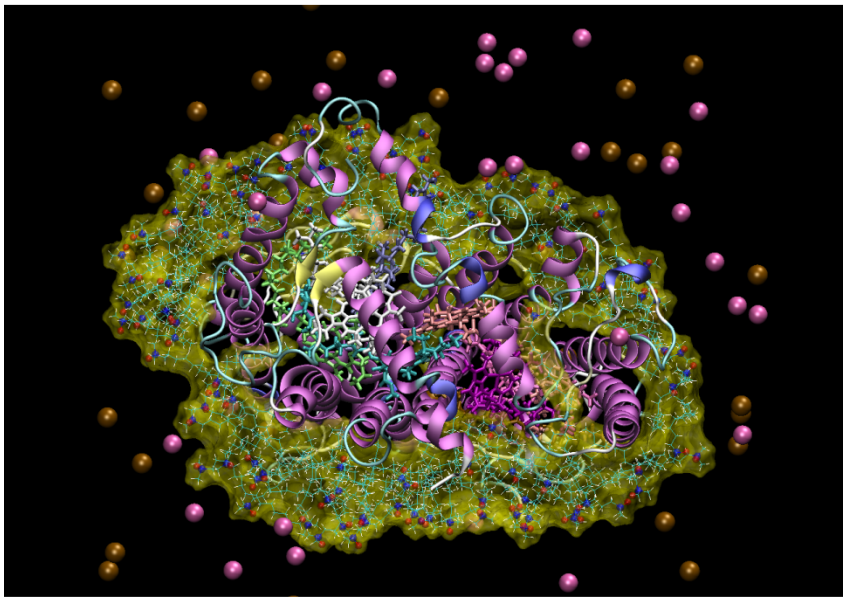

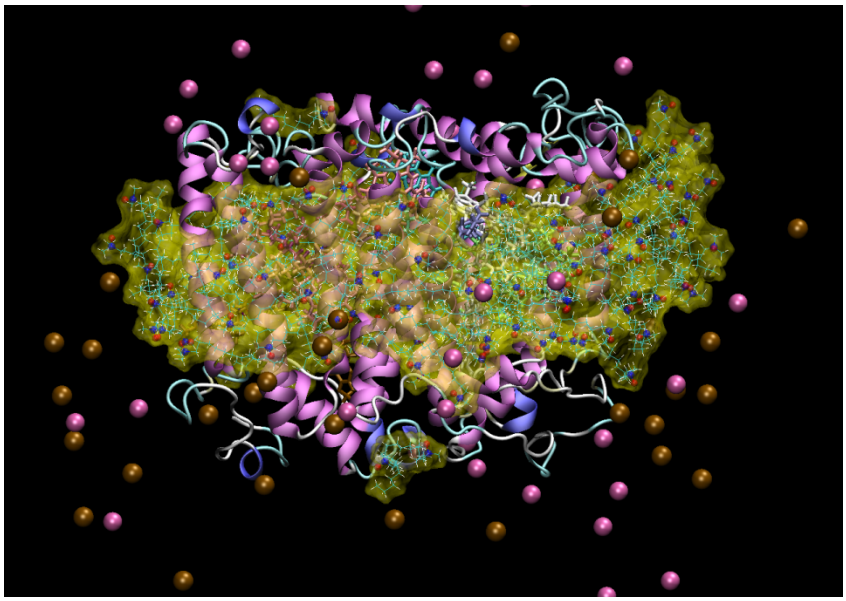

Figure 25: Equilibrated structure in MD simulation. Upper panel, top view (from the periplasmic side); lower panel, side view. The reaction center protein is rendered in cartoon representation, and the cofactors are shown in sticks. The LDAO molecules are shown as wires (H,C,N,O atoms are shown, the last two atom types are rendered in blue and red color respectively). The polar groups (N and O atoms) of LDAO molecules are facing outward to the water solvent. The ions in the solvent are shown as spheres (pink for Cl^-, and brown for Na^+).

Mutant stability is tested by mutating the residue of the target amino acid *in silico* and evaluating their relative stability from molecular dynamics simulation results. The simulation protocol for the mutants are the same as those performed for wild type. Criteria used to evaluate the stability is the root mean square deviation (RMSD, a numerical measure of the difference between two structures, definition see Appendix B) of the molecule relative to the wild type (the atom set used for the comparison is defined as the atoms that are within 7 angstroms distance from the mutation site). Figure 26 presents such a result. The stability of a mutant is normally estimated by its activation free energy barrier between its folded

structure and its transition state structure connecting to the unfolded structure ensemble. Simplified criteria test whether a mutant could exist or not by using conventional molecular dynamics simulation and its local RMSD. Rearrangement of the local structure near the mutation site leads to an increase of RMSD. If this is a relative minor change and does not show a linear growth with time in the long run (otherwise it indicates that there is essentially a diffusion inside the structure), then the structure might still be intact. In this study, it appears that lysine (K) and asparagine (R) might not be a good amino acid replacement for this mutation site, whereas the other mutants might still preserve most of the native structure. The mutant M210YR was prepared with molecular biology mutagenesis technique as previously described. Failure to isolate the reaction center structure as other M210 mutants, suggests that the YR substitution could be unstable, which to some extent supports the validity of the results from molecular dynamics simulations. One useful result that can be produced by the all-atom MD simulation is the 3D electrostatic potential profile. A quick evaluation of electrostatic interaction in the reaction center protein is often performed with a static structure, usually a crystal structure, using different dielectric constants for the protein and solvents. By assigning each atom a certain partial charge, the spatial distribution of the electrostatic potential induced by the charge atmosphere can be calculated by numerically solving the Poisson-Boltzmann equation.

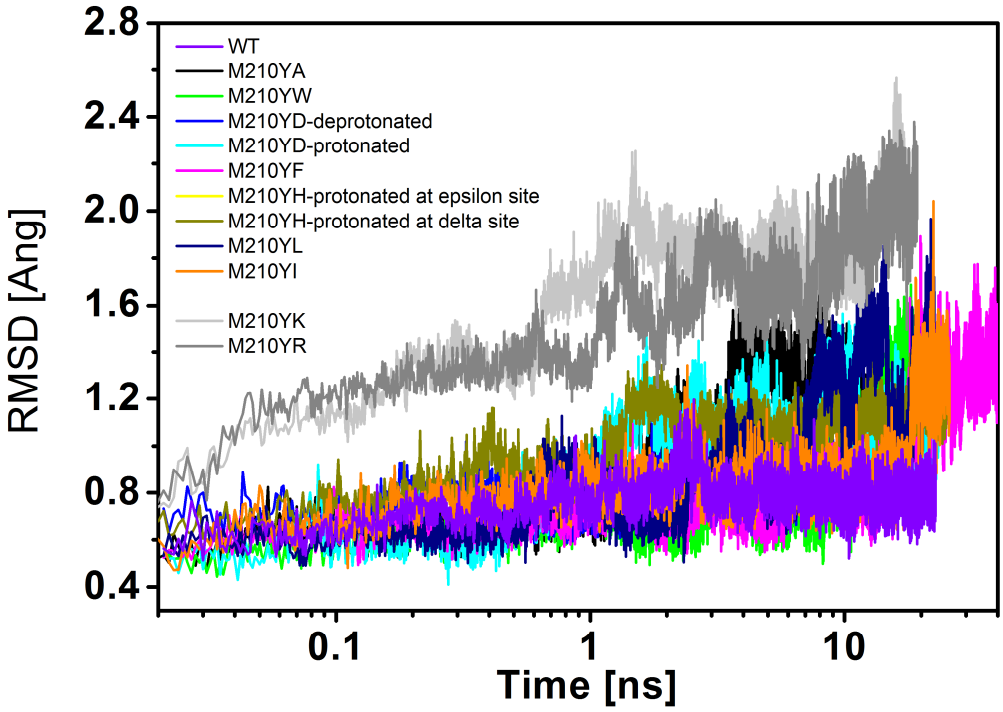

Figure 26: The structural difference between the simulated structures and the initial structures (including crystal structures and optimized mutated structures) in the wild type reaction center and its M210 mutants evolves as a function of time. The unit for the root mean squared deviation is in angstroms.

In figure 27, it is shown that the electrostatic potential generated by the smooth particle-mesh Ewald method in an all-atom level simulation (averaged on the last 1 ns trajectory frame of the MD simulation) is generally very similar to the electrostatic potential obtained with the dielectric continuum method (uses one single crystal structure, $\varepsilon = 4.0$)[102]. Seeing from here, it appears that the reaction center has different dielectric properties in its two branches as reported before[102, 103].

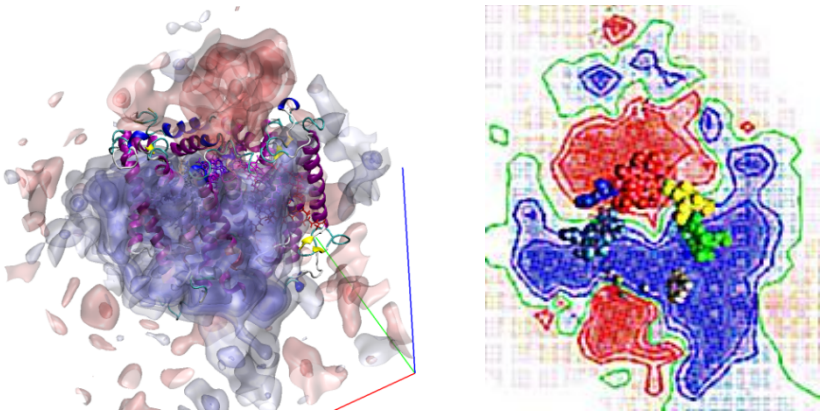

Figure 27: The 3-D electrostatic potential profile of the ground state wild type reaction center obtained from molecular dynamics simulation (PME electrostatics), in iso-value surface representation (left panel). Red for positive, blue for negative. The most exterior positive profile has an iso-value of 0.39 eV, while the exterior negative profile has an iso-value of -0.52 eV. Right hand side is the electrostatic calculation using continuum electrostatics (Delphi) from Gunner et al's work. Note that the L,M branch in those two graphs are flipped.

Although the all-atom MD simulations often provide more details about dynamics, they normally do not allow for a constant pH simulation[104-106]. They often require quantum mechanics descriptions to account for the proton transfer process. Chapter 3 of this thesis investigates the pH dependent electron transfer in the wild type reaction center and its M210YD mutant. Some rough estimates of certain side chain protonation states at given pH conditions are necessary to model the electron transfer pathway in the reaction center after light excitation. In such circumstance, the Multi-Conformation Continuum Electrostatics (MCCE) approach[107] has been used to estimate the pKa value of the ionizable amino acid side chains. This approach is an improved version of the single-structure dielectric continuum method, which utilizes the Monte Carlo annealing method to sample

the side chain torsion angles and generate different side chain conformers in order to introduce conformational flexibility (see Figure 28).

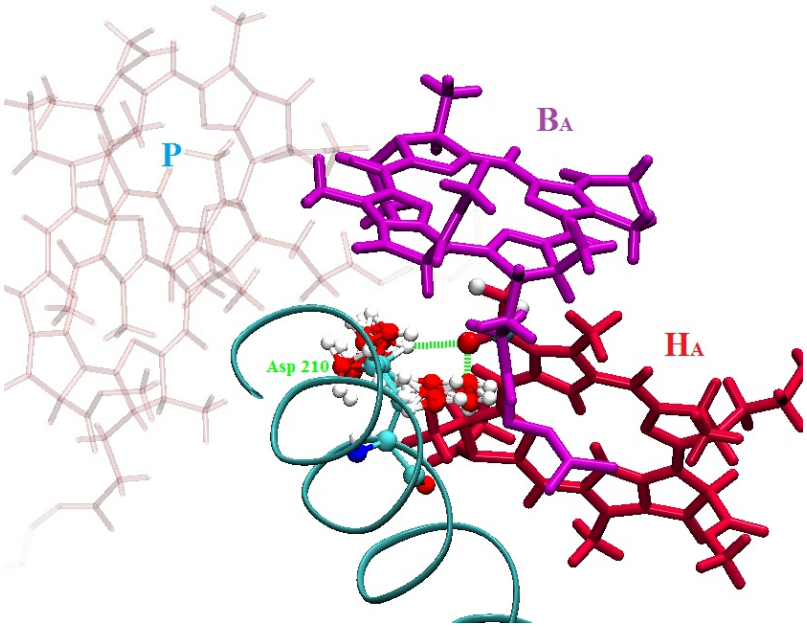

Figure 28: Various conformers and protonation states of Asp 210 side chain sampled by Monte Carlo approach in MCCE program.

After performing the conformational sampling, the probability of the protein to reside in a protonation state, represented by vector **X,** requires appropriate Boltzmann average over all possible microstates. In thermodynamic equilibrium, the vector incorporates 2^N protonation state elements, where N is the number of titration sites. The relationship can be expressed as:

$$\Omega_{\mu,eq} = \frac{e^{-\beta G_\mu} \cdot e^{\beta m_{X\mu} H^+}}{Z}$$

$$Z = \sum_p^{2^M} e^{-\beta G_\mu \cdot m_{X\mu} H^+}$$

Where m is the number of protons bound to the molecule, and μ_{H^+} the chemical potential of the proton. G_μ is the electrostatic interaction energy between ionizable sites. The MCCE program also outputs a pH titration curve of each ionizable amino acid side chain, which is given by:

$$\Theta_j \;\leq< p_j \;>= \sum_{\mu}^{M} p_{\mu,j}\,\Omega_{\mu,eq} \qquad (44)$$

where $p_{\mu,j}$ is the number of protons bound on site j at chemical potential μ.

CHAPTER 2

Comparing the temperature dependence of photosynthetic electron transfer in *Chloroflexus aurantiacus* and *Rhodobactor sphaeroides* reaction centers

Abstract

The process of electron transfer from the special pair, P, to the primary electron donor, H_A, in quinone-depleted reaction centers (RCs) of *Chloroflexus (Cf.) aurantiacu*s has been investigated over the temperature range from 10 to 295 K using time-resolved pump-probe spectroscopic techniques. The kinetics of the electron transfer reaction, $P^* \rightarrow P^+H_A^-$, was found to be non-exponential and the degree of non-exponentiality increased strongly as temperature decreased. The temperature-dependent behavior of electron transfer in *Cf. aurantiacu*s RCs was compared with that of the purple bacterium *Rhodobacter (Rb.) sphaeroides*. Distinct transitions were found in the temperature dependent kinetics of both *Cf. aurantiacus* and *Rb. sphaeroides* RCs, at around 220 K and 160 K, respectively. Structural differences between these two RCs, which may be associated with those differences, are discussed. It is suggested that weaker protein-cofactor hydrogen bonding, stronger electrostatic interactions at the protein surface and larger solvent interactions likely contribute to a higher transition temperature in *Cf. aurantiacus* RCs temperature dependent kinetics compared with that of *Rb. sphaeroides* RCs. The reaction-diffusion model provides an accurate description for the room temperature electron transfer kinetics in *Cf. aurantiacus* RCs with no free parameters, using coupling and reorganization energy values previously

determined for *Rb. sphaeroides,* along with an experimental measure of protein conformational diffusion dynamics and an experimental literature value of the free energy gap between P* and $P^{+}H_{A}^{-}$.

Introduction

Protein folding studies have demonstrated the importance of the protein conformational energy landscape in determining the pathway and products of the protein folding process[108, 109]. Given this, it is perhaps not surprising that conformational dynamics of fully-folded protein systems play a critical role in native protein function. While this concept is not new, the last decade has seen a dramatic increase in the number and sophistication of theoretical and experimental studies in this area. This work includes increasingly accurate calculations from simulation studies[110-113], the observation of conformational fluctuation associated with function at the single molecule level[114-116] and a variety of studies of photoinitiated chemical processes in proteins[117-120], such as those that employ ultrafast x-ray diffraction techniques[121-123].

One of the most important realizations that has emerged from this work is that dynamic heterogeneity is not a liability to protein systems, but is likely pivotal in making them as functionally robust as they are. The ability to explore local conformational space means that moderate changes in the environment, or even in protein sequence, can be accommodated by maintaining a level of conformational flexibility that allows the protein to compensate appropriately. An important aspect of this adaptability is that proteins undergo conformational

changes over a very broad range of time scales, from femtoseconds to hours, making them an extremely versatile solvent for performing chemistry and ensuring that movement, and the associated changes in the energy landscape of the system, occurs on essentially any time scale relevant to biology.

Different experimental approaches have been used to look at reactions on various time scales. However, in the sub-nanosecond regime, where essentially all electron transfer reactions take place, spectroscopic measurements of photoinduced charge separation and associated protein movement dominate. In this regard, the photosynthetic reaction center (RC) of purple non-sulfur photosynthetic bacteria is perhaps the best characterized system. This protein-pigment complex uses light energy to power a series of electron transfer reactions that ultimately yield a charge-separated state that drives trans-membrane proton translocation. In recent years, it has become evident that electron transfer in this system is directly dependent on protein dynamics. In other words, the exploration of protein conformational space is rate limiting in photosynthetic electron transfer, and thus it is this conformational diffusion that actually determines charge separation kinetics. This type of electron transfer kinetics is embodied in the concept of reaction diffusion in polymer systems and, as a model for non-ergodic reactions, does an excellent job of describing the electron transfer kinetics of bacterial RCs over a broad range of temperatures and reaction free energies.

One of the great advantages of studying bacterial photosynthetic reaction centers is their robust nature; isolated reaction centers are stable for long periods at room temperature and can undergo many cycles of photoexcitation. In

addition, their structure is easily altered through genetic modification, and they are very tolerant of mutational change in terms of protein folding and cofactor assembly. By taking advantage of these characteristics, a great deal has been learned about the role of thermodynamics in reaction center function and in the mechanistic details of specific cofactor function in electron transfer. However, exploring the role of protein conformational dynamics is more difficult. It is hard to imagine how one would systematically alter the distribution and interconversion of different reaction center conformations via mutagenesis. Fortunately, Nature has provided examples of proteins in which the conformational flexibility been altered in more or less predictable ways. Thermophilic proteins are stable at high temperature in part because they limit access to protein conformations that could lead to denaturation or loss of function. There are a number of thermophillic photosynthetic bacterial systems available, and analysis of these reaction centers, in comparison to mesophilic reaction centers, may provide an avenue for probing the effects of systematic changes in conformational diffusion on electron transfer. In particular, one might expect that both the rate of conformational interconversion and its temperature dependence should be altered in thermophilic vs. mesophilic proteins. Here, this concept is explored through a detailed comparison of the electron transfer kinetics of the RCs of *Rhodobacter (Rb.) sphaeroides*, a mesophilic, purple nonsulfur bacterium and *Chloroflexus (Cf.) aurantiacus*, a thermophilic, filamentous anoxygenic phototroph (FAP)[10, 124].

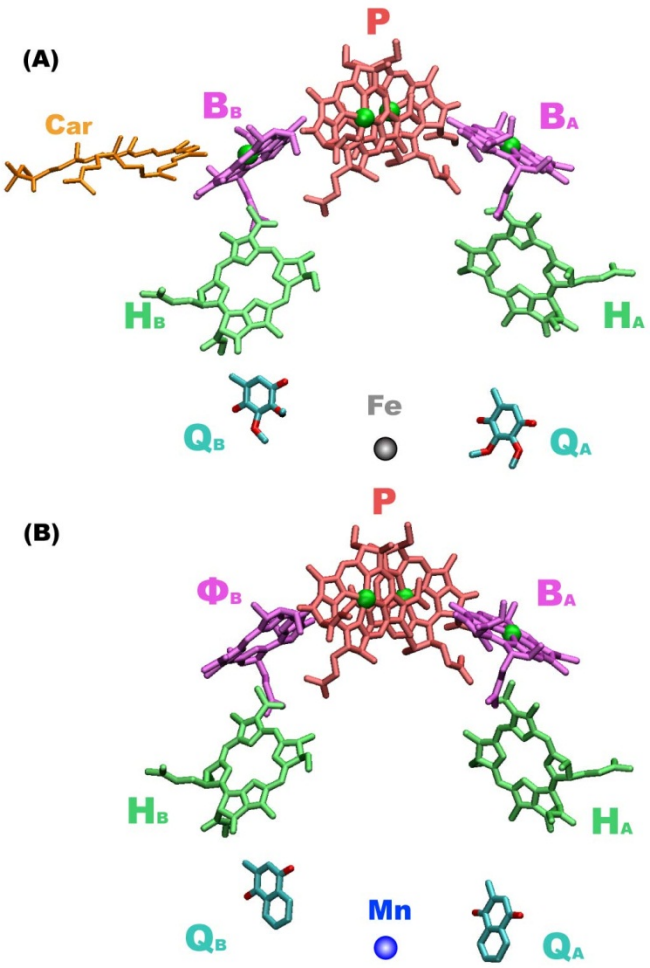

Figure 1. Cofactor arrangement in two bacterial reaction centers. From top to bottom, red for the bacteriochlorophyll dimer (**P**), magenta for bacteriochlorophyll monomer (**B**, or for B branch in *Cf. chloroflexus* RC, **Φ** is used), green for bacteriopheophytin (**H**), cyan for quinones (**Q**), and metals between two quinones (**Fe** for *Rb. sphaeroides*, **Mn** for *Cf. chloroflexus*) at the bottom. Carotenoid (**Car**) in *Rb. sphaeroides* RC is in orange color. A) *Rb. sphaeroides* RC, B) *Cf. chloroflexus* RC. The cofactor arrangement for the *Rb. sphaeroides* RC is obtained from ref [125](PDB id: 1PRC), the cofactor arrangement for *Cf. chloroflexus* RC is a 'schematic' illustration modified from the *Rb. sphaeroides* RC. Graphs were prepared by VMD software.

The structure of RCs from *Rb. sphaeroides* is well known in multiple forms and includes 10 cofactors: 4 bacteriochlorophyll (BChl) molecules, 2 bacteriopheophytin (BPheo) molecules, 2 ubiquinone molecules, a carotenoid

molecule and a non-heme iron atom. These cofactors are bound to two symmetrically-related protein subunits, L and M, and form two symmetrically-arranged electron transfer chains (referred to as A and B, Figure 1A). A third protein subunit, H, is located on the cytoplasmic membrane side of the complex. In isolated wild type RCs, only the cofactors in the A-branch appear to be actively involved in the primary electron transfer reactions and each of the reaction steps has been well-characterized spectroscopically[25]. The initial charge separation occurs from the excited state of the two closely-coupled BChls P (P*) to a BChl monomer (B_A), forming the state $P^+B_A^-$ in 3 ps. The electron is then transferred from B_A^- to the BPheo (H_A), and finally to the quinone (Q_A) with time constants of 0.9 and 200 ps, respectively.

The structure of the RC from *Cf. aurantiacus* has not yet been determined, but past studies have suggested that its form and function is similar to that of *Rb. sphaeroides*[126], although the two organisms are phylogenetically quite separate[127]. A schematic model of the cofactor composition of the *Cf. aurantiacus* RC, based on the structure of the *Rb. sphaeroides* RC, is shown in Figure 1B. While the *Cf. aurantiacus* RC contains L and M protein subunits that are the functional analogues of those found in *Rb. sphaeroides*, it lacks the H protein subunit[10]. Comparing cofactors between the two types of RCs reveals that the monomeric BChl in the B-branch of the *Rb. sphaeroides* RC is a BPheo molecule in the *Cf. aurantiacus* RC, the carotenoid near B_B is missing, and the *Cf. aurantiacus* RC utilizes menaquinone, instead of ubiquinone, as the secondary electron acceptor[10]. In addition, there are some key differences in amino acid residues between the L

and M protein subunits of *Cf. aurantiacus* and *Rb. sphaeroides* reaction centers that likely affect the cofactor properties[127].

In *Cf. aurantiacus* RCs, the ground state absorption band of P peaks at 865 nm, similar to that in *Rb. sphaeroides* RCs[10]. It red shifts to 887 nm at 77 K and remains at roughly the same position down to 4 K. The stimulated emission from P* has been studied in *Cf. aurantiacus* RCs in polyvinyl alcohol films as a function of temperature, and the time constant of the initial electron transfer ($P^* \rightarrow P^+H_A^-$) was found to be 7.0 ps at room temperature, becoming biexponential (3.0 ps and 32 ps) at 80 K[128]. The corresponding overall electron transfer rates in *Rb. sphaeroides* RCs are 3 ps and 1.5 ps at room temperature and 77K, respectively, when a single time constant is assumed[129, 130]; though more detailed studies make it clear that the reaction is really kinetically heterogeneous. For example, using two components to describe the kinetics results in components of roughly 2 and 10-ps with the 10 ps component having a 10-20 percent amplitude at room temperature[131]. In *Rb. sphaeroides*, the kinetic heterogeneity appears to decrease with decreasing temperature, so that at 10 K, the reaction is essentially single exponential. Kirmaier et al. have investigated $P^+Q_A^-$ formation kinetics and determined the time constant to be 365±19 ps in *Cf. aurantiacus*, which is slower than that found in *Rb. sphaeroides* RCs (~200 ps)[132]. Volk et al. analyzed the $P^+H_A^-$ charge recombination process and determined that the energy gap between the P* state and the $P^+H_A^-$ state in *Cf. aurantiacus* RCs is about 0.04 eV less than that in *Rb. sphaeroides* RCs[133]. Recent studies by Collins et al. on

reaction centers from *Roseiflexus castenholzii*, an organism closely related to *Cf. aurantiacus,* have produced generally similar results[134].

In this study, we measured the temperature dependent electron transfer kinetics of *Cf. aurantiacus* RCs in detail over a wide temperature range (10 K ~ 294 K). The results were compared with those of *Rb. sphaeroides* RCs, which contains the same cofactors in the electron transfer chain but a protein environment evolved for mesophilic rather than thermophilic function.

Materials and Methods

Sample Preparation. Q_A-containing RCs of *Cf. aurantiacus* were prepared using a protocol previously described[135]. To remove quinones, isolated RCs were loaded on a Q-sepharose HP 5 mL column and washed extensively with 1L of 0.2% Triton X-100 (reduced form) in 20 mM Tris-HCl buffer (pH 8.0) until the absorbance (260~960 nm) returned to its baseline value. This concentration of Triton X-100 is sufficient to remove quinones in more than 99% of the *Chloroflexus* RCs. The quinone-depleted RCs were then eluted in the same buffer plus 100 mM NaCl. The peak fractions contained RCs with A_{860} greater than 10 in a 1-cm cuvette. The resulting samples were diluted with 0.1% LDAO in Tris buffer (20mM, pH8.0) to a final OD of 0.6 at 860 nm in the 1.2 mm optical path-length measuring cell.

Spectroscopic measurements. Femtosecond transient absorption spectroscopy was carried out using a pump-probe setup described previously[83, 84]. Laser pulses were generated at a repetition rate of 1 kHz with 130 fs duration at 800 nm using

a regenerative amplifier system based on a Titanium:Sapphire laser (Millennia, Tsunami, Spitfire, Spectra-Physics Lasers). Part of the beam was used to pump an infrared optical paramagnetic amplifier (OPA-800, Spectra-Physics) to generate excitation pulses at 860 nm and the other part was focused on a sapphire plate to generate a white light continuum that was used as the probe light. Tryptophan kinetics were measured using excitation at 800 nm and 280 nm probe pulses obtained via second harmonic generation using 560 nm pulses from the OPA. After passing through the sample, the probe pulses were sent through a monochromator (SP150, Action Res. Corp.) and detected by a photodiode detector (Model 2032, New Focus Inc.). Time-resolved spectra were recorded by scanning the monochromator over the desired wavelength region at a fixed time delay

Kinetic data analysis. Both multiple exponential and stretched exponential (Kohlrausch-Williams-Watts function) fitting methods were employed to fit kinetic decay curves. The latter has been widely applied to characterize complex kinetic processes, especially for the analysis of time-dependent photonic spectra and dielectric responses. The time-dependent, stretched exponential function has two nonlinear parameters per component:

$$f(t) = e^{-\left(\frac{t}{\tau}\right)^{\beta}} = \int_0^{\infty} e^{-\frac{t}{\tau}} \rho(\tau) d\tau$$

Here, τ is the characteristic time constant in the relaxation distribution, and the index, β, is associated with the width of the distribution, or the variety of the relaxation processes. If β equals ~1, the decay process distribution approaches a

Dirac function and the decay recovers to a single exponential relaxation. When β decreases, the relaxation process distribution becomes broader and the average lifetime produced by such a distribution is

$$< \tau >= \beta\tau \cdot \Gamma(\beta)$$

where $\Gamma()$ is the gamma function. To extend its application to the simultaneous relaxation of multiple processes, the sum of several stretched-exponentials can be used:

$$f(t) = \sum_i A_i e^{-\left(\frac{t}{\tau_i}\right)^{\beta_i}}$$

Applying the Reaction Diffusion model to describe Cf. aurantiacus kinetics.

The kinetics of initial electron transfer in reaction centers of *Rb. sphaeroides* have previously been successfully modeled using a reaction diffusion formalism, as previously described in ref [83] and in the supporting information. For the calculations described here, the electronic coupling strength (J) was assumed to be the same in reaction centers from the two species, and the driving force and time-dependent diffusion term were determined from experimental data, as described below.

Results

Initial electron transfer processes and tryptophan absorption kinetics in *Cf. aurantiacus* RCs at room temperature

For the temperature-dependent studies described below, it was necessary to remove Q_A from the *Cf. aurantiacus* RCs. These two samples, the Q_A-containing and the Q_A-depleted RCs, were compared both spectrally and kinetically to ensure that there were no major changes in the initial reactions simply due to quinone removal. Both the early time kinetics and spectra were essentially identical, with the initial electron transfer reaction occurring in both cases with biexponential kinetics involving a roughly 3 ps and 10 ps component (Supplemental data, Figure S1a, S2). Similar kinetics is observed in the Q_Y region of the spectrum, monitoring the ground-state bleaching of H_A and the formation of H_A^- at 540 and 660 nm, respectively (Supplemental data, Figure S3a,b). This is consistent with previous measurements of quinone-containing RCs of *Cf. aurantiacus*[128, 136]. As expected, removing Q_A does not strongly affect either the spectra or the kinetics of initial electron transfer indicating that quinone binding/removal has only a minor influence on the environment of P, as has been seen previously in *Rb. sphaeroides* RCs[130, 137, 138]. In quinone-containing RCs from *Cf. aurantiacus*, the state $P^+H_A^-$ decays in about 300 ps at room temperature as the electron is transferred from H_A to Q_A, in agreement with previous results[132]. Upon removal of the quinone, as expected[133], the $P^+H_A^-$ lifetime lengthens, decaying on the nanosecond time scale (data not shown).

Previously, the transient absorbance signal from tryptophan has been used to monitor the general kinetics of protein motion in the vicinity of the electron transfer reaction in *Rb. sphaeroides* RCs[83]. A key issue in this work is to understand if the distribution of protein dynamics differs in the thermophillic *Cf.*

aurantiacus RC. The change of the tryptophan absorption signal was measured at 280 nm upon special pair excitation, as was done previously in *Rb. sphaeroides* RCs. The induced absorption signal near 280 nm in *Rb. sphaeroides* RCs appears to originate, at least in part, from tryptophans W156(L) and W185(M), which are symmetrically arranged about 7~9 angstroms from the magnesium centers of the BChls forming P. Alignment between *Rb. sphaeroides* and *Cf. aurantiacus* RC sequences shows that W196(L) and W174(M) in *Cf. aurantiacus* are analogous to W156(L) and W185(M) in *Rb. sphaeroides* RCs [127], which suggests that these two conserved tryptophans may also serve as probes in measuring the protein dynamics in *Cf. aurantiacus* RCs[83]. The tryptophan absorbance kinetic changes from Q_A^--depleted *Cf. aurantiacus* RCs are compared with those from Q_A^--depleted *Rb. sphaeroides* RCs over 350 ps in Figure 2. The protein relaxation in Q_A^--depleted *Cf. aurantiacus* RCs appears to have a larger amplitude contribution from the slow component than what is observed in *Rb. sphaeroides* RCs during the first 50 ps. Thus, the overall decay rate of the tryptophan absorbance change is slower in *Cf. aurantiacus* than in *Rb. sphaeroides*, even though the actual time constant of the slow component in Cf. aurantiacus is shorter than that in *Rb. sphaeroides* RCs. Previous resonance Raman measurements by Cherepy et al. showed a frequency downshift in the low-frequency (29-100 cm^{-1}) region of the special pair in *Cf. aurantiacus* RCs as compared with *Rb. sphaeroides* RCs[139]. The small frequency downshift can be interpreted as porphyrin ring core size expansion due to an increase in the low-frequency anharmonic vibrations of the

protein[140, 141], which is consistent with the observation of the increased weight of the slow protein diffusion kinetic components in the *Cf. aurantiacus* RC.

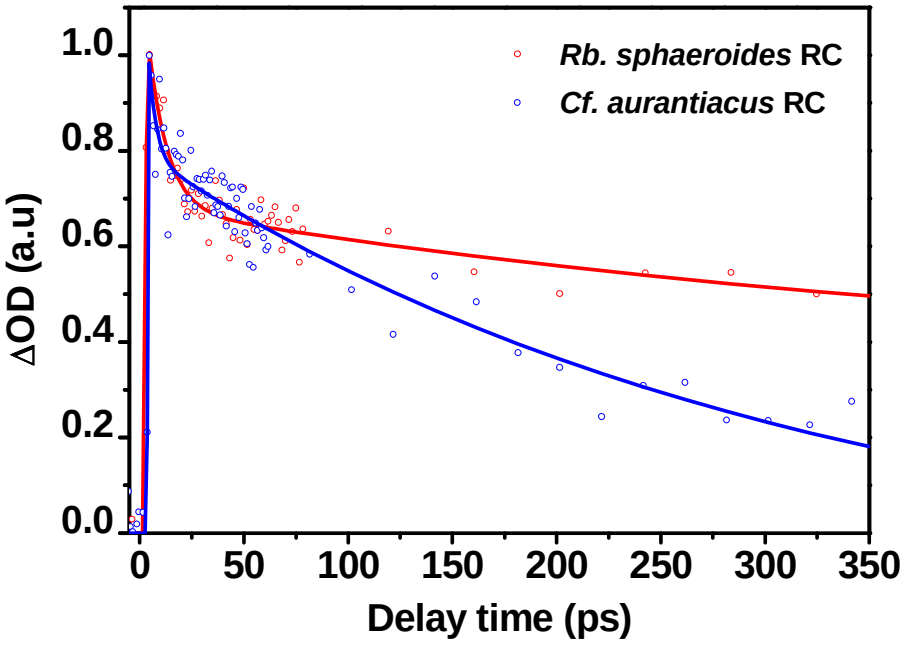

Figure 2. Room temperature tryptophan absorption change kinetics probed at 280 nm. Red open circles represent Q_A-depleted *Rb. sphaeroides* RCs and blue open circles represent Q_A-depleted *Cf. aurantiacus* RCs. Smooth curves are the results of a three-exponential fit.

Temperature dependence of the initial electron transfer in *Cf. aurantiacus* vs. *Rb. sphaeroides* RCs

The only transient absorption study of the temperature dependent kinetics of initial electron transfer in *Cf. aurantiacus* RCs was performed in 1991 using Q_A-containing RCs embedded in polyvinyl alcohol films between 80 and 320 K[128]. A 10 Hz laser was used to avoid the accumulation of closed reaction centers in the sample and excitation was at 605 nm. At that time, it was not possible to

excite P directly in the near IR and the time resolution of the instrument was limited to about a picosecond. The P* decay kinetics at room temperature (296K), when fit to a single exponential decay term, gave a lifetime of 7.1 ps. At 320K, the single exponential lifetime increased slightly to 9.0 ps. The kinetics measured over most of the temperature range were clearly heterogeneous, with biexponential fits at 80 K giving lifetimes of about 2 and 23 ps. Stretched-exponential fitting of the decay as a function of temperature suggested that above 200 K, the kinetics approached single exponential. The only temperature-dependent studies performed below 80 K used the fluorescence decay to estimate the electron transfer kinetics[142]. In this case, the RCs were in the state PQ_A^-, generated by white light illumination in the presence of an electron donor to re-reduce P. The measurements under these conditions gave much longer times for P* decay, with two time constants of 20 ps and 300 ps, possessing a 1:1 amplitude ratio and exhibiting a very weak temperature dependence over the measured range.

In order to better understand the temperature dependent kinetics of electron transfer in *Cf. aurantiacus*, and be able to compare it in detail to that of *Rb. sphaeroides*, transient absorbance measurements of quinone-depleted reaction centers were performed between 10 and 294K exciting directly into the Q_Y band of P at 860 nm. Current ultrafast spectroscopic equipment not only allows direct excitation of P, but provides a much higher time resolution and much greater signal-to-noise ratios using much lower excitation energy. Figure 3 shows the P*

stimulated emission decay kinetics at 930 nm on a 40-ps time scale at selected temperatures.

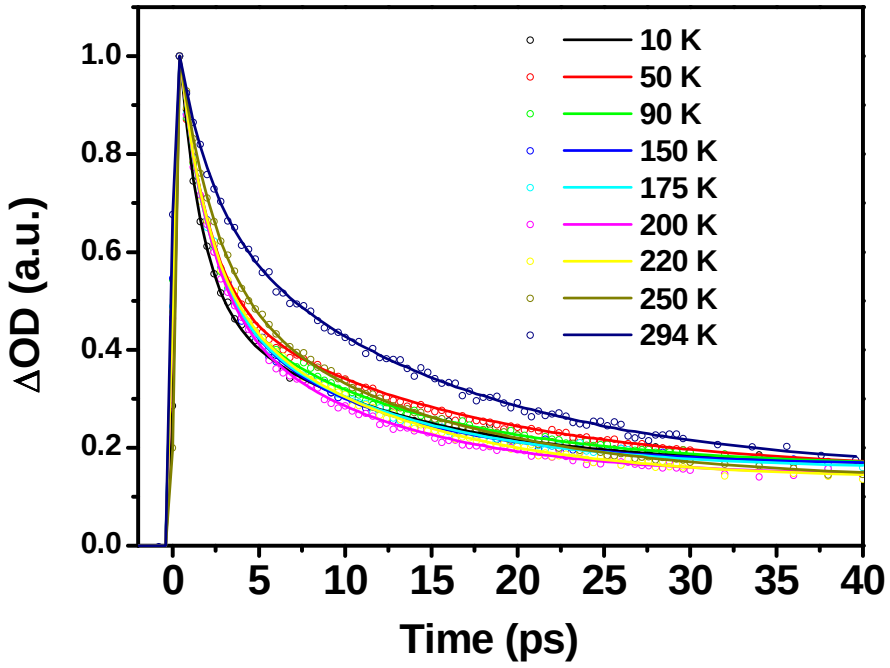

Figure 3. Temperature dependence of the P* decay kinetics in *Cf. aurantiacus* RC over the first 40 ps, probed at 930 nm (signal is inverted for clarity).

The solid lines result from two-exponential fits of the data (discussed in the following paragraph). The P* kinetics of Q_A-depleted *Rb. sphaeroides* RCs were also measured using the same protocol (see below). For *Cf. aurantiacus* RCs, at least two exponential components and a non-decaying component are required to describe the kinetics at early times (<40 ps) over the entire temperature range measured. This model provides a qualitatively accurate kinetic picture during the first 40 ps and will be used to compare the kinetics of *Cf. aurantiacus* vs. *Rb.*

sphaeroides reaction centers at early times as a function of temperature. However, measurements over longer time periods clearly show more complex kinetic heterogeneity that is best described with the sum of two stretched-exponentials.

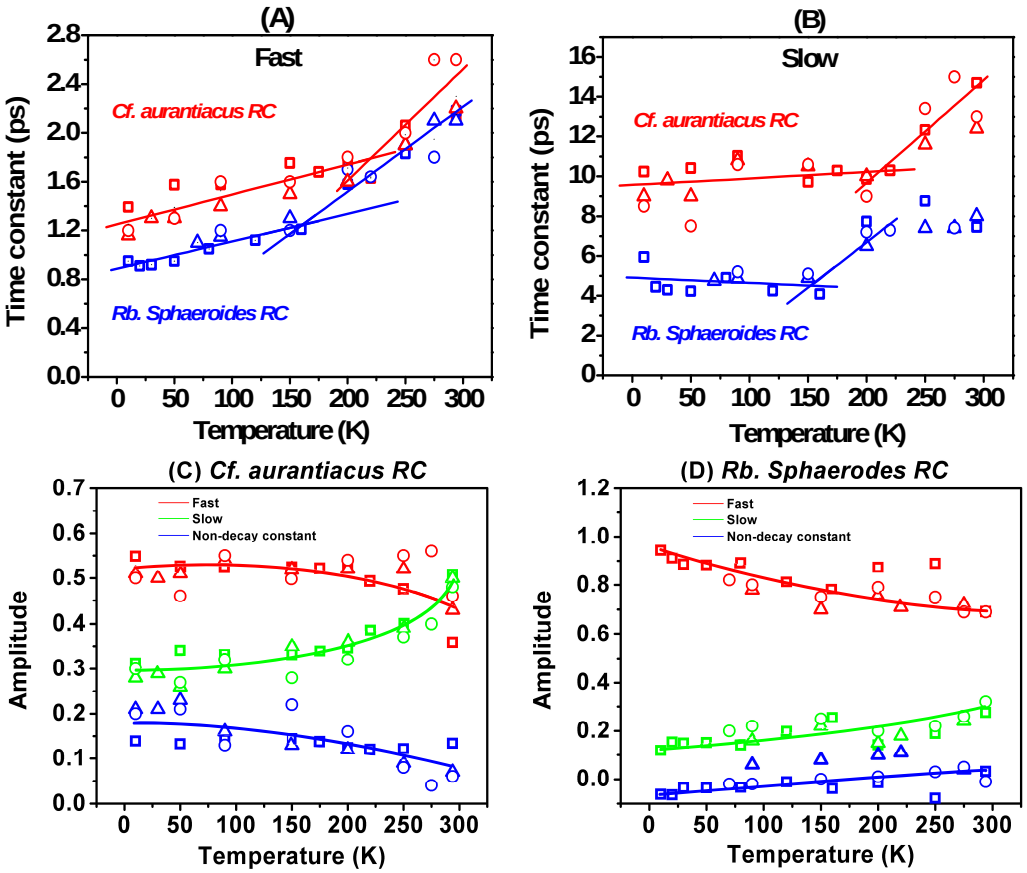

Figure 4. Decay lifetimes and relative amplitudes of P* decay kinetics as a function of temperature, obtained from fitting over the first 40 ps kinetics using 2 exponential components and a non-decaying term. Decay lifetimes of the A) fast and B) slow components as a function of temperature. Red represents *Cf. aurantiacus* RCs, blue represents *Rb. sphaeroides* RCs. The amplitude of each component as a function of temperature: C) *Cf. aurantiacus* RCs. D), *Rb. sphaeroides* RCs. The experiments have been repeated three times for each (represented by square, triangle, and circle symbols respectively).

In the following analyses the results from fits using two exponential components plus a non-decaying term (based on 40-ps kinetics traces) will first be presented, as this allows a simple way of understanding the overall temperature dependence of the early time kinetics. Then, the results from using a two-component stretched-exponential fit (based on 350-ps kinetics traces) will be analyzed. This provides a means of understanding the temperature and species dependence of the kinetic heterogeneity, as the β term is a measure of the width in the distribution of kinetic components.

Figure 4A and B show P* decay lifetimes as a function of temperature, obtained from a fit with two exponential decay components and a non-decaying term for Q_A-depleted RCs of both *Cf. aurantiacus* and *Rb. sphaeroides*. At all temperatures, the fast-decaying lifetime for *Cf. aurantiacus* RCs is between 1 and 2 ps (3 ps in buffer without cyroprotectant at room temperature), while the slow lifetime varies between 10 and 15 ps. The fast-decay time constant gradually increases as the temperature is raised from 10 K to about 220 K, then a steeper increase occurs at 220 K. The slow-decay time constant does not show significant change in the 10 K to 220 K region before a sharp increase occurs at 220 K. Similar shifts in the electron transfer rate constants occur in *Rb. sphaeroides* RCs, most clearly in the longer component lifetime, at around 160 K. The temperature range at which a sharp rate change takes place is similar to other studies that investigate the temperature dependence of the atomic mean square displacement in protein and polymer systems[143, 144], referred to as the dynamic transition temperature or the dynamic crossover temperature. The current view on this

phenomenon is that it is related to the beta-relaxation processes of the protein hydration layer[145], and a phenomenological explanation is an abrupt increase in the protein conformational entropy with increasing temperature, where the molecular collective motion converts from harmonic to anharmonic, mostly driven by the solvent interactions. Many thermodynamic quantities will correspondingly experience a transition at this temperature (e.g., reorganizational energy[146]).

Figure 4C and D compare the relative amplitudes of each kinetic component of the two samples and their temperature dependence. The amplitude of the fast component from *Rb. sphaeroides* RCs dominates at all temperatures below 250 K and shows little temperature dependence. The amplitude ratio of the fast to slow components decreased from 7.8:1 at low temperatures to 2.5:1 at room temperature. A similar bi-exponential decay of P* kinetics has been observed in RCs from other species of purple bacteria[147-149]. In *Cf. aurantiacus* RCs, the contribution from the slow component at all temperatures is significantly higher than that observed in *Rb. sphaeroides*. The amplitude ratio between the fast and slow components decreases from 1.75:1 to 0.7:1 as the temperature increases from 10 K to 295 K, crossing 1 at around 250 K. The amplitudes of the kinetic components are not extremely temperature dependent.

As mentioned above, at low temperatures, the non-exponential character of the P* kinetics is particularly pronounced in *Cf. aurantiacus* RCs, with obvious decay kinetics extending beyond the 40 ps range. In the double-exponential analyses above, this long-lived component was treated as a non-decaying

component and accounted for 10-15% of the overall amplitude. A two-component, stretched-exponential function allows the long decay components to be incorporated into the stretch index parameter for explicit consideration. We applied this method to the analysis of P* kinetics in *Cf. aurantiacus* RCs over a 350 ps time window. Figure 5 shows the variation of the stretched-exponential parameters with temperature. The stretch index (β) of the fast component (Figure 5A), starts near 0.8 at room temperature and gradually approaching 1 at temperatures below 90 K, suggesting that this fast decay process can be fairly well-described by a single relaxation process at all temperatures and a nearly pure single exponential process at very low temperature. The narrowing in the kinetic distribution below 90 K is likely due to a limited protein nuclear diffusion along the electron transfer reaction coordinate on the ps time scale (average lifetime ,τ, is 1~2 ps). For such short time periods, the protein motion is dominated by high-frequency covalent bond vibration and hydrogen bond fluctuation, leading to a quasi-harmonic coupling between these motions and the electron transfer reaction. In contrast, the slow component is more dispersive. Since the β parameters of both the fast and the slow stretched exponentials approach 1 at room temperature, it may be reasonable to model the room temperature electron transfer rate as bi-exponential. However, the stretch index of the slow component drops from 0.76 (at room temperature) to 0.5 (at 10 K), suggesting an increasingly dispersive lifetime distribution with decreasing temperature. The dispersive nature of the kinetics may be associated with conformational trapping at low temperatures, and more long-lived P* relaxation processes.

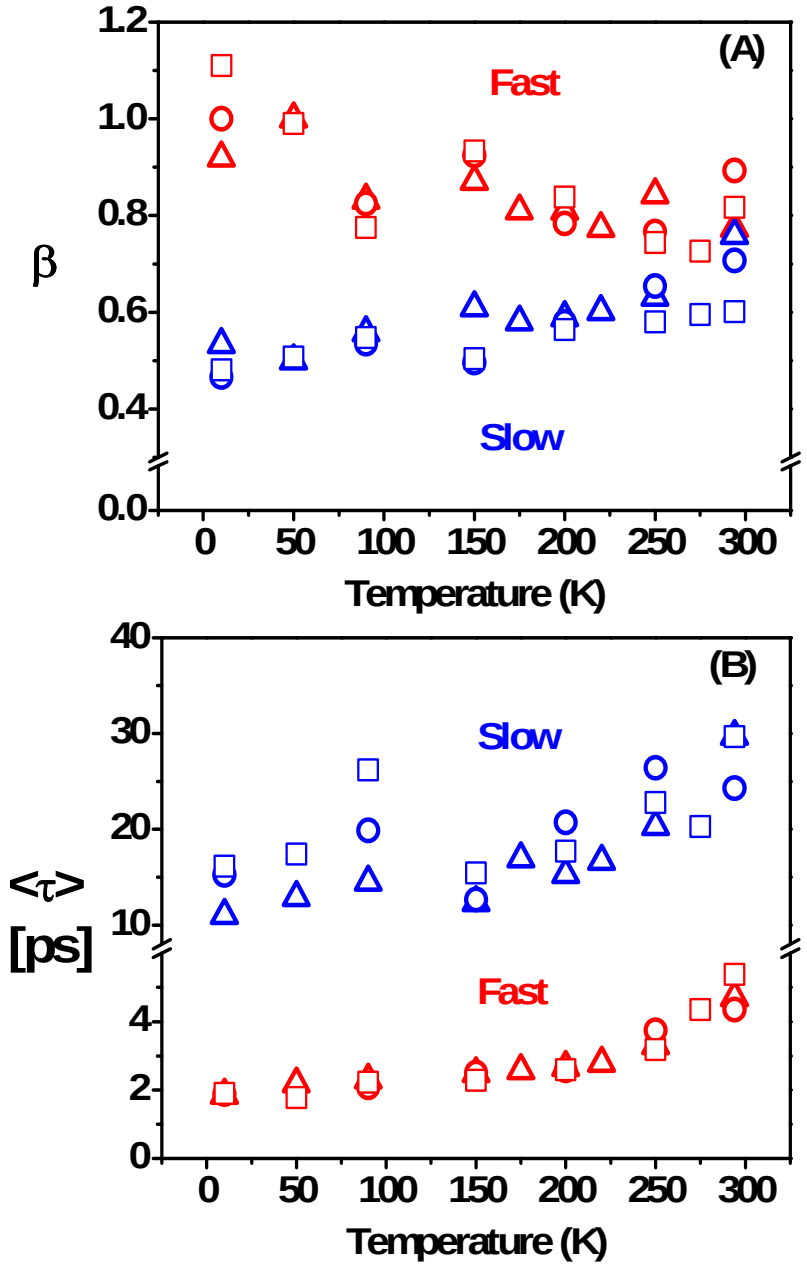

Figure 5. Two-component stretched-exponential fit performed on the 350 ps P* decay kinetics traces of *Cf. aurantiacus* RCs measured at all temperatures. A) Stretched-exponential indices, **β,** as a function of temperature. B) The average lifetime constants, <**τ**>, calculated using the formula described in Material and Methods.

Discussion

Temperature-dependent kinetics in RCs from *Cf. aurantiacus* and *Rb. sphaeroides*

While there are substantial structural and functional similarities between the RCs of *Cf. aurantiacus* and *Rb. sphaeroides*, there are clearly detailed differences in the spectrum and the charge separation process. Perhaps the most obvious structural difference is that the B_B cofactor in *Rb. sphaeroides* is replaced with a bacteriopheophytin in *Cf. aurantiacus*. However, the cofactor swap is clearly not the whole story, and may not be the most important difference functionally. This can be seen by considering the *Rb. sphaeroides* mutant M182HL in which B_B has been replaced with a bacteriopheophytin, resulting in the same cofactor composition as in *Cf. aurantiacus*[150]. Interestingly, the ground state absorbance spectra of the M182HL mutant and the *Cf. aurantiacus* RC are quite different. The Q_y absorption band of the newly-introduced BPheo in the M182HL mutant is located at 785 nm, close to the accessory BChl absorption, while in *Cf. aurantiacus* RCs, the Q_y absorption band of all three BPheo cofactors peak near 756 nm. At room temperature, 35% of the electron transfer occurs along the B-branch in the M182HL mutant, while electron transfer in *Cf. aurantiacus* RCs apparently occurs almost exclusively along the A-branch at all temperatures[151]. All of these phenomena suggest that the detailed protein environment is functionally quite different between the two organisms. Recently, Pudlak and his coworkers used a five-site kinetic model to numerically simulate the electron transfer behavior of two branches between *Rb. Sphaeroides* and *Cf.*

aurantiacus RCs[152]. The results suggest different mechanism of the unidirectional electron transfer exists in two organisms.

The temperature-dependence of the electron transfer kinetics in *Rb. sphaeroides* RCs and *Cf. aurantiacus* RCs differs in several ways. A biexponential analysis of the early time data (tens of picoseconds) shows that both RCs have a fast component lifetime of 1-3 picoseconds and then a longer lifetime in the 4-15 ps range depending on the species and the temperature (Fig. 4). The electron transfer is, overall, faster in *Rb. sphaeroides* RCs than in *Cf. aurantiacus* at any temperature. This is because in *Rb. sphaeroides* the contribution from the fast component dominates the overall electron transfer kinetics. In contrast, the amplitudes of the fast and slow decay components in *Cf. aurantiacus* RCs are more comparable at all temperatures and the slow component actually dominates near physiological temperature. The temperature at which there is a sharp change in the kinetics of electron transfer also differs between *Rb. sphaeroides* and *Cf. aurantiacus RCs*. This transition occurs at a higher temperature (~220 K for both the fast and the slow components) for *Cf. aurantiacus* RCs than it does in *Rb. sphaeroides* RCs (~150 K for the slow component and a less obvious transition between 100 and 150 K for the fast component).

It has been known for many years that *Rb. sphaeroides* RCs undergo protein conformational changes associated with charge separation and that some of those changes depend strongly on temperature[153, 154], with the most pronounced changes occurring near 150 K. In addition, resonance Raman spectroscopy has indicated relatively sharp changes in specific vibrational modes in a similar

temperature range[155, 156]. The temperature dependence of electron transfer in *Rp. viridis* and *Rb. capsulatus* RCs (both mesophillic organisms) indicates a transition temperature very similar to that seen in *Rb. sphaeroides* [148, 157, 158].

Multiple types of protein-protein and protein cofactors interactions may be involved in controling the transition temperature in the electron transfer kinetics. A comparison between the RC amino acid sequences of the two species suggests that *Cf. aurantiacus* RCs may have fewer hydrogen bonding interactions with their cofactors than do *Rb. sphaeroides* RCs. In particular, glutamic acid L104 which hydrogen bonds to H_A and histidine L168 which forms a hydrogen bond with P_A in *Rb. sphaeroides* are glutamine and phenylalanine, respectively, in *Cf. aurantiacus*. The vibrational relaxation properties of BChl *a* in solution apparently depend on the hydrogen-bonding capability of the solvent[159], again consistent with the idea that specific hydrogen bonds may affect the vibrational coupling associated with BChl *a* on the nanosecond time scale and further change its temperature dependent behavior. In addition to specific protein/cofactor interactions, temperature dependent changes in the dielectric nature of the protein environment can affect the overall electron transfer kinetics. Recent molecular dynamics simulations of the *Rb. sphaeroides* RC, as well as the small electron carrier plastocyanin, have suggested that the dynamic columbic interactions between proteins and local solvent molecules on the protein surface may play an important role in determining temperature dependent changes in the dynamic behavior of the protein and its immediate solvent shell transitions[146, 160].

Table 1. Amino acid compositions from various reaction centers, statistics are assembled by ProtParam module from ExPASy proteomics server.

		***Cf. auranti acus* J-10-fl RC**	***Rb. sphaeroid es* 2.4.1 RC**	***Rhodoseu domonas. viridis* RC**	***Rb. capsulatu s* SB 1003 RC**
L branc h	**Number of Positively charged residues (+)**	24	14	16	14
	Number of Negatively charged residues (-)	20	14	14	13
	Aliphatic index	85.27	102.45	97.88	93.05
	Grand Average of Hydropathy	0.286	0.586	0.468	0.551
M branc h	**Number of Positively charged residues (+)**	18	17	19	20
	Number of Negatively charged residues (-)	15	14	18	14
	Aliphatic index	91.27	94.45	88.61	90.00
	Grand Average of Hydropathy	0.333	0.436	0.342	0.394

The amino acid composition of *Cf. aurantiacus* RCs is compared with three RCs from purple bacteria in Table 1. Generally speaking, the *Cf. aurantiacus* RCs contain more charged residues and fewer aliphatic residues, especially in the L subunit. Sequence alignment (http://blast.ncbi.nlm.nih.gov/)

and structural comparison indicate that 10 out of the 14 non-charged-to-charged residue changes from *Rb. sphaeroides* to *Cf. aurantiacus* RCs in the L-subunit are located at the periplasmic membrane surface. These charged residues presumably form ion pairs and optimize the surface electrostatic interactions (both protein/protein and protein/solvent) to stabilize the structure at high temperature, as has been seen in other thermophilic proteins[161]. Dipole reorientation at the protein-water interface appears to be a critical factor in inducing the protein structural fluctuation, especially at higher temperatures[162]. The non-decaying component that results from a double exponential analyses or *Cf. aurantiacus* RC kinetics has a life time of 100~200 ps, which is comparable to the bulk protein electrostatic relaxation lifetime that has been estimated for *Rb. sphaeroides* RCs[163]. This is also consistent with the observation of a more distinct temperature transition for the slow component from a two exponential analysis (Fig. 4b). The effect of dynamics at the protein-water interface is necessarily less on the picosecond time scale, as this is too fast for most collective protein motions, but the temperature-dependent transition in the kinetics is still apparent. In addition to the protein surface differences between *Cf. aurantiacus* and *Rb. sphaeroides* RCs discussed above, the lack of an H-subunit in *Cf. aurantiacus* RCs may also result in more direct exposure of protein surfaces to water in comparison with *Rb. sphaeroides* RCs, increasing solvent associated effects.

Using the reaction diffusion model to explore electron transfer parameters at room temperature

In *Rb. sphaeroides* RCs, it has been previously shown that the detailed electron transfer kinetics can be accurately represented using a reaction diffusion model in which protein dynamics controls the rate of electron transfer[83]. This model contains several important parameters including the electronic coupling, the driving force, the time dependent conformational diffusion, and fast and slow reorganization energy. The surprising thing about the application of this model to *Rb. sphaeroides* RCs is that it was possible to describe the complex and widely varying kinetics of a large number of mutants that specifically changed the driving force for electron transfer by varying only that parameter between mutants.

One question is whether that analysis can be extended to *Cf. aurantiacus* RCs and if so, which parameters will change and which will remain the same. Two of the parameters can be obtained from experimental data. Volk and coworkers used magnetic field dependent reaction yield measurements to estimate the standard free energy gap between P* and $P^{+}H_{A}^{-}$ for the RCs of both *Rb. sphaeroides* and *Cf. aurantiacus*. They found that the driving force for *Cf. aurantiacus* RCs was 0.04eV lower than that of *Rb. sphaeroides* RCs[133]. Thus, for the analysis below, the driving force for *Cf. aurantiacus* RCs will similarly be set 0.04 eV below the value previously determined in modeling *Rb. sphaeroides* RCs (0.197 eV). In addition, the measured Trp decay for *Cf. aurantiacus* RCs

(Figure 2) will be used to derive the time dependent diffusion term, as described previously[83]. All other parameters will be held as they were in *Rb. sphaeroides.*

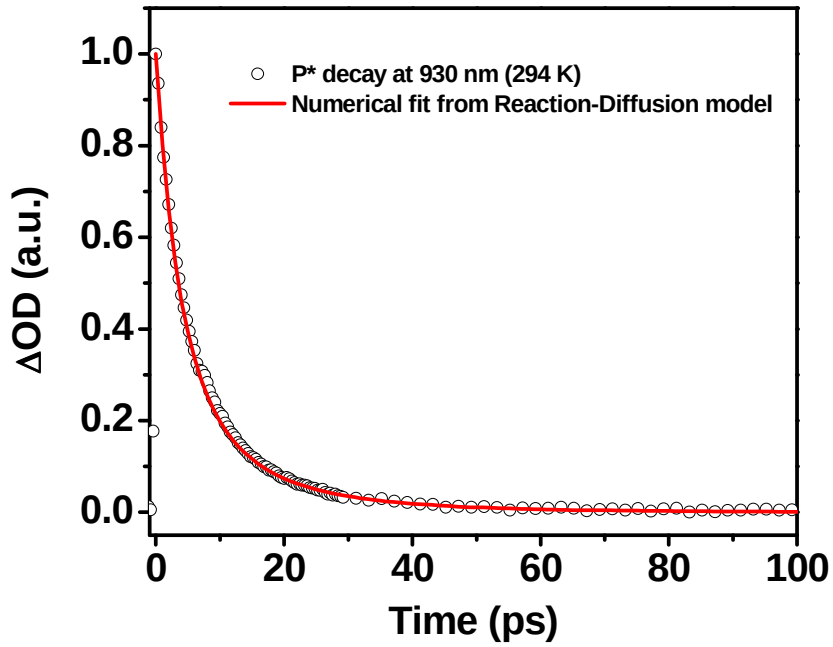

Figure 6. A fit of the P* decay in *Cf. aurantiacus* reaction centers monitored at 930 nm (circle) using the reaction diffusion model[31]. All of the parameters used in the fit were either experimentally derived from independent measurements or taken from the fitting parameters previously determined for *Rb. sphaeroides* (see Methods).

Fixing these two parameters at their measured values and changing nothing else results in essentially perfect simulation of the room temperature *Cf. aurantiacus* kinetics for the first 100 ps (Figure. 6). One might have expected that the reorganization energies associated with *Cf. aurantiacus* RC initial electron transfer would have been substantially different from those of *Rb. sphaeroides*. However, comparisons between them in the B_A^- absorbance oscillatory spectra at 90 K[164], and also the resonance Raman spectra at room temperature[139] have

suggested that distribution of intramolecular motions that likely contribute to the reorganization energy on this time scale are actually quite similar between the two organisms. In practice, the two reorganization energies can be varied by about 0.02 eV before the fit deviates significantly from the data.

Supporting Information

Figure S1-S3 provide additional spectroscopic data for Q_A-containing and Q_A-depleted *Cf. aurantiacus* RCs. A mathematical form of the reaction-diffusion model for electron transfer is also provided.

Supplemental Data

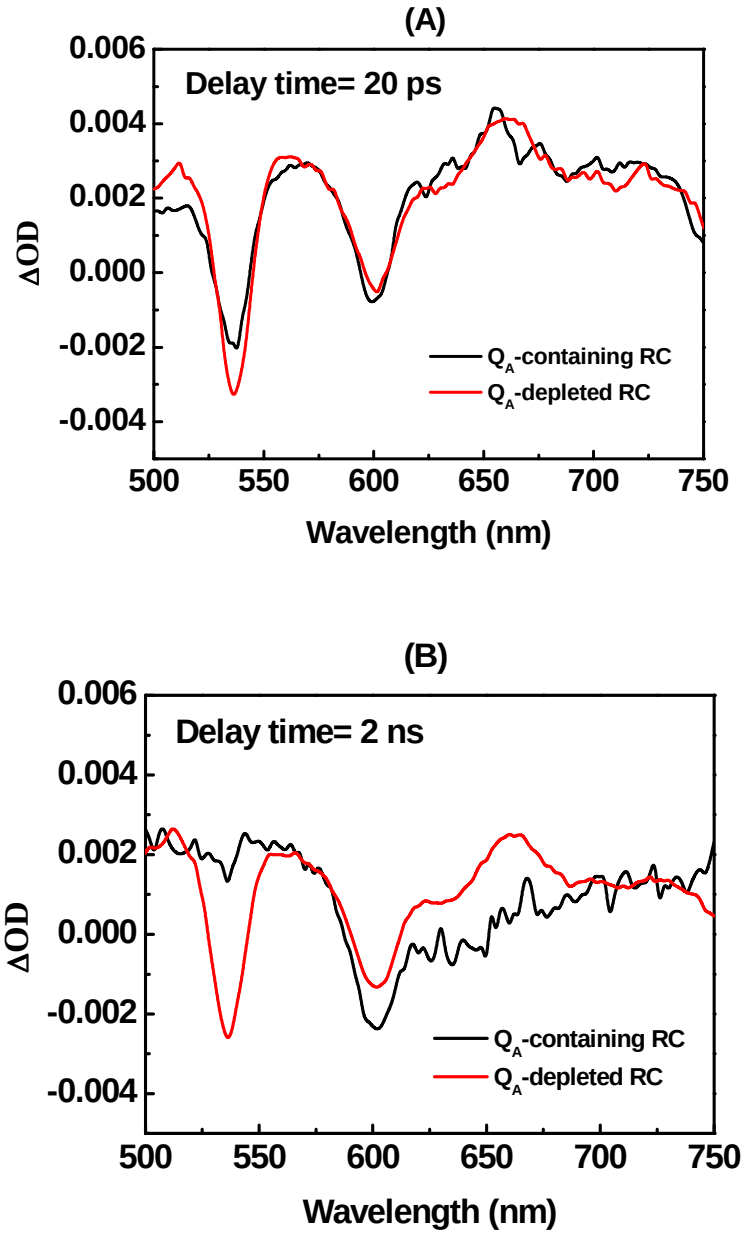

Figure S1. Transient absorption spectra of Q_A-containing and Q_A-depleted RCs, from *Cf.aurantiacus*, recorded at (A) 20 ps and (B) 2 ns after laser excitation at 860 nm.

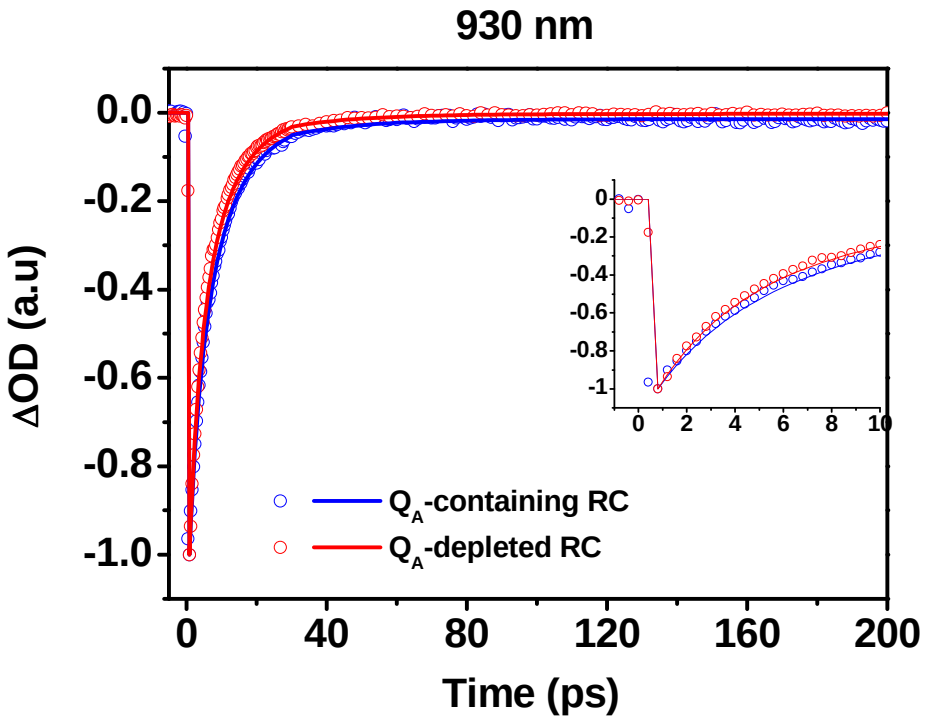

Figure S2. Kinetics of stimulated emission from P* at 930 nm; measured at room temperature (294 K). Blue open circles represent Q_A-containing *Cf. aurantiacus* RCs and red open circles represent Q_A-depleted *Cf. aurantiacus* RCs. The solid lines are the fitting curves obtained from three exponential fitting. The inset shows the kinetics of the first 10 ps after laser excitation.

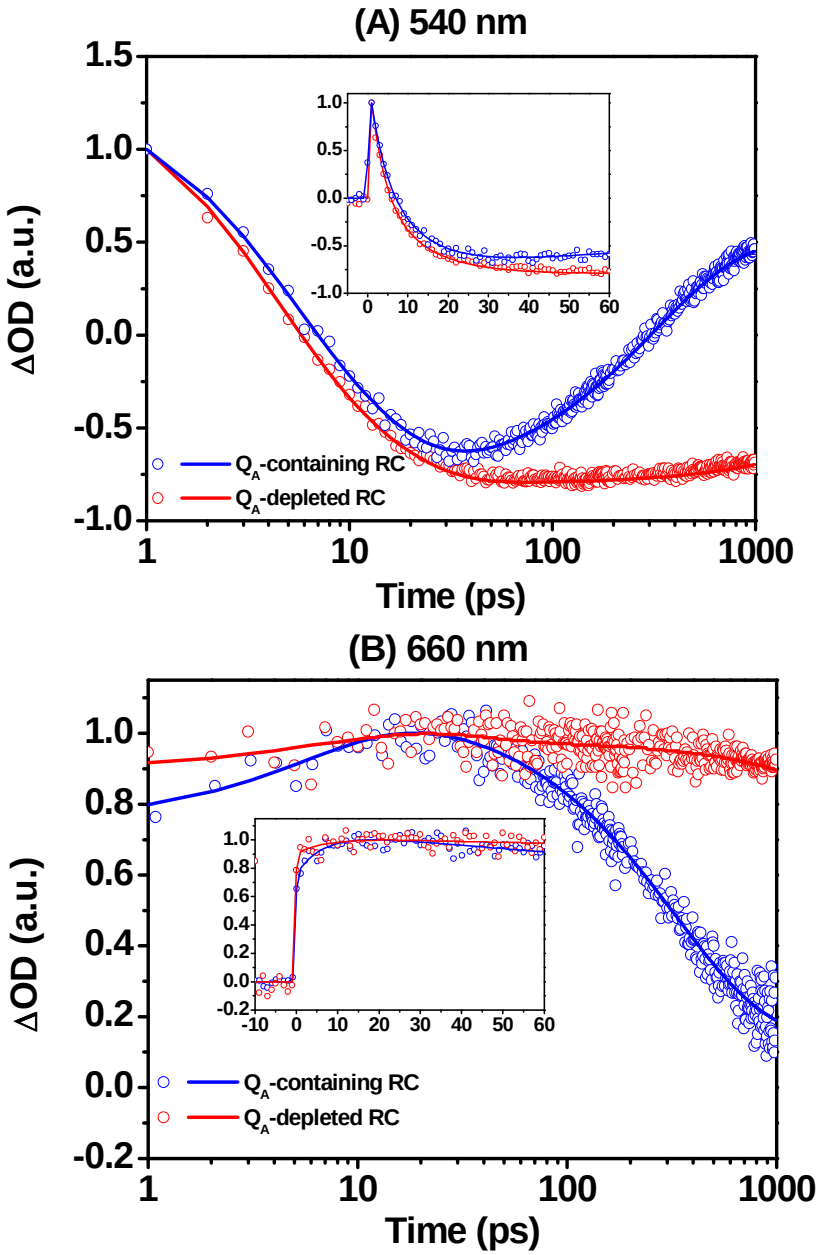

Figure S3.(A) Absorption change kinetics of bacteriopheophytin (H_A, 540 nm) and (B) its anion state (H_A^-, 660 nm); Insets are the early time kinetics plotted in a linear time scale. Color scheme: blue represents Q_A-containing *Cf. aurantiacus* RCs, red represents Q_A-depleted *Cf. aurantiacu*s RCs. The solid lines are the fitting curves given by three exponential components.

CHAPTER 3

Electron transfer pathway modulated by protein dielectric relaxation

Introduction

In Marcus's treatment of electron transfer[165], the free energy required to drive charge separation between the donor and acceptor is modeled in terms of charge polarization, using the amount of polarized charge as the reaction coordinate. One important parameter in this model, as well as in all dielectric continuum models, is the dielectric constant. Originally, the response of the system was divided into its nuclear and electronic terms, and the dielectric constant was accordingly separated into an optical dielectric constant ε_o (the high frequency limit, corresponding to electronic polarization), and static dielectric constant ε_s (the low frequency limit, corresponding to nuclear polarization). For most electron transfer processes in condensed phase being considered, such homogenous dielectric continuum model is not enough because many length scale dependent time scales are involved in the nuclear motion[166]. In a dynamic arresting picture, the electron transfer rate sets a high frequency cut-off limit and defines the frequency window for selecting the nuclear motion that are involved. The frequency dependence of the dielectric response is important because it determines which non-ergodic region the reaction is going to enter.

Electron transfer in proteins is different from that of soluble donor/acceptor systems, in that the charge distribution is spatially constrained, or in other words,

the translational and rotational motions of reactants are greatly confined by the protein structure compared with molecules free in solution. This structural constraint results in a relatively long memory in the dielectric relaxation kinetics which can give rise to complex reaction kinetics. For those nuclear motions that are both coupled to electron transfer and occur on a similar time scale, their kinetic distribution in the frequency domain becomes an important aspect of any model that hopes to accurately describe the electron transfer dynamics. The primary electron transfer reaction in the photosynthetic reaction center has become a paradigm for protein mediated charge separation. This reaction has been successfully described using the reaction-diffusion model (as a function of mutationally altered driving force and of temperature), using a measurement of the dielectric relaxation dynamics as input[83, 167].

Though it may seem somewhat counter intuitive, the primary electron transfer is probably the simplest of the reaction center mediated electron transfer reactions in which to explore and model the role of protein dynamics. This is because on the picosecond time scale, relatively little moves, and what does are small scale motions that are likely relatively homogeneous. The electron transfer in the photosynthetic reaction center occurs on slower time scales as well. In addition to the ~3 ps in $P^* \rightarrow P^+H_A^-$ primary charge separation, there is the secondary electron transfer to Q_A in hundreds of picoseconds, transfer between the quinones in microseconds and various charge recombination reaction that takes place from charge separated intermediates on time scales from nanoseconds

to seconds. On time scales longer that picoseconds, larger scale and structurally heterogeneous dynamics come into play.

The protein dielectric response function has biologically evolved to optimize both the initial electron transfer from P* via $P^+B_A^-$ forming $P^+H_A^-$ and the subsequent transfer forming $P^+Q_A^-$. Simultaneously, charge recombination, which competes with forward electron transfer at each step, must be avoided. This study focuses on the protein environment of the monomber bacteriochlorophyll B_A and the bacteriopheophytin H_A, both of which play multiple roles in the electron transfer process on timescales from picoseconds to hundreds of picoseconds. H_A accepts an electron via B_A during primary electron transfer and then either donates the electron to the next electron acceptor Q_A or returns it to P, presumably again via B_A, regenerating the ground state. The overall time constants for the $H_A \rightarrow Q_A$ electron transfer and the $P^+H_A^-/PH_A$ recombination are 200 ps and 10~15 ns, respectively, in wild type RCs, though charge recombination has been shown to have components on faster time scales as well[26, 168]. The environment of B_A and H_A must be optimized for both reactions. This balance is presumably sensitive to both static and dynamic aspects of the dielectric environment. Of course, what is static on one time scale is dynamic on another, and this opens up possibilities for tuning reactions on different time scales by controlling the dynamics of the protein in the immediate vicinity.

The dielectric environment of a protein, on a phenomenological level, is influenced by the distribution and nature of charged groups within the structure. The dynamic response of the protein during electron transfer depends both on

where charges and other polar groups are placed and on the effective time-dependent dielectric constant. It is possible to use site-directed mutagenesis to localize a charge at a specific site within a protein. Such an additional charge should make the local environment more polarizable and increase the effective dielectric constant compared with the wide type.

Here, the effect of varying the dielectric environment in the region of B_A and H_A is explored by replacing tyrosine at position M210 with an aspartic acid, thus potentially altering both the static and dynamic dielectric nature of the environment. Three different electron transfer reactions, primary electron transfer forming $P^+H_A^-$, charge recombination from $P^+H_A^-$ to the ground state and forward electron transfer from H_A^- to Q_A, are monitored, all on different time scales.

Materials and Methods

Two new mutants at M210 site were prepared by replacing the original condon (TAC) for tyrosine with GCA (Ala) and GAT (Asp) respectively. The mutagenesis was performed as previously described[169]. RCs were grown and isolated according to previously described procedures[170]. For mutants that are not involved in pH dependence study, those samples were suspended in 50 mM Tris-HCl (pH=8.0), 0.025% LDAO, 1 mM EDTA. In the pH dependence study, the wild type RC and its M210YD mutant were transfer to a higher pH environment (pH=9.5) by doing a buffer exchange, a pH=9.5 CLE buffer was used, and more details have been described in earlier publications[171]. The quinone removal was routinely performed by continuously eluting the sample with high concentration

LDAO detergent (4%) buffer with *o*-phenanthroline. The final product absorption does not show significant degradation judging from the relative intensity of the major absorption peaks. In quinone containing RCs, 1 mM *o*-phenanthroline was added to block the electron transfer to Q_B during transient absorption spectroscopy experiments.

Transient absorption spectroscopy measurements were performed with a pump-probe setup. Laser pulses were generated at a repetition rate of 1 kHz with 130 fs duration at 800 nm using a regenerative amplifier system based on a Titanium:Sapphire laser. Part of the beam was used to pump an infrared optical parameter amplifier (OPA-800, Spectra-Physics) to generate excitation pulse at 860 nm, and the other part was focus to a 3-mm sapphire plate. The white light generated was then compressed by prism pairs (CVI) before passing the sample. The polarization of pump beam was set to the magic angle (54.7°) relative to the probe beam. The white light probe is dispersed by a spectrograph (300 line grating) on a charge-coupled device (CCD) camera (DU420, Andor Tech.). The final spectral resolution is about 2.3 nm for a nearly 300 nm spectral coverage in either the Qx (480~780 nm) or the Qy (680~980 nm) region. For the measurement of B_A^- transient absorption, 600-line grating was used, which provides a 1.2 nm spectral resolution in the 980~1040 nm region.

The time-resolved spectra were analyzed either with a locally written global analysis program (ASUFIT 3.1, http://www.public.asu.edu/~laserweb/asufit/asufit.html) for global analysis, or a program from Ivo M Stokkum that solves the sequential models (Glotaran,

http://glotaran.org/). To estimate of the protonation state of the aspartic acid in M210 site, the Multi-Conformation Continuum Electrostatics (MCCE) method was used[172, 173]. The crystal structure used for this study is taken from the PDB data bank, PDB id 1AIJ. The *in silico* mutagenesis was performed in Pymol followed by structural relaxation in the MCCE program. All the titratable groups that were 4 Angstroms within the M210 "hot spot" were selected to generate 12 rotamers per rotatory degree of freedom for enhancing conformation sampling consideration. The protein dielectric constant was set to 4.0 and 8.0 (two conditions), and solvent dielectric constant was set to 80 with a 0.15 M salt strength. Delphi[174] was used as the Poisson-Boltzmann solver.

Results and Discussion

Measuring yield loss during charge separation

In wild type reaction centers, excitation of P results in the formation of $P^+Q_A^-$ in about 200 picoseconds via the series of reactions, $P^* \rightarrow P^+B_A^- \rightarrow P^+H_A^- \rightarrow P^+Q_A^-$, where the first reaction has a rate of about 3 ps, the second about 1 ps and final transfer to the quinone occurs in about 200 ps. At the same time, each of these states has some intrinsic rate for returning to the ground state. Thus the yield of charge separation at any particular point during this process depends on the competition between forward electron transfer and decay to the ground state. In wild type, at each step the forward reaction is usually taken to be 2-3 orders of magnitude faster than the intrinsic decay rate of the intermediate involved and therefore the yield of charge separation is close to unity throughout the process.

One can monitor this process in a number of ways, but one is to take advantage of the fact that, once light is absorbed, P leaves its ground state and remains out of its ground state throughout the process unless charge recombination occurs. Figure 1a shows the time dependent absorbance changes in the vicinity of the ground state band of P for wild type reaction centers. It is clear that the bleaching of the ground state absorbance centered at 860 nm overlaps both the time dependent changes associated with the B_A and B_B bands near 800 nm and with the broad stimulated emission band of P* that extends from about 850 nm to > 950 nm (Figure 1a). However, the blue side of the P ground state band in the 835-840 nm region seems to remain constant, at least during the initial reactions (Figure 1b), consistent with the near unity

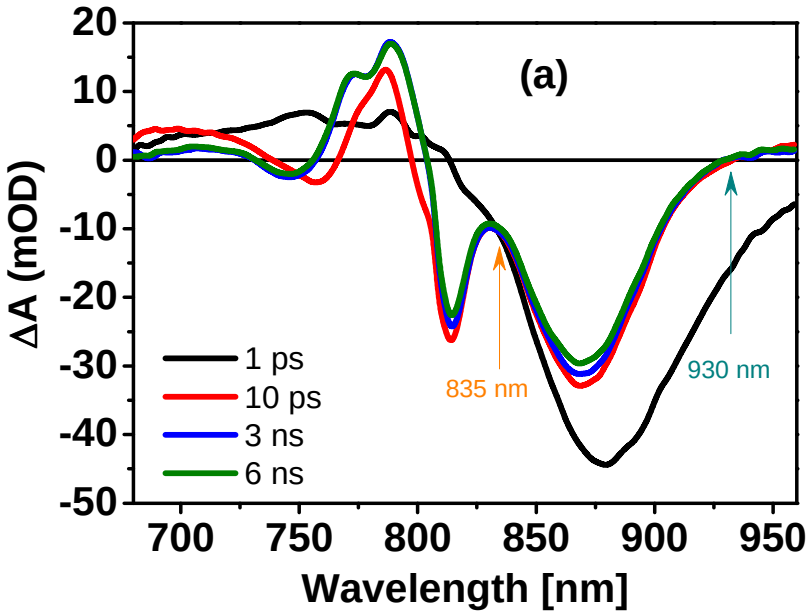

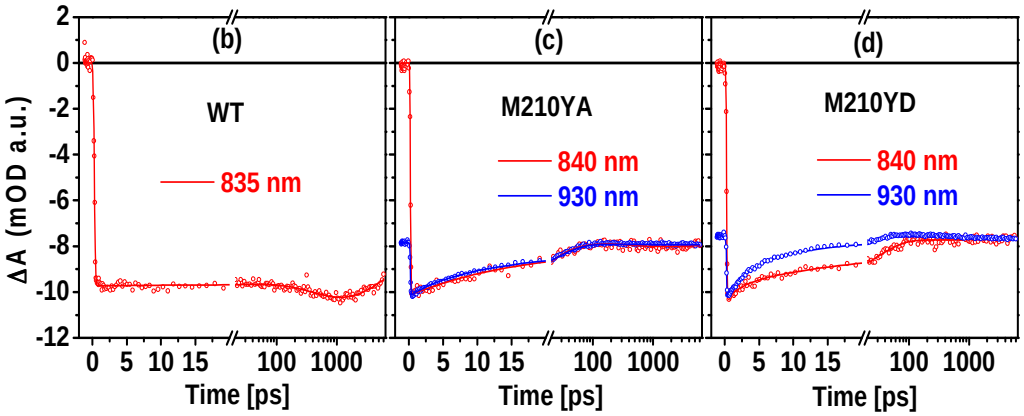

Figure 1 (a): Time-resolved spectra of the wild type RC in 680~960 nm spectral regions at 1 ps (P*), 10 ps ($P^+H_A^-$), 3 ns and 6 ns ($P^+Q_A^-$) after laser excitation at 860 nm. Arrows indicate the wavelengths where the kinetics were monitored in the lower panels. Lower panels: The P ground state bleaching recovery kinetics for wild type RC (b) and two of its M210 mutants (M210YA (c) and M210YD (d)) observed at 835~840 nm in a 6 ns probe window (shown in red, solid line for fitting curve, up to three exponential components plus a non-decay component was used). All samples were measured in pH=8.0 Tris/Hcl buffer. To illustrate the contribution of the intrinsic decay of P* to the early time quantum yield lost in the two mutants, P* stimulated emission kinetics measured at 930 nm was rescaled so that its bleaching maximum and the nanosecond decay kinetics match those of the 840 nm trace for comparison.

yield of charge separation in wild type (times after 200 ps will be discussed later). In mutant reaction centers where the yield is reduced, the absorbance at this wavelength decays with time.

M210YD mutant reaction centers undergo fast charge recombination

Figure 1c shows the results for M210YA in which a structurally important tyrosine near B_A has been replaced with alanine. As a result, the rate of initial electron transfer is decreased by about a factor of five in this mutant relative to wild type, as measured by monitoring the decay kinetics of the stimulated emission from P* at 930 nm. The initial electron transfer rate in M210YA is slow

enough that it does not compete as effectively with the intrinsic decay of P* as does forward electron transfer in wild type, and about 15% of the reaction centers return to the ground state during the P* lifetime. The result is that there is a ~15% decay at 835 nm (a recovery of P ground state) in concert with the decay at 930 nm (decay of P*) (Figure 1c). Based on this yield loss and the observed kinetics, one can also estimate the intrinsic decay time of P* in this mutant to be roughly 100 ps (Table 1).

Table 1 Decay lifetimes of the P* stimulated emission at 930 nm as well as the P ground state bleaching at 840 nm; both fit with 1 and 2 exponentials, and the quantum yield of the $P^+H_A^-$ state is estimated from ground state bleaching recovery kinetics at 835~840 nm.

Sample	**P* lifetime from 1-exponential fitting**	**P* lifetimes and relative amplitudes from 2-exponential fitting**	**P ground state bleaching recovery life time from 1-exponential fitting**	**P ground state bleaching recovery fitting results using 2-exponentials**	**Quantum yield of $P^+H_A^-$ state**
wild type pH=8.0	3.3 ps	2.5 ps (70%) + 6.4 ps (30%)			~100%
wild type pH=9.5	3.2 ps	2.7 ps (84%) + 9.4 ps (16%)			~100%
M210YF	12.7 ps	6.6 ps (53%) + 25.5 ps (47%)	12.8 ps	7.1 ps (30%) + 16 ps (70%)	~75%
M210YW	35 ps	9.4 ps (35%) + 55 ps (65%)	40 ps	19 ps (57%) + 103 ps(43%)	~75%
M210YA	17 ps	5.8 ps (35%) + 26.4 ps (65%)	17.7 ps	10.7 ps (26%) + 20.8 ps (74%)	~85%
M210YD pH=8.0	7.4 ps	3.5 ps (57%) + 17 ps(43%)	20 ps	3.4 ps (34%) + 33 ps (66%)	>85%
M210YD pH=9.5	8.2 ps	4.2 ps (60%) +19.7 ps (40%)	23 ps	6.2 ps (36%) + 42.2 ps (64%)	>85%

The intrinsic lifetime of P* in wild type reaction centers is thought to be on the order of two hundred picoseconds, though this value comes from similar analyses

of other mutants with charge separation yields less than unity[175-177]; the absolute yield has not been measured directly in wild type on this time scale.

When aspartic acid is substituted for tyrosine at M210 (M210YD), a rather different result is obtained. In this case, there is also some return of P to the ground state due to yield loss on the tens of picosecond time scale, however, the yield loss, as determined by monitoring P ground state recovery at 840 nm, does not follow the course of the stimulated emission decay at 930 nm (Figure 1d and Table 1). This implies that the observed yield loss does not simply result from an intrinsic P* decay that competes with forward transfer. Instead, it is dominated by a recombination reaction that occurs after initial charge separation. In wild type reaction centers, the charge separated states are very stable on this time scale, but apparently the introduction of aspartic acid at M210 results in charge recombination to the ground state that is rapid enough to compete with the subsequent forward electron transfer, either from B_A to H_A or from H_A to Q_A.

In wild type reaction centers, the electron transfer from B_A to H_A occurs with a time constant of about 1 ps[23, 25]. Thus, it is unlikely that recombination is directly competing with that rate on the tens of picoseconds timescale. Indeed, H_A^- formation in this mutant (8.0 ps at pH 8.0, measured at 670 nm as in Ref [178], data not shown) occurs on a time scale similar to P* decay (7.4 ps at pH 8.0, Table 1). Thus, the yield loss must occur subsequent to the formation of $P^+H_A^-$ and represents the competition between charge recombination from this state and forward electron transfer to the quinone. Charge recombination in $P^+H_A^-$ occurs on the 10 ns timescale in wild type and very likely involves formation of $P^+B_A^-$ as

an intermediate[179, 180]. In fact in some mutants, the standard free energies of $P^+B_A^-$ and $P^+H_A^-$ are probably close enough so that the charge separated state present at 10 ps is likely an equilibrium mixture[181-183]. Apparently some aspect of charge recombination is much faster in M210YD than in wild type.

The electron transfer reaction from H_A to Q_A in M210YD

The time course of electron transfer between H_A^- and Q_A^- can be determined by monitoring the decay of the bacteriopheophytin anion. Two most prominent signals associated with the H_A^- state are due to the bleaching of the ground state absorbance of H_A at 545 nm and the broad H_A^- absorbance around 670 nm. The results of global fitting across the 500 to 700 nm region for wild type and 4 different M210 mutants are summarized in Table 2. The H_A to Q_A electron transfer rate constant appears to be very similar in M210YF, M210YW and M210YA. In each case, the H_A^- decay kinetics are essentially single exponential and rate constants for all of these mutants is 20% of the wild type value. However, in the M210YD RCs, a substantially biphasic $H_A^- \rightarrow H_A$ decay is observed (Table 2). The fast time constant is similar to wild type, and has relative amplitude of 60%. The remaining amplitude is due to a much longer decay process with a time constant of 700-800 ps. Even though the kinetics is complex, and part of the transfer from H_A^- to Q_A is slow in M210YD, a comparison of these kinetics to the ground state bleaching of P shows that long after H_A^- has decayed, P^+ still remains (Figure 1d). Judging from this, the yield of $P^+Q_A^-$ is relatively

high, about 80% and in fact almost all the yield loss is on the tens of picosecond timescale rather than due to the slow component of the H_A^- to Q_A reaction.

Table 2 Time constants and associated relative amplitudes of the fast and slow component of H_A/H_A^- kinetic decay, obtained from global analysis in the 500~700 nm region using a sum-of exponential fitting.

RC Sample	Fast component	Slow component
wild type (pH=8.0)	240 ps [100%]	N.A.
wild type (pH=9.5)	214 ps [100%]	N.A.
M210YF	206 ps [100%]	N.A.
M210YW	252 ps [100%]	N.A
M210YA	262 ps [100%]	N.A.
M210YD pH=9.5	178 ps [60%]	717 ps [40%]
M210YD pH=8.0	270 ps [60%]	840 ps [40%]

Thus there are two aspects of M210YD that are distinctly different from wild type and other mutants at this position. There is recombination happening on the tens of picoseconds time scale and there is a fraction of the $P^+H_A^-$ state that does not undergo forward electron transfer on the 200 ps time scale, but instead takes several times longer. The mechanisms of these two processes are explored below.

Dielectric relaxation around B_A could facilitate early time charge recombination

Charge recombination from $P^+H_A^-$ has been effectively described in terms of an activated decay via $P^+B_A^-$[26, 27, 168, 179, 184-186]. Past measurements of the P* decay time as a function of driving force for initial electron transfer[83, 169, 187], suggest that in M210YD reaction centers (7~8 ps P* decay time), the $P^*/P^+B_A^-$ free

energy gap is decreased from wild type by no more than 30 meV. As in wild type, $P^+B_A^-$ is not accumulated during the reaction implying that electron transfer from B_A^- to H_A is much faster than the initial charge separation from P*. The H_A anion absorbance changes appear with a time constant that is essentially the same as the P* decay. Thus, it does not appear that on the time scale of the initial electron transfer reaction, the relative free energies of P*, $P^+B_A^-$, and $P^+H_A^-$ in the M210YD mutant are very different from wild type. However, this conclusion is difficult to reconcile with the observation of $P^+H_A^-$ recombination on the tens of picoseconds time scale. Such an unusually rapid recombination would suggest that $P^+H_A^-$ and $P^+B_A^-$ are very close in free energy, allowing a rapid decay of the equilibrated state via $P^+B_A^-$ recombination.

One possibility is that the relative free energy difference between $P^+B_A^-$ and $P^+H_A^-$ decreases rapidly in M210YD reaction centers after charge separation forming $P^+H_A^-$ is complete. As a result, the free energies of these two states are much closer together on the ten picosecond time scale than they were on the picosecond time scale. This in turn allows rapid charge recombination via $P^+B_A^-$. If true, this makes a prediction: it should be possible to observe a longer-lived population of $P^+B_A^-$ in M210YD in pseudo-equilibrium with $P^+H_A^-$.
Absorption changes near 1025 nm have been used successfully to characterize the transient population of B_A^- on sub-picosecond time scales[188]. Transient absorbance spectra in M210YD and wild type were recorded between 980~1040 nm over a broad time range, making it possible to follow processes from hundreds of femtoseconds to 1 ns. The spectral evolution in this region is complex, and the

absolute size of the signals of interest is small, making it difficult to follow the key states just by looking at the raw spectra. In order to facilitate visualization and analysis, the spectral evolution was modeled as a series of states that interconvert irreversibly (A→B→C→…). Obviously, in a situation where it is expected that back reactions are important, these will not represent pure states, but they do give a clean way of presenting the spectral progression with time without imposing a more complex, ad hoc kinetic model. This type of analysis has been referred to as Evolution Associated Difference Spectra (EADS[189]).

The number of states used in the EADS analyses in determined by the kinetic complexity of the data. Over a very large time frame such as this (four orders of magnitude) it is not possible to represent the data accurately with less than five kinetic components. This is not surprising as in the reaction scheme $P^* \rightarrow P^+B_A^- \rightarrow P^+H_A^- \rightarrow P^+Q_A^-$ there are three electron transfer steps, a well-documented sub-picosecond evolution of P* and, at least in the M210YD mutant, kinetic heterogeneity in the $H_A^- \rightarrow Q_A$ reaction. The application of such an analysis to wild type reaction centers (Figures 2a and 2b) gives results consistent with a similar analysis performed by Stokkum et al[190] when one takes into account their use of 800 nm excitation and the associated energy transfer. Of particular note, wild type shows a spectral species with a lifetime of about 0.9 ps with an EADS spectrum that peaks near 1025 nm (Figure 2a). This is consistent with $P^+B_A^-$ and as would be expected for a state that decays faster than it is formed, as it never makes up more than a 10-15% of the population (Figure 2b).

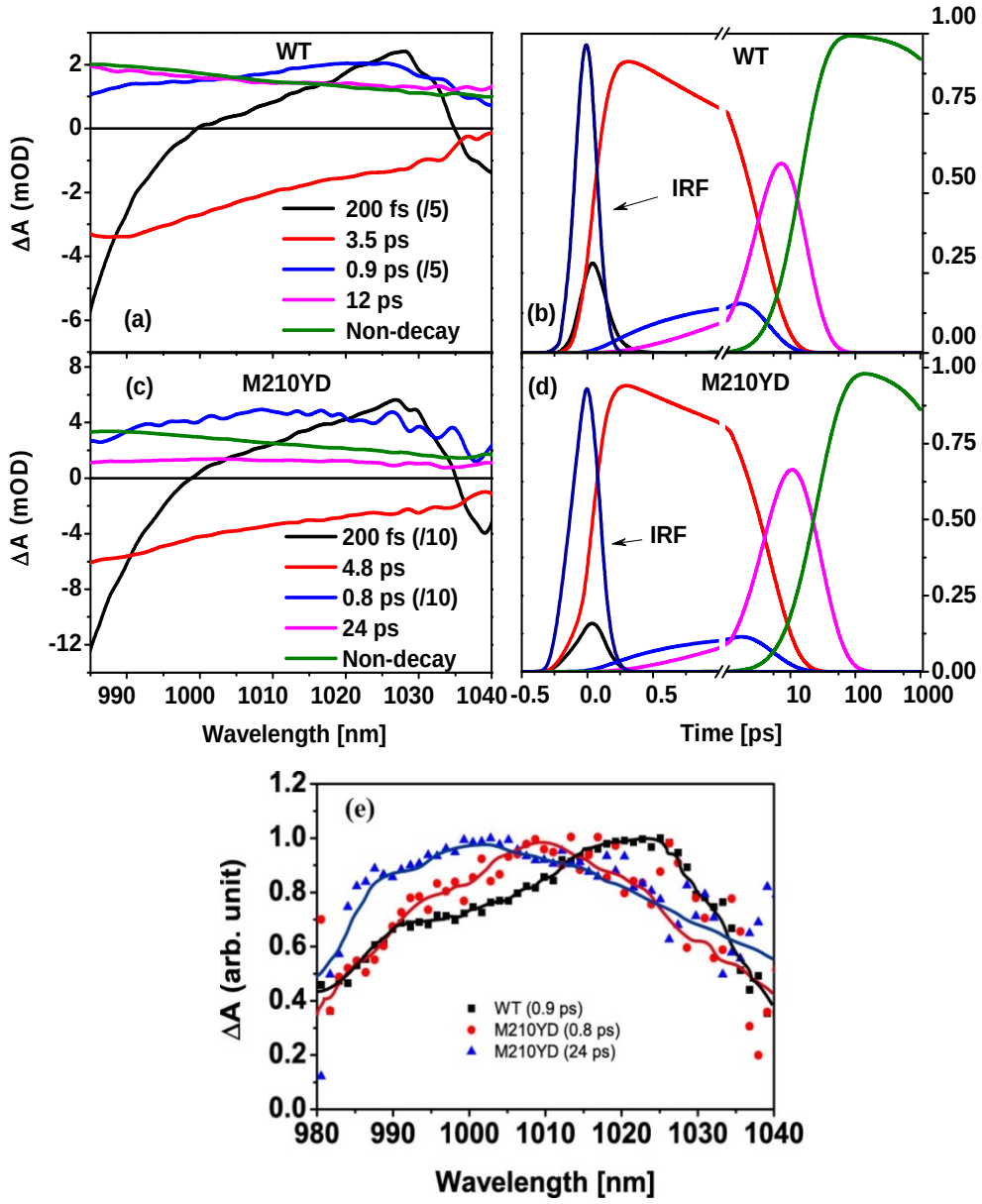

Figure 2 Left panels, graph a, c): EADS from a global analysis using a sequential model in the 980~1040 nm region upon 860 nm excitation of the wild type and M210YD RC (both in pH=8.0 Tris/Hcl buffer) in a 1 ns time windows. Right Panels, graph b, d): The normalized population evolution with time of each species assumed in the sequential model. For clarity, the amplitudes of the EADS for the 200 fs and 0.9 ps (0.8 ps for M210YD) states are divided by 5 (10 in M210YD). e) EADS associated with the $P^{+}B_{A}^{-}$ state normalized to their maxima, showing. a dynamic band blue shift in the M210YD RC (0.8 ps and 24 ps states) in relative to that of the wild type RC (0.9 ps state), and as a function of time.

When this analysis is applied to the M210YD mutant (the results for the other M210 mutants described here are available in supporting information Fig-1), the progression of states that results is similar to wild type with two of important differences (Figures 2c and 2d). First, the B_A^- absorption peak is blue-shifted in the M210YD mutant relative to the wild type on the 0.8 – 0.9 ps time scale (Figure 2e shows the normalized spectral changes for comparison). More importantly, this blue shift continues until in the spectral species with a 24 ps lifetime, it is 15~20 nm shifted relative to the 1025 nm peak found in wild type at early times. Second, the 12 ps lifetime spectral species in wild type shows essentially no $P^+B_A^-$ contribution. This EADS is flat and presumably due to broad P^+ absorption. This is because on this time frame the electron in wild type is localized almost entirely on H_A. In M210YD reaction centers, however, the 24 ps spectral species still appears to contain a B_A^- signal that is about one fifth of the amplitude it was in the 0.8 ps EADS (the spectra in figure 2e are normalized). Equally importantly, while this B_A^--containing signal decays in 24 ps, the H_A^- signal lives much longer. Apparently, there is a substantial amount of $P^+B_A^-$ in equilibrium with $P^+H_A^-$ on the picosecond time scale, but with a 24 ps time constant, the equilibrium shifts towards $P^+H_A^-$. This is consistent with the fact that the fast recombination process disappears on a similar time scale.

Taken together, the time dependent shift in the B_A^- band on the picoseconds time scale in the M210YD mutant, and the fact that it remains in the 24 ps lifetime spectral species but this decays much faster than H_A^- does, suggests a model for the unusual behavior of this mutant. The early time shift of B_A^- could represent a

relaxation in the dielectric environment around B_A on the time scale of initial electron transfer. This relaxation occurs predominantly after the electron has transferred to H_A and pushes the free energy of $P^+B_A^-$ down close to that of $P^+H_A^-$. This dielectric relaxation is evidenced by the blue shift in the B_A^- absorbance band. This is consistent with the fact that initial electron transfer is kinetically similar in the mutant and wild type; on the picoseconds time scale $P^+B_A^-$ has not yet relaxed completely so forward electron transfer proceeds normally. After $P^+B_A^-$ has relaxed, charge recombination can proceed very rapidly until the equilibration between $P^+B_A^-$ and $P^+H_A^-$ shifts towards $P^+H_A^-$ on the 24 ps time scale, presumably due to dielectric relaxation in the environment around $P^+H_A^-$.

The slow component of the H_A^- to Q_A electron transfer

As described above, the kinetics of H_A^- disappearance in M210YD reaction centers is biphasic, containing both a component near 200 ps, similar to wild type, and a long component with a lifetime of about ¾ of a nanosecond. The underlying heterogeneity could either be static (multiple ground state conformations of the reaction center) or dynamic. Interestingly, other mutations at this position do not result in much change in the rate of transfer to the quinone, suggesting that the coupling is not very sensitive to the exact structure in this region. Given the nature of the M210YD mutation and the other apparent effects on dielectric relaxation, it is more likely that the heterogeneous kinetics results from either static or dynamic heterogeneity in the driving force of the forward electron transfer. One can estimate the size of the change in driving force that

would be required to give rise to this magnitude of rate change by looking at the rather extensive literature on quinone replacements[191]. From this, it appears that shifting the rate from 200 to 700-800 ps is equivalent to a decrease of the driving force by at least 100 meV.

Figure 3 presents the decay associated spectra from a global analysis of the transient absorption spectra of M210YD reaction center in 510~750 nm spectral region using four exponentials plus one constant. In addition to a spectral feature of the ground state bleaching recovery of P at 600 nm at 26 ps, representing the early charge recombination from $P^+H_A^-$ in this mutant, another noteworthy feature is seen in the decay associated spectra of the 180 ps and 720 ps components. A 4~5 nm red shift is observed in the ground state bleaching recovery of the bacteriopheophytin band on the 720 ps timescale compared to the decay associated spectrum of the 180 ps component. In the meantime, there appears to be a corresponding blue shift of the anion band (around 660 nm) of H_A, though this is more difficult to see due to the breadth of the band. Thus, there are two spectrally distinct $P^+H_A^-$ states involved on the different time scales. A spectral band shift of this nature is consistent with two distinct dielectric environments of $P^+H_A^-$ giving rise to two driving forces for forward electron transfer.

One cannot directly determine from this if the dielectric environments are static environments present in the ground state or result from dielectric relaxation on the time scales being considered. In either case, the nature of the mutation involved (Y → D) and the fact that other mutations at the same position

do not show this kinetic complexity suggest that the protonation state of the aspartic acid could play a role in the unusual kinetic properties of the M210YD mutant.

pH dependence of electron transfer in wild type and M210YD RCs

As shown in Table 3 (the kinetic curves are in supplementary information, Fig S-1), there is a moderate pH dependence of the fast charge recombination time constant in M210YD reaction centers (it slows down by a factor of two) and an even less dramatic dependence of the biphasic time course of H_A^- to Q_A electron transfer on pH. Wild type also shows weak pH dependence for the electron transfer rate to the quinone. Thus, while pH may perturb the aspartic acid and its environment, there does not appear to be a static protonation or deprotonation in this pH range. This argues that the protonation state of the aspartic acid is not substantially heterogeneous, at least in the ground state (the effective pKa is probably not close to 8.0). In other words, the kinetic heterogeneity in the H_A^- to Q_A electron transfer reaction in M210YD is not due to a static heterogeneity in the protonation of the aspartic acid in the ground state. This conclusion is also supported by the ground state absorption spectrum of this mutant (Supplementary Information-Fig-S3), which does not show any apparent pH dependence.

Table 3 Time constants and their relative amplitudes yielded by performing multiple-exponential fits on the kinetics decays in **Figure 3**.

Sample (Q_A-removed)	pH	τ1 (%)	τ2 (%)	τ3 (%)	τ4 (%)	% of Non-decay
wild type	8.0			390 ps (11.7%)	6 ns (45.7%)	42.6%
wild type	9.5			366 ps (8.2%)	6 ns (31.2%)	60.6%
M210YD	8.0	2.53 ps (2.2%)	21.6 ps (12%)	456 ps (16.2%)	5.7 ns (46.1%)	23.5%
M210YD	9.5	1.82 ps (4.4%)	44.5 ps (15%)	640 ps (9.6%)	6 ns (47.9%)	23.1%

The weak pH dependence suggests that neither the pKa value of the tyrosine in the wild type reaction center nor that of the aspartic acid in M210YD falls in current investigated pH range (8.0~9.5). However, one remaining question is: To the high pH end or to the low pH end? Particularly for M210YD, its protonation state could be important to explain the observed fast charge recombination and the biphasic $P^+H_A^- \rightarrow P^+Q_A^-$ electron transfer. The intrinsic pKa value of the Asp amino acid in solution is around 3.9. Its pKa value can shift in a heterogeneous protein environment due to the interactions with other ionizable groups in its neighborhood, or in the other extreme, deprived of such interactions because of the absence. Despite of this uncertainty, there is a much larger possibility that the aspartic acid is de-protonated, because among the statistical data of experimentally determined the pKa states of embedded Asp side chain in more than 500 folded proteins, very few of them move to the high pH tail (9~10)[192]. A structure based calculation using MCCE[172, 173] (details in Methods section) and an

online server based on empirical pKa prediction (PROPKA 3.1 server[193, 194], http://propka.ki.ku.dk) also prefer a de-protonated state for the Asp residue in M210YD at pH 8.0~9.5 (pKa = 6 ~ 7, see **Table** 4), particularly if one expects an increase in dielectric constant in the local environment of the mutation due to increased conformational flexibility[102]. Furthermore, this explanation is also consistent with the observation of the blue shift of B_A^- absorption band in the M210YD mutant at pH=8.0 upon charge separation because the redistribution/relaxation of the localized net charges in the de-protonated Asp side chain can lead to a major relaxation of B_A^- energy level.

Table 4 Calculated pKa value for the M210 site tyrosine sidechain in wild type RC and aspartic acid sidechain in the M210YD mutant. The values in brackets are calculated by PROPKA 3.1 server, and other values are calculated by MCCE program. The ε_{prot} value represents the protein dielectric constant chosen for the continuum electrostatic calculations.

	wild type RC (ε_{prot}=4.0)	M210YD RC (ε_{prot}=4.0)	M210YD RC (ε_{prot}=8.0)
Neutral state	(14.7) 14	(10.1) 9.36	(7.4) 6.33
$P^+H_A^-$ state	>14	9.45	6.00

Charge recombination in Q_A-depleted M210YD reaction centers

When Q_A is removed in wild type RCs, $P^+H_A^-$ is formed and decays non-exponentially due to charge recombination[26, 168, 180, 184], primarily on the 6-10 ns time scale. Charge recombination in Q_A-depleted M210YD RCs is kinetically even more complex, with time constants on at least three time scales (22~44 ps, 456~640 ps, and >5 ns). More than 25% of the RC population recombined on a sub-nanosecond time scale in M210YD, compared to only about 10% in wild type

and none of the decay components in wild type have sub-hundred picosecond time constants. At least in terms of the fast recombination reaction in M210YD, these results are consistent with those presented above for Q_A-containing reaction centers in which the 24 ps component was interpreted as rapid charge recombination.

A model for electron transfer, dielectric relaxation and recombination in M210YD RCs

Figure 4b provides a scheme that summarizes some of the concepts and conclusions described above for the M210YD mutant reaction centers. Following primary charge separation, the energy level of $P^+B_A^-$ experiences a rapid relaxation. This is observed as a fast dielectric relaxation in the environment of B_A^- (**Figure 2e).** As a result, the free energies of $P^+B_A^-$ and $P^+H_A^-$ are now very similar, a fact that is reflected in the apparent equilibrium population of B_A^- that persists well after initial electron transfer (Figure 2). This provides a pathway for recombination of $P^+H_A^-$ via $P^+B_A^-$ that is now fast enough to compete with the relaxation of $P^+H_A^-$ relative to $P^+B_A^-$ on the 20 ps (pH 8.0) or 40 ps (pH 9.5) time scale. Given that about 10% of the $P^+H_A^-$ population recombines with this time constant (Table 3), the intrinsic recombination rate constant during this time period should be a few hundred ps. Relaxation of $P^+H_A^-$ has been widely documented in literature[27, 184, 186, 195], on a variety of time scales (from 20 ps to a couple of nanoseconds). After $P^+H_A^-$ relaxes, access to recombination via $P^+B_A^-$

has a much higher activation energy and thus the rate recombination slows down to values more similar to that observed in wild type.

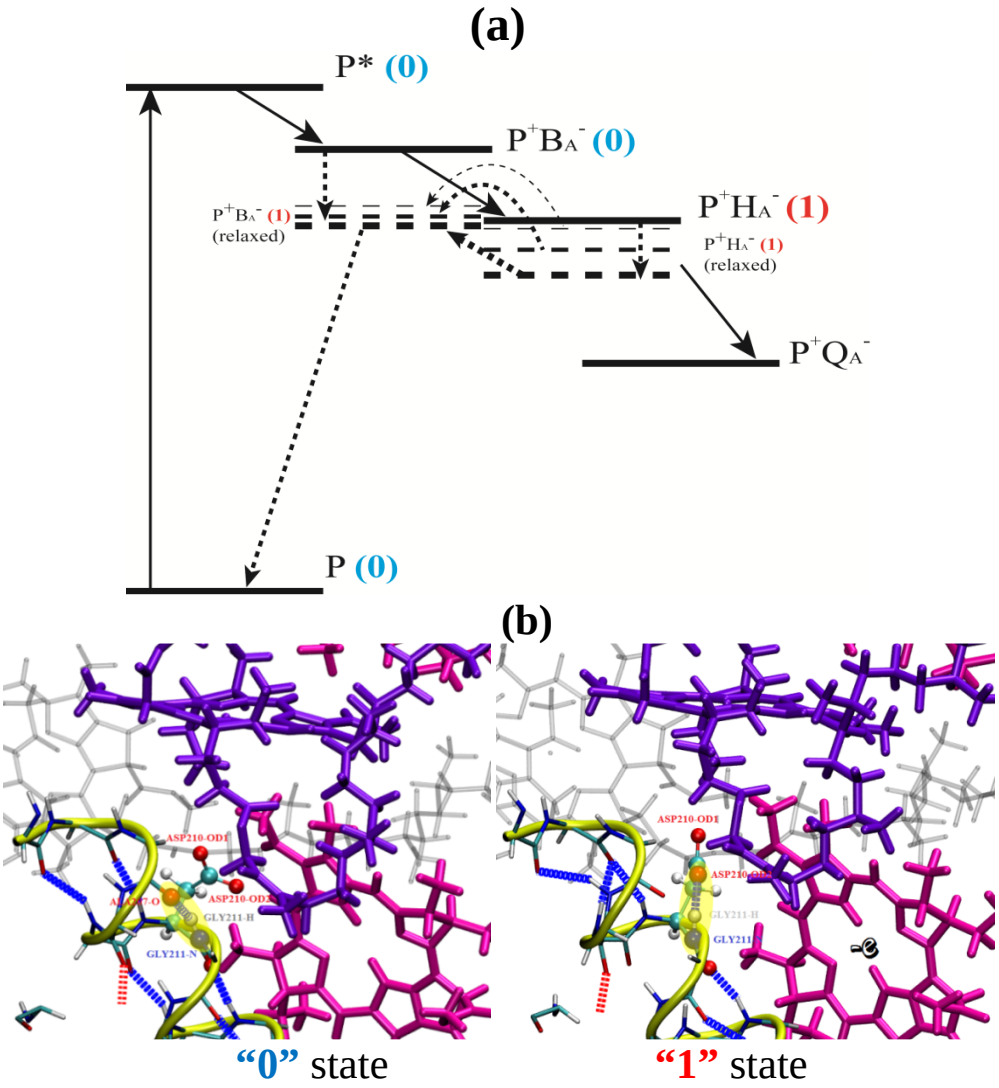

Figure 3. (a): Energetics scheme for primary charge separation and the charge recombination pathway. The energy level relaxation caused by the dielectric environment change (labels for "0" and "1" states are reserved for figure b), resulting in a branched recombination pathway as well as a biphasic rate to Q_A. **(**b): Possible structural picture of the dielectric environment change due to fast hydrogen bonding dynamics. Before charge separation, the alpha-helix backbone hydrogen bonding Ala207-Gly211 was intact ("0" state); After charge separation, to avoid the unfavorable charge-charge interaction between Asp210 and H_A^-(pink color), the Asp210(OD2) lone pair competes the hydrogen bonding with Gly211, forming Asp210-Gly211 hydrogen bond ("1" state).

The introduction of aspartic acid at M210 clearly elicits a change to the dielectric environment that is not seen in wild type or other mutants at this site. In terms of electron transfer, this is expressed both as a fast charge recombination of $P^+H_A^-$ $\rightarrow PH_A$ and a biphasic $P^+H_A^- \rightarrow P^+Q_A^-$ electron transfer. Even though the possibility of a static heterogeneity in the protonation of the aspartic acid in the ground state cannot be entirely excluded, the weak pH dependence of both the ground state spectrum and the electron transfer kinetics suggests a different explanation. Such a perturbation to the dielectric environment more likely has a dynamic origin, in which the protonation state (or at least the polarity) of the aspartic acid changes during charge separation as does its interactions with other amino acid groups in the protein.

Exactly how and when protonation/de-protonation of the aspartic acid takes place in M210YD is not certain, but one possibility is that this occurs during the fast $P^+B_A^-$ energy level relaxation following primary charge separation. One structurally plausible scenario is that immediately after charge separation, the aspartic acid protonates and forms a new hydrogen bond with the backbone nitrogen of glycine M211 (Asp210(OD2)-Gly211(HN)) while simultaneously breaking an alpha-helical backbone hydrogen bond between M211 and M207 (Ala207(O)-Gly211(HN)) (see figure 4a) . This will remove the unfavorable charge-charge interaction with the bacteriopheophytin anion (H_A^-) and allow fast dielectric relaxation.

Supporting Information

Figure S1-S3 provide additional spectroscopic data for the ground state spectrum and pH dependent data.

Supplemental Data

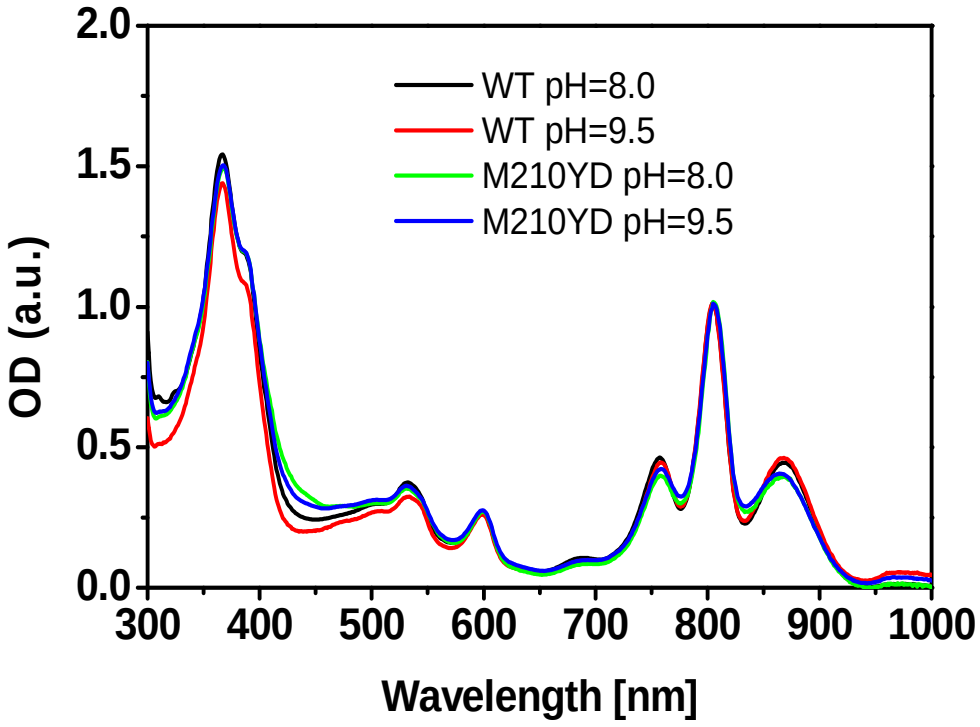

Figure S1: Superimposed ground state absorption spectra of wild type (pH=8.0, 9.5) and M210YD (pH=8.0, 9.5). The peaks were normalized at 800 nm.

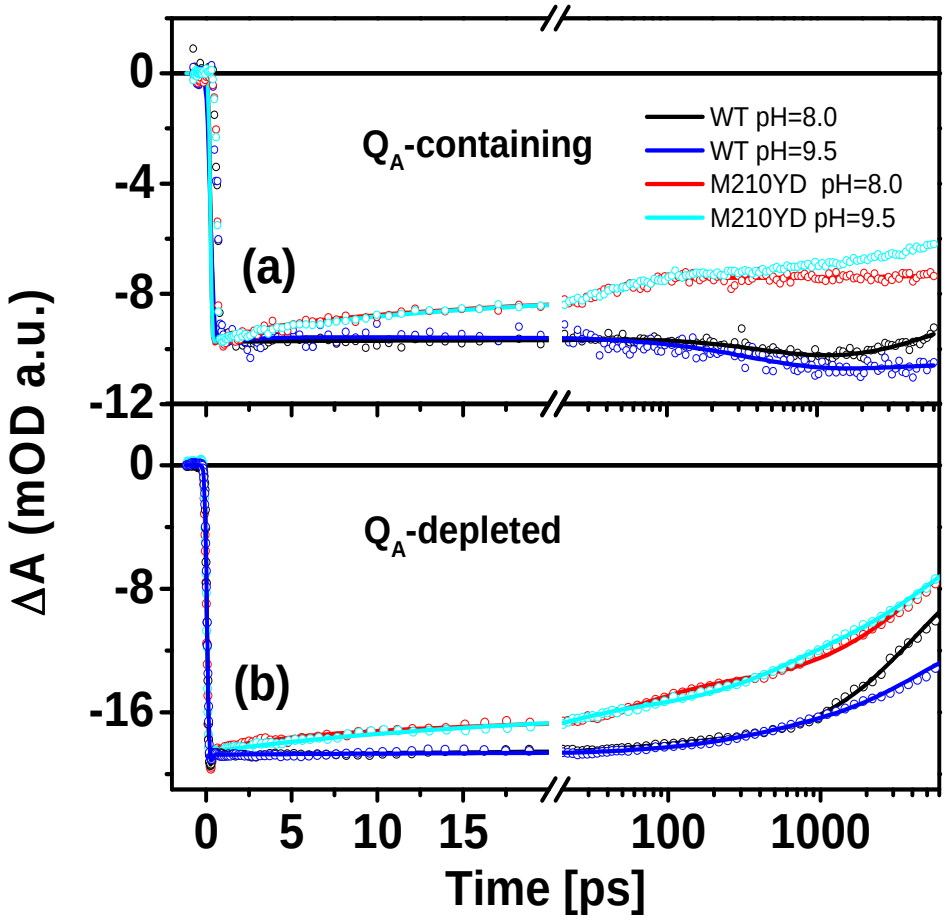

Figure S2: The ground state bleaching recovery kinetics of P for wild type RC and its M210YD mutant in their Q_A-containing (a) or Q_A-depleted state (b), measured in two different pH conditions (8.0 and 9.5), and observed at 835~840 nm in a 6 ns probe window. The kinetics of all measurements were normalized to the maxima of the initial bleaching. Up to four exponential components plus one non-decay component was used to fit the curves (solid lines).

CHAPTER 4

Utilizing the dynamic stark effect as a probe for the reaction center dielectric relaxation during charge separation

Abstract

The electrochromic shift is a phenonmenon in which the absorption spectrum of a molecule shifts in response to an external field. In the photosynthetic reaction center, this field is created by charge separation following excitation by light. In Stark effect theory, a shift in the absorption spectrum is considered as a component of the field-induced energy level perturbation in both the ground state and excited state. In other words, the Stark shift indirectly reflects the effective field strength on the probe molecules. In this work, the possibility of monitoring the continous variation of the effective field strength on the ground state absorbance spectrum of the monomeric bacteriochlorophylls in the photosynthetic reaction centers has been explored by observing their time dependent Stark shift during charge separation (dynamic Stark shift). The time dependent Stark shift is analyzed by first performing a sequential analysis of the time-resolved spectra to obtain the evolution associated difference spectra (EADS), then reconstructing the "post-excitation" abosolute absorption spectra from those EADS, and finally forcing the reconstructed spectra to converge in a three-gaussian component global fit. Using this approach, the dynamic Stark shift has been explored in wild type reaction centers and in four of mutants at position M210. It is shown that the dynamic Stark shift of both monomeric bacteriochlorophylls are consistent with

our current picture of electron transfer. That said, it is also shown that the dynamic Stark shift conveys additional information not available in the electron transfer kinetics. In particular, polarization effects influenced near B_A can be observed which lend in insight into the role of protein dynamics in photosynthetic electron transfer.

Introduction

The electronic Stark effect in molecules has been known for a long time and utilized to explain the effects of electric fields on molecular electronic transitions. On advantage that monitorin the Stark effect has over many other experimental approaches is that it has the potential of allowing a direct comparison between results from electrostatics calculation/simulation and those from experiments. For each molecule, the perturbed transition dipole $\vec{p}$ and the peak position ν_{max} are functions of the external field $\vec{E}$:

$$\overrightarrow{p(E)} = \overrightarrow{p_0} + A \cdot \vec{E} \qquad (47)$$

$$\Delta\nu(\vec{E}) = -\overrightarrow{\Delta\mu} \cdot \vec{E} - \frac{1}{2}\vec{E} \cdot \Delta\alpha \cdot \vec{E} \qquad (48)$$

Where $A$is the transition polarizability, $\overrightarrow{\Delta\mu}$and $\Delta\alpha$ are the difference permanent dipole moment (between ground state and excited state) and the difference polarizability, respectively. The absorption spectrum can therefore be expanded as a Taylor series in powers of $\Delta\nu$, i.e.

$$\varepsilon(\nu, E) = \varepsilon(\nu,0) + \frac{\partial\varepsilon(\nu,0)}{\partial\nu}\Delta\nu + \frac{1}{2}\frac{\partial^2\varepsilon(\nu,0)}{\partial\nu^2}\left|\Delta\nu\right|^2 + \Lambda$$

$$= \varepsilon(\nu,0) - \frac{\partial\varepsilon(\nu,0)}{\partial\nu}\left(E_{ext}\cdot\Delta\mu + \left|E_{ext}\right|^2\Delta\alpha\right)h^{-1}$$

$$+ \frac{1}{2}\frac{\partial^2\varepsilon(\nu,0)}{\partial\nu^2}\left(E_{ext}\cdot\Delta\mu + \left|E_{ext}\right|^2\Delta\alpha\right)^2 h^{-2} + \Lambda\ ,$$

$$\varepsilon(\nu, E) - \varepsilon(\nu,0) = -\left(\frac{\partial\varepsilon(\nu,0)}{\partial\nu}\right)\frac{E_{ext}\cdot\Delta\mu}{h} - \left(\frac{\partial\varepsilon(\nu,0)}{\partial\nu}\right)\frac{\Delta\alpha\left|E_{ext}\right|^2}{h} + \frac{1}{2}\left(\frac{\partial^2\varepsilon(\nu,0)}{\partial\nu^2}\right)\frac{\left|\Delta\mu\right|^2\left|E_{ext}\right|^2}{h^2} + \Lambda \qquad (49)$$

Liptay first developed a detailed framework for describing the electronic Stark effect for molecules immobilized in a matrix[196, 197]. Even with this simlification, the expressions in equation (49) would be even more complex if the perturbations of the external field on the transition dipole and the transition polarizability in expression (47) were considered. Luckily, due to molecular symmetry, the effects of the external field on the transition dipole change are often relatively minor compared with the influences of the permanent dipole change in most case[198]. Equation (49) is suffice for molecules that are pre-aligned in a polymer film or a membrane. However, in isotropic samples where molecules are entirely random relative to the field, equation (49) need to be further averaged over all orientations (odd terms associated with $E_{ext}\cdot\Delta\mu$ disappear, leaving only even terms), resultin a broadening or narrowing of the functional form, rather than a shift, assuming the dipolar approximation (ignoring the $\left|E_{ext}\right|^2\cdot\Delta\alpha$ term). This is depicted in figure 1,

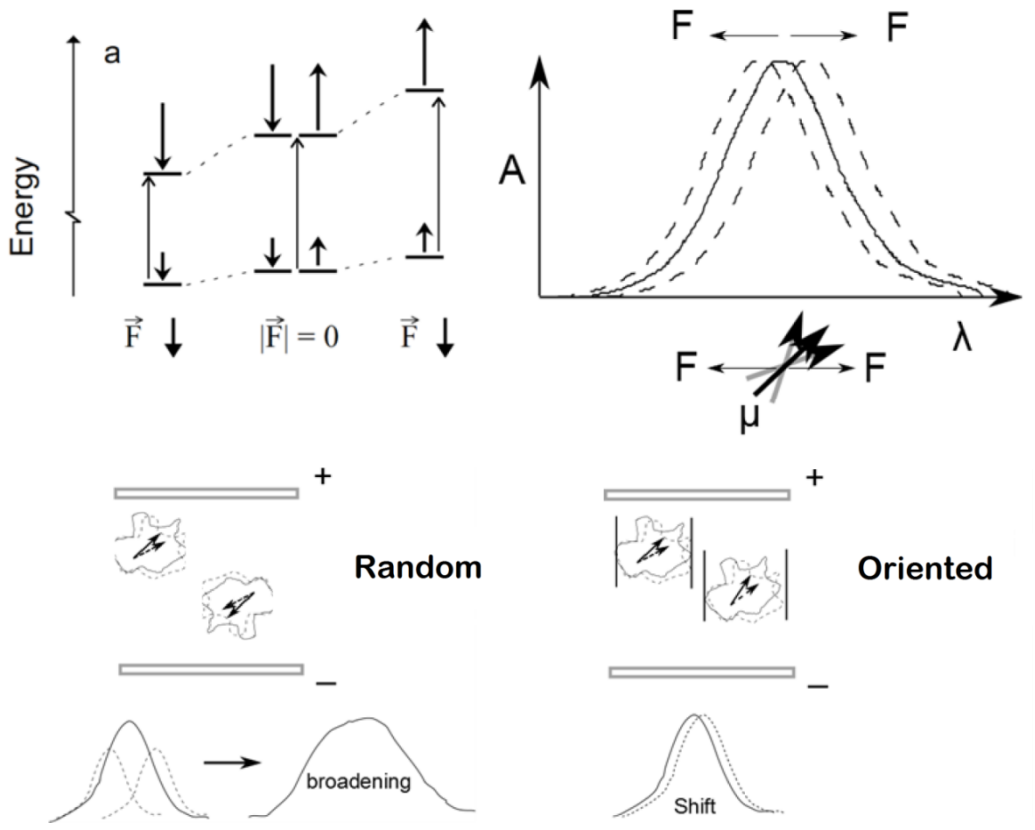

Figure 1: An illustration of the Stark effect in molecules. (a) energy level in an external field (b) spectral band shift for a single molecule (c) spectral band broadening effect of the molecules in random medium (d) spectral band shift in molecules oriented in the film

For molecules with homogeneous orientation, the field perturbation to an individual transition resulting in a collective shift in one direction become more important than the spectral line shape. In contrast, for non-oriented molecules, the perturbation felt by the transition dipoles is non-uniform, and broadening effects dominate in the line shape. Both experimental and theoretical application of the Stark experiment in biomolecules and organic molecules system has progressed rapidly during recent years[198-207]. The electrochromic shift, a phenomenon that has

been know for many years, is a particular example of the Stark shift observed in absorption spectra[208-210]. The electrochromic effect in reaction centers was observed early on and explained by a shift of the absorption peak of the chromophores in the charge separated state[211]. The field created by an internal charge separation within the reaction center is identical for each molecule in the sample, therefore equivalent to the prealigned case mentioned before. Some early efforts were devoted to studying the electrochromic shift within the reaction center ground state spectra using low temperature, where a high signal-to-noise ratio was possible[103]. However, there are not many reports that consider the role of the Stark effect in time-resolved absorption spectra context. In this study, it is shown that the electrochromic shift can be used to characterize time-dependent protein dielectric relaxation.

Materials and Methods

Mutant preparation and reaction center protein isolation

The mutants used in this chapter all target one site, position 210 in the M branch (M210). The construction of the mutant that incorporates a poly his-tag modified pseudo wild type *Rb. sphaeroides* reaction center gene has been described in Chapter 3 and previous publications[169, 171]. The reaction center isolation and purification was also performed as previously described[170]. The reaction center samples were suspended in 50 mM Tris-HCl buffer (pH 8.0), 0.025% LDAO detergent, 1mM EDTA during measurements.

Spectroscopy measurement

A femtosecond pump probe system used to investigate the transient absorption of the reaction center samples is described in Chapter 3. In brief, the laser pulses were generated at a reptition rate of 1KHz with 130 fs duration at 800 nm using a regenerative amplifier system based on a Titanium:Sapphire laser (Millennia, Tsunami, Spitfire, Spectra-Physics lasers). About 70% of the beam power was used to pump the infrared optical paramagnetic amplifier (OPA-800C, Spectra-Physics), and the remaining 30% was used to generate the white light continnum for probe. The 860 nm excitation was obtained by fourth-harmonic generation in the OPA. The white light probe beam was generated by focusing the 800 nm pulse onto a 3 mm sapphire plate followed by pulse compression using a pair of prisms (CVI). The polarization of the excitation beam and the probe beam were set to a magic angle (54.7º) with respect to each other. The probe light was dispersed by a spectrograph and detected by a CCD device over a 300 nm spectral range (centering at 830 nm, 680-980 nm). Samples were placed between two quartz plates sealed in a wheel (1.2 mm path length) that rotates to avoid accumulating the $P^{+}Q_{A}^{-}$ state. The translation stage using in the delay line for the kinetics measurements allows up to a 6 ns delay to be introduced between the pump beam and the probe beam.

Data analysis

The spectroscopic analysis is divided into two parts. First, a rudiment analysis is performed that uses conventional curve fitting composed of several exponentials

or global analysis on the whole spectra using a kinetic model involving a series of sequential states. Second, a further dynamic Stark shift analysis that utilized both time resolved difference spectra and the ground state spectrum to reconstruct the absorption spectrum at a particular time after light excitation is performed (referred to as a time-resolved absolute spectrum). Instead of using all the time resolved difference spectra directly, the evolution associated difference spectra (EADS) from the sequential model analysis is used for the time-resolved absolute spectra reconstruction. The purpose of this replacement is simply to reduce the spectral noise in the subsequent fitting of the absorption bands and to avoid cumulative errors by reducing the amount of fitting data. Since the sequential model analysis is simply used to filter out the noise, in principal the number of states used for such a fitting should be large enough to result in a random distribution of residuals. In practice, at least 7 states are required to fit the time resolved spectrum in the Q_y spectral region. Judging from the kinetics and the spectral features of the EADS states, the first two states are assumed to be dominated by the excited state P* population. All the following states can be treated as time dependent mixtures of charge separated states. The dynamic Stark shift analysis is applied to the charge separated state EADS.

The dynamic Stark shift method

The reconstruction of time resolved absolute spectra is similar to the steady state approach in Steffen et al's work[103]. The only difference is to replace the

$P^+Q_A^-$ – PQ_A steady state difference spectra with the charge separated state EADS calculated in the previous step. Briefly, the absorption bands of the accessory bacteriochlorophylls (B_A and B_B) are built-in probes of the internal electric field produced by the charge separated states(either $P^+H_A^-$ or $P^+Q_A^-$ in this case). In order to obtain the absolute absorption spectrum of reaction centers in the charge separated state, the magnitude of the P ground state absorption band was scaled to match the maximum of the absorbance decrease associated with P ground state bleaching in the EADS, and then the ground state and normalized transient spectrum are added together (figure 2).

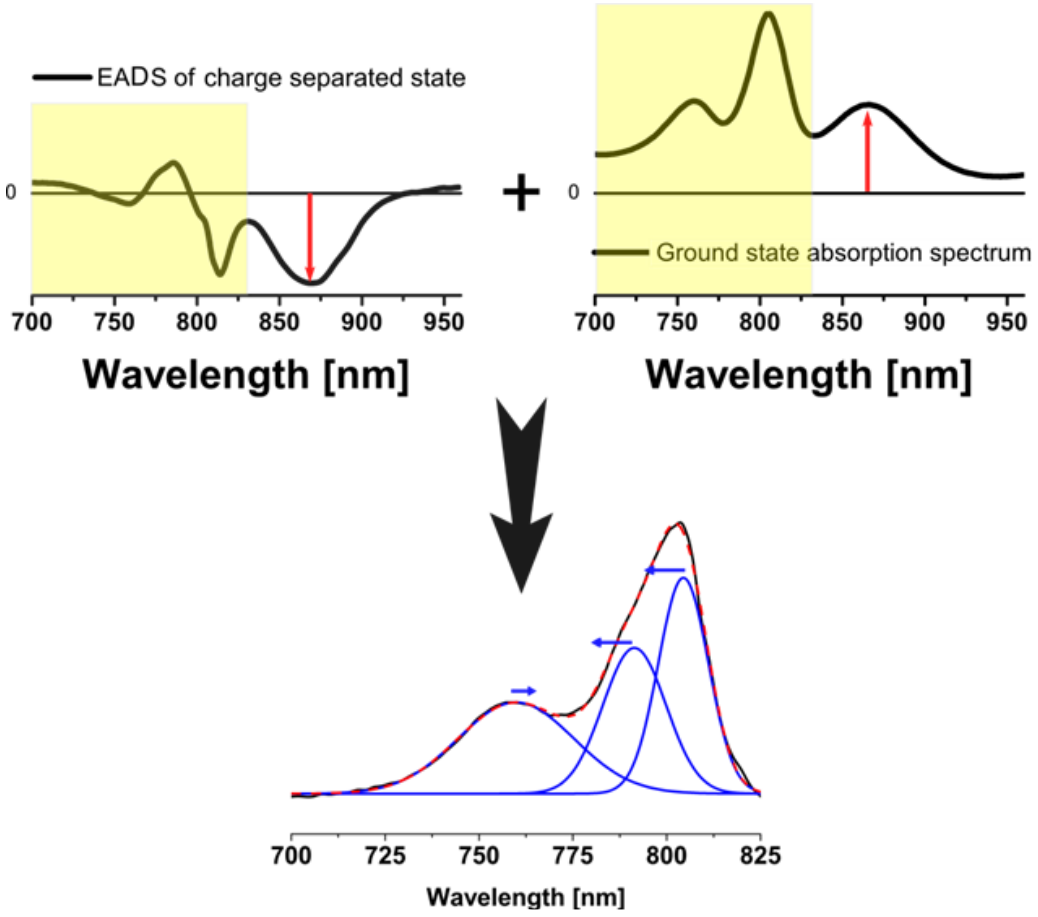

Figure 2: Illustration of how reconstruction is performed of a band-shifted time resolved absolute spectrum (absorption spectrum with background illumination) from the ground state absorption spectrum and the difference absorption spectrum by a superposition procedure. After the addition of two spectra, only the spectral region in yellow will have significant contribution to the absolute absorption spectrum as the two spectra are first normalized at 865 nm (P band) before the addition. The absolute absorption spectrum is then fitted with three gaussian bands to yield the Stark shift (blue arrows, detailed in text).

The absolute absorption spectra are assumed to contain the absorption band information of B_A, B_B, H_A and H_B only. Even though previous theoretical calculations as well as some hole burning results have suggested the existence of an upper exonic band of P* (P_+) in the absorption region of accessory bacteriochlorophyll, its oscillator strength is assumed to be much smaller than B_A and B_B from recent experiments[212]. More important, we only consider the charge separated state EADS in current study to minimize the complexity that arises from the absorbance change due to the excited state. For each time-resolved absolute asborption spectrum constructed from one EADS, B_A and B_B band shifts ($\Delta\nu_{B_A}$, $\Delta\nu_{B_B}$) need to be extracted. As in ref [103], gaussian fits are the most convenient way to perform this step. However, in contrast to the strategy used in the previous paper, only a single gaussian function is used to fit each of the B_A and B_B absorption bands rather than using two gaussian bands to describe each cofactor. This is because at room temperatuer (the current study), there is a significant line shape broadening compared with the low temperature condition (1.5 K) used in the previous work. This make it easier to describe the bands with a single gaussian. Reference [103] also considers room temperature data. In that case,

only an average spectral shift can be identified for the bacteriopheophytin band in their work. The bacteriochlorophyll band shift studied here has the advantage of being larger than that of the bacteriopheophytin and the contributions from each cofactor are more separable. An even more important aspect is that, the time-resolved spectra provide a continuous variation of the band shift that significant increases the amount of information that goes into the spectral determination, reducing the uncertainty relative to what one would get from single spectral fit. The absorption bands of the bacteriopheophytins (H_A and H_B) are even more coarse-grained in fitting. Only one gaussian is used to represent the absorption bands of both H_A and H_B cofactors to ensure a robust fitting of B_A and B_B bands, even though this usually results in a non-random fitting residual for H_A and H_B bands. Therefore, a global gaussian peak fit on a series of EADS is analogous to the global analysis on the time resolved spectra. The constrained parameters for the global gaussian fit is the widths of the gaussian absorption bands, which are kept constant throughout the fit. The reason for applying such a constraint is indicated in Figure 1. The chromophores in the reaction center protein are embedded in the protein matrix with well-defined positions and orientations, which basically eliminates the source of heterogeneity between reaction centers. Given a well-defined internal field (though it changes with time, it varies in the same way collectively within the ensemble) and probe chromophore dipole orientations, the dynamic change of the Stark shift value reflects the internal dielectric relaxation of the protein. In practice, the time

dependence of B_A (or B_B) band shift $\Delta\nu(t)$ is calculated by weighting the values in each EADS with normalized populations in the corresponding kinetics:

$$\Delta\nu(t) = \sum_i C_i(t) \cdot \Delta\nu_i^{EADS}(t) \qquad (50)$$

Results and discussion

The magnitude of the evolution of the stark shift from B_A and B_B absorption bands are presented as a function of time in figure 3 for the wild type reaction center and its M210 mutants.

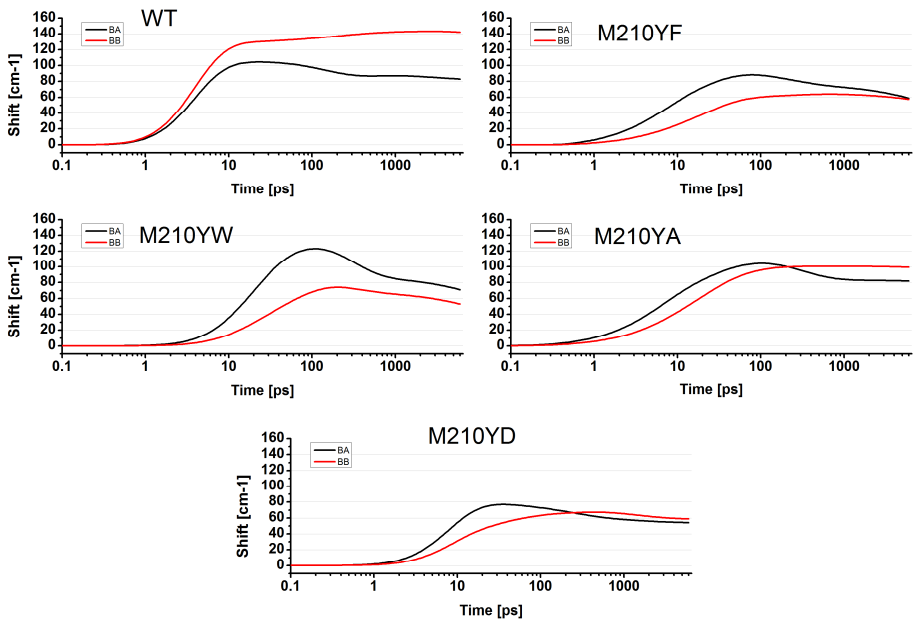

Figure 3: B_A and B_B band shift kinetics for wild type and M210 mutants. Black lines represents B_A and red lines represent B_B. The kinetics are constructed by the procedure described in the Methods section.

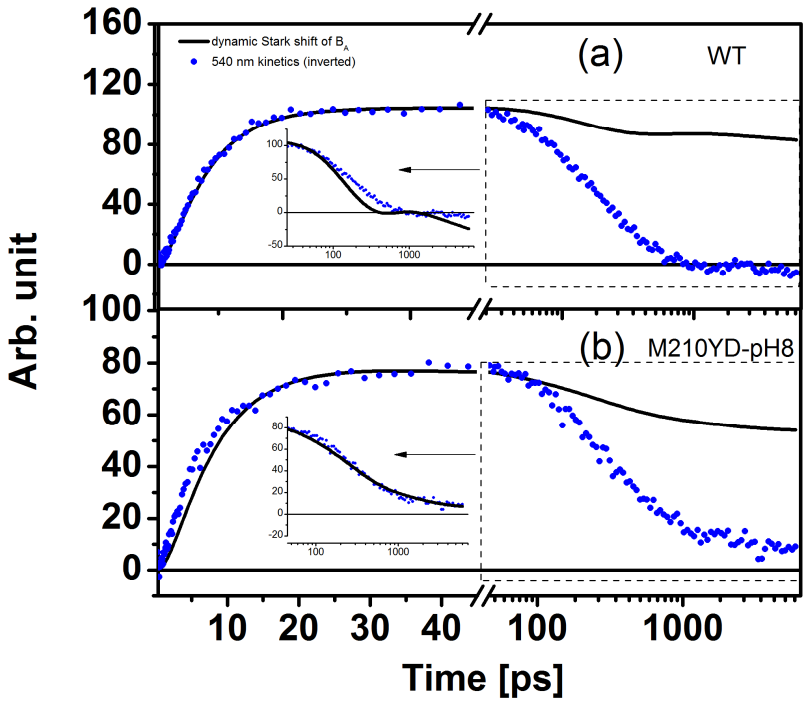

Figure 4: Comparing the time dependent B_A Stark shift (black) with the electron transfer kinetics measured at 545 nm (blue, monitoring the bleaching signal of H_A) over a 6-ns time window. Both kinetics are normalized at the maximum, which allows a direct comparision during the peroid of primary electron transfer. To facilitate a comparison on a longer time scale (electron transfer kinetics to quinone and up to 6-ns), the Stark shift kinetics are scaled to overlap with the electron transfer kinetics. Wild type reaction centers (a) and the M210YD mutant (b) are compared measuring at pH 8.0 and room temperature.

In wild type reaction center and all of the mutants considered, the dynamic stark shift for B_A builds up quickly and then decays more slowly. This is because the magnitude of the stark shift basically reflects the interaction intensity of the B_A multi-pole with the internal field due to charge separation. According to equation (52), to the first order approximation (dipole), the stark shift should be proportional to the field strength. Qualitatively, the rise and decay of the field strength do correlate with the distance between B_A and the electron as the charge

separation develops. On the other hand, the stark shift for the B_B absorption band also experiences such a rise, yet at a different rate compared with that of B_A. After reaching the maxima, the B_B stark shift either does not show a significant decay in some of the mutants, or shows a slight decay or even a growth (in wild type) that is independent of electron transfer.

A comparison between the kinetics of the B_A dynamic stark shift and the electron transfer kinetics characterized at 545 nm H_A ground state bleaching was performed for wild type reaction centers and the mutants M210YD. As shown in Figure 4, in the wild type reaction center, the growth rate of the Stark shift during primary charge separation match that of the electron transfer kinetics. If the observed stark shift can be used to represent the time dependence of the effective field strength (first order $\Delta\mu$ approximation), this observation reflects a linear relationship between the effective field strength variation and the electron transfer kinetics. In contrast, the growth of B_A stark shift is occurs more slowly than electron transfer in M210YD reaction centers. This phenomenon might be associated with a significant dielectric relaxation near B_A observed in this mutant (see Chapter 3), where a charge of aspartic acid acting on B_A contributes significantly to its Stark shift and deviates from a linear relationship with respect to a H_A^- population change. In both the wild type reaction center and the M210YD mutant, the kinetic decay of dynamic stark shift during the $H_A \rightarrow Q_A$ electron transfer reaction are faster than the electron transfer kinetics. This is

particularly prominent in the wild type reaction center, where the stark shift decay lifetime is about 130 ps, much shorter than the $H_A \rightarrow Q_A$ electron transfer lifetime. This phenomenon can be explained by the quadratic term in the expression:

$$\Delta\nu = -\left(E_{int} \cdot \Delta\mu + \left|E_{int}\right|^2 \Delta\alpha\right) / h \qquad (52)$$

Using high order stark spectrum, Lao et al. has already showed that the monomeric BChl-*a* has a low excited state polarizability, and the dipole moment change $\Delta\mu$ dominates $\Delta\alpha$ in equation (52)[213]. This linear relationship has been observed in primary electron transfer, which can be treated as an adiabatic process during which the protein dielectric environment is basically the same as the ground state except for changes local to the electron donor P. The deviation observed between the electron transfer kinetics and the Stark shift kinetics in $H_A \rightarrow Q_A$ electron transfer possibly implies that, on this time scale, the higher order term associated with $\Delta\alpha$ is more important. Under these conditions, if the time dependence of the internal field follows the electron transfer (e.g. has a e^{-kt} dependence), a portion of B_A stark shift kinetics should accelerate at a doubled rate due to a quadratic relationship of the field change in the second term of equation (52) (i.e. $\left(e^{-kt}\right)^2 = e^{-2kt}$). One possible explanation for such a phenomenon is that: when the electron transfer arrives at H_A and starts to transfer to Q_A, the entire protein environment starts to relax in response to the charge separation and the environment polarizability near B_A becomes more significant.

Also, if the evolution of $\Delta\alpha(t)$ due to the protein matrix polarization is a complex function rather a constant, the kinetics of $\Delta\nu(t)$ becomes more complicated.

Stark shift observed at $P^+H_A^-$ state and $P^+Q_A^-$ state

A more straight forward way to compare the time dependent dielectric property of the wild type with that of the mutants is to compare the stark shift of B_A and B_B absorption bands in particular electronic states. The maximum of the stark shift in the B_A absorption band can in principle be used as one of gauges of the dielectric response of the reaction center in $P^+H_A^-$ state. The stark shift for the state $P^+Q_A^-$ is determined at the maximum of the delay (6 ns), representing a well formed $P^+Q_A^-$ state after initial relaxation. A summary of the stark shift magnitude of the B_A and B_B absorption bands at two states ($P^+H_A^-$ and $P^+Q_A^-$) in wild type and the mutants is presented in figure 5. Four horizontal lines are drawn representing the values in wild type reaction centers. The mutants are ordered along X axis according to their B_A stark shift magnitude in the $P^+H_A^-$ state. It is not surprising to see that the B_A stark shift magnitudes all decrease by a similar amount, about 20 cm^{-1}, during the transition from $P^+H_A^-$ to $P^+Q_A^-$ (except in M210YW, which is 50~60 cm^{-1}), which is due to an attenuation of the field following the departure of the electron from H_A.

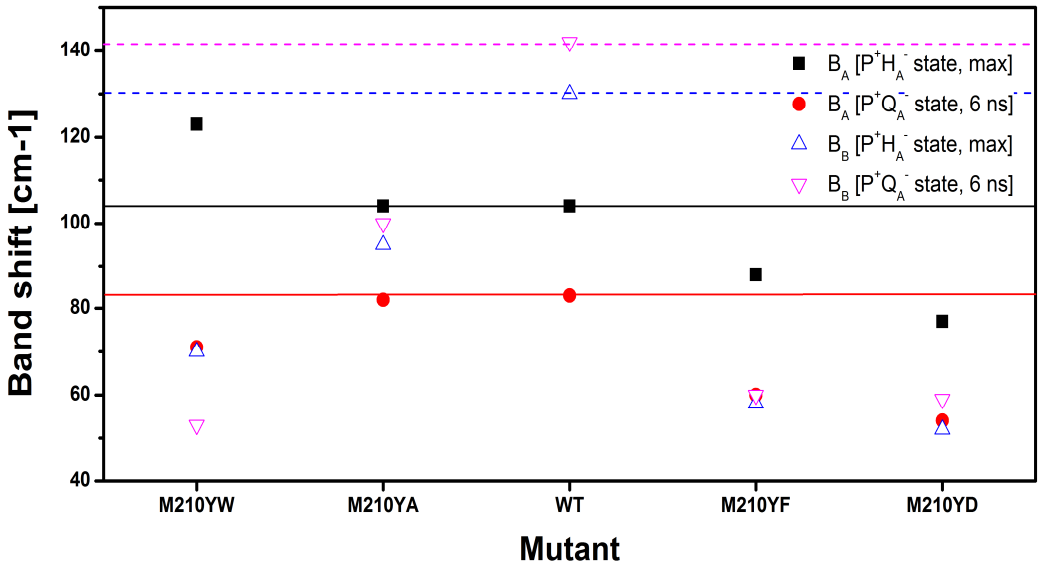

Figure 5: The Stark shift associated two electronic states, $P^{+}H_{A}^{-}$ and $P^{+}Q_{A}^{-}$, in wild type reaction centers and the M210 mutants. The mutant are ordered by the magnitude of B_A Stark shift in the $P^{+}H_{A}^{-}$ state (black square) in descending order. The wild type reaction center values are used as baselines and indicated by lines.

Overall, the change in the B_A stark shift follows electron transfer but does not overlap with its kinetics. In contrast, the stark shift of B_B absorption band exhibits a strong sensitivity to mutagenesis in this site. The idea is that B_B is far from the A-side electron acceptor, and should mostly be influenced by the cation on P, most mutant reaction centers show little evolution in their B_B stark shift kinetics after the primary charge separation. Therefore, the B_B stark shift magnitudes for the two electronic states investigated ($P^{+}H_{A}^{-}$ and $P^{+}Q_{A}^{-}$) are quite similar. Wild type reaction centers are the exception; it appears that there is still significant dielectric environment evolution in P^{+} following the primary charge separation, which appears to enhances the field in the vincinity of B_B. This

observation in the wild type reaction center is surprising, yet its variation trend is approaching the values obtained in previous $P^+Q_A^-$ steady state stark effect experiments which predicted a 175 cm^{-1} Stark shift in B_B [103].

Use dynamic Stark shift approach to predict $B_A \rightarrow H_A$ electron transfer rate within the reaction center mutants

B_A is an electron transfer intermediate between P and H_A. In the wild type reaction center, the $P^+B_A^- \rightarrow P^+H_A^-$ electron transfer takes less than 1 ps to complete, which is faster than its formation (3 ps lifetime for $P^* \rightarrow P^+B_A^-$), resulting a very small observable population. This small $P^+B_A^-$ population can be observed near 1020 nm spectral region due an absorption of B_A^-. The kinetics near 780 nm have also been suggested to provide a measure of the B_A^- population due to the electrochromic shift of its ground state absorption, yet this kind of single wavelength characterization is not very reliable as a result of significant overlap of the spectra of the different cofactors in this region. The building-up kinetics of the B_A stark shift matches with the electron transfer $P^* \rightarrow P^+H_A^-$ kinetics in general, but just like the kinetics observed in the 1020 nm, there is an initially fast phase presumably associated with $B_A \rightarrow H_A$ electron transfer. The rate equation for the $B_A \rightarrow H_A$ electron transfer is written as the following:

$$\frac{dN_{H_A^-(t)}}{dt} = k_{B\rightarrow H} \cdot N_{B_A^-}(t) \qquad (53)$$

where, $N_{H_A^-}$ is the H_A^- population, $N_{B_A^-}$ is the B_A^- population, and $k_{B\to H}$ is the rate constant for $B_A \to H_A$ electron transfer. The $H \to Q$ electron transfer pathway is neglected due to a two order difference in rate constant in competing with $k_{B\to H}$. Assuming that during the kinetics of initial Stark shift of B_A, the field strength felt by B_A is proportional to H_A^- population (first order approximation to $\Delta\mu$), the H_A^- population can then be replaced with the observed magnitude of B_A Stark shift $\Delta\nu_{B_A}$. i.e.

$$\frac{d\Delta\nu_{B_A}(t)}{dt} = k_{B\to H} \cdot N_{B_A^-}(t) \qquad (54)$$

Since the $B_A \to H_A$ electron transfer is fast enough to be considered as an adiabatic process, $k_{B\to H}$ is then taken as a constant. Hence, we have

$$\frac{d\Delta\nu_{B_A}(t)}{dt} \propto N_{B_A^-}(t) \qquad (55)$$

Equation (55) implies that if we compare the derivative of the B_A Stark shift kinetics and the evolution of B_A^- population, they should be similar at least for the rising edge. To validate our approach, we compare the $B_A \to H_A$ electron transfer kinetic measured in 980~1040 nm spectral region and the dynamic Stark shift kinetics analysis in the 800 nm region. The results from both approaches are presented in figure 6.

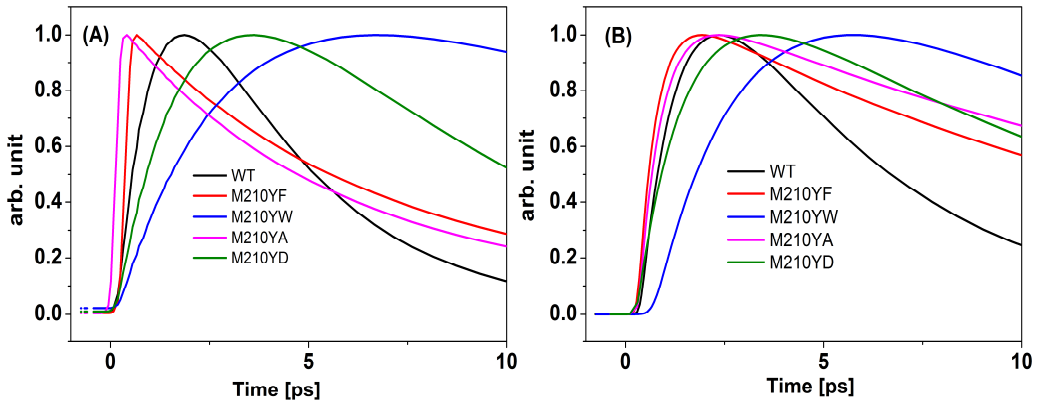

Figure 6: Comparing the kinetics of $\frac{d\Delta\nu_{B_A}(t)}{dt}$ (panel A, calculated from B_A Stark shift measured in the 800 nm region) and $N_{B_A^-}(t)$ (panel B, measured for $P^+B_A^-$ absorption change in 980~1040 nm spectral region) in *Rb. sphaeroides* reaction center in wild type and its M210 mutants.

It is demonstrated that the dynamic Stark shift approach gives the qualitatively correct result for $k_{B\to H}$ between wild type reaction center and the mutants. It is noteworthy to point out that even though the wild type reaction center has the fastest overall $P^* \to P^+H_A^-$ electron transfer rate, it does not appear to optimize the $B \to H$ step significantly.

Dynamic dielectric asymmetry in charge separated reaction centers

The bacterial reaction center has been found to be functionally asymmetric even though its structure has quasi-C2 symmetric branches. Many studies have been performed to understand the origin of this. Steffen et al. identified a dielectric asymmetry in charge separated photosynthetic reaction center by measuring the Stark effect spectrum[103]. The hypothesis from this study is that the dominant A

side electron transfer is associated with a larger dielectric constant of the protein environment, thereby increasing orbital overlap and enhancing the electron coupling between reactant and product state. Continuum dielectric studies using a static structure also concluded that the field also favors charge separation along the L branch. With the dynamic Stark shift approach, the dielectric asymmetry is a natural extension of the definition adopted in the steady state by defining it as a relative ratio between the time dependent field-induced energy level shift from two cofactors, B_A and B_B ($\Delta\nu_{B_A}(t)/\Delta\nu_{B_B}(t)$). The results from the wild type reaction center and its mutants are summarized in figure 7, while the results from Q_A-depleted reaction center as well as the steady state data published by Steffen et al. (1.5 K, $P^+Q_A^-$ state) are included as a reference.

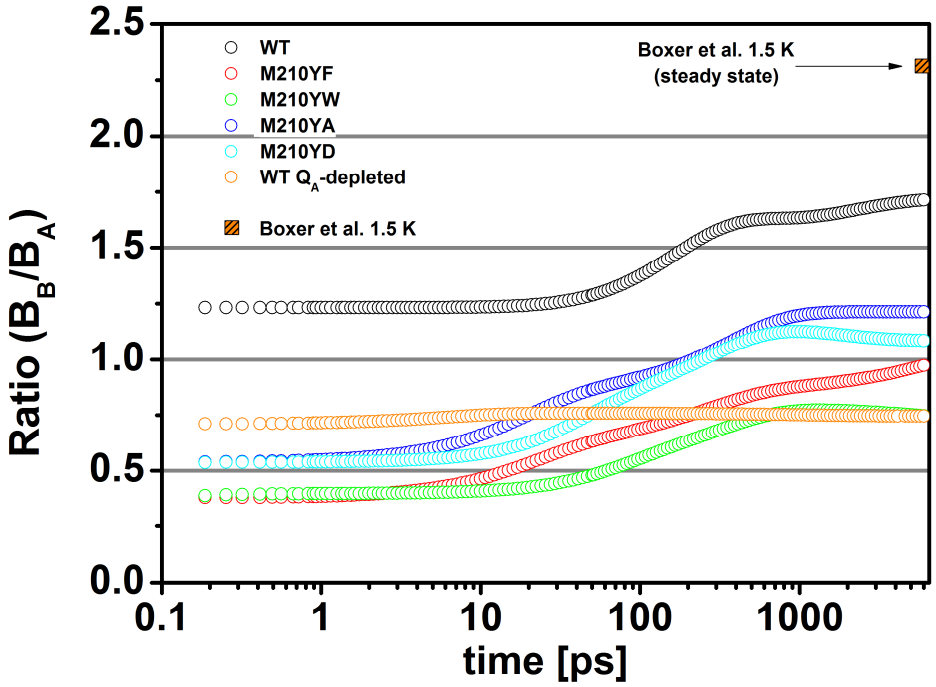

Figure 7: The time dependent evolution of dynamic dielectric asymmetry after charge separation in wild type reaction centers (including QA-depleted reaction

centers) and the M210 mutants. The dynamic dielectric asymmetry is expressed as a dynamic ratio of the Stark shift of accessory bacteriochlorophylls from two branches (B_A and B_B). Data are collected at room temperature over a 6-ns time window. The steady state dielectric asymmetry at low temperature (1.5 K) in reference [103] is also presented, shown as a shaded square.

There are a couple of interesting observations from the dynamic asymmetry curves of figure 7. Instead of a single value measured in steady state from previous experiments, the curves show that at least a portion of the dielectric asymmetry gradually builds up as charge separation continues. This is not very surprising because a continual charge separation in space will result in a response of protein structural reorganization in the L branch, while the M branch should experience much less reorganization particularly after primary charge separation in complete. In this sense, the dynamic dielectric asymmetry observed here is more likely the effect of unidirectional charge separation rather than a cause of it. This speculation is supported by the observation in Q_A-depleted reaction centers. The Q_A-depleted reaction center has very little dynamic asymmetry evolution after the primary charge separation, and the subsequent charge recombination process appears to be a slow, diabatic process (quasi-equilibrium) that leads to indistinguishable dielectric relaxation kinetics in the two branches. It appears that all of the mutants at M210 as well as quinone depletion cause a change in the dielectric asymmetry during primary charge separation, suggesting a static perturbation of the reaction center structure near B_A or B_B. It is worthwhile to noting that there is some preliminary evidence suggesting that this may be true, for example, the early time excited state (<1 ps) spectrum in the 800 nm region

that mostly reflects a difference in the electron coupling and orbital overlap of B_A and B_B are quite different between native wild type reaction center and Q_A-depleted ones prepared in two different ways, a detergent eluted one and a single point mutant that occupies the quinone pocket(AM260W) (see Supporting Information figure-S1).

Conclusion

The dynamic Stark shift of the monomeric bacteriochlorophylls in the charge separated reaction center has been analyzed with a sequential state analysis followed by a global fitting procedure on the resulting EAS. The time dependence of this Stark shift reflects a dynamic change of the effective dielectric constant susceptible to the variation of the internal field formed between the hole on the dimer and the bacteriopheophytin anion. In the wild type reaction center, the time dependence of the B_A Stark shift is identical to the electron transfer kinetics occurring in this branch, suggesting that permanent dipole change $\Delta\mu$ probably dominates the band shift expression in (52). In contrast, some of the mutants, for example, M210YD, show a quadratic Stark effect in which a polarizability change of B_A becomes significant, possibly because of the aspartic acid replacement. The uneven development of the dielectric response from the two potential electron transfer branches of the reaction center was found to be associated with the process of charge separation along the A branch. In other words, although certain static dielectric asymmetry was found immediately after light excitation, a major

part of the dielectric asymmetry observed in the steady state spectrum may be induced by the charge separation.

Supplemental data

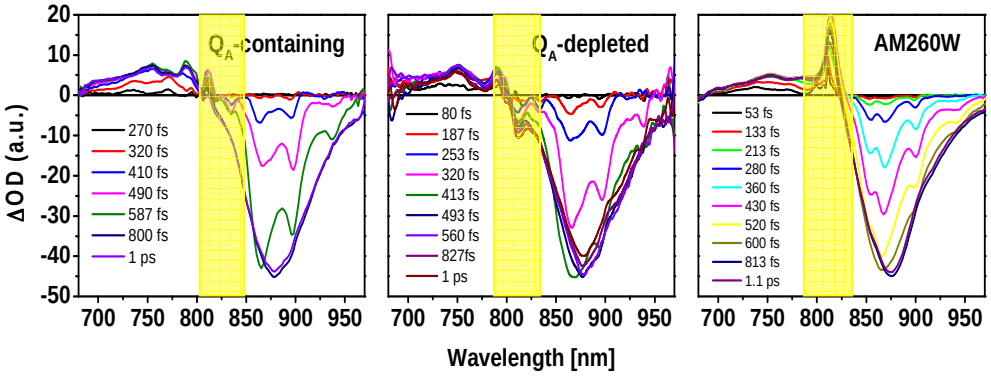

Figure S1: The time resolved spectra in the 680-970 nm spectral region for three reaction center samples (Q_A-containing wildtype RC, Q_A-depleted wildtype RC, and AM260W mutant RC) during the early time evolution (0~1 ps) after 860 nm light excitation. The major spectral differences in the 800 nm region are highlighted in yellow.

CHAPTER 5

Preliminary work and concluding remarks

Transient CD spectroscopy, a potentially useful approach to explore the protein dielectric relaxation

Following light excitation, the reaction center protein is agitated from the ground state and subsequent electron transfer occurs. As a response to the instantaneously redistributed charges on the chromophores, the protein matrix then experiences dielectric relaxation that is driven by the readjustment of the nuclei, which occurs on multiple time scales (ps-ms). Clearly, acquiring information about the protein dielectric relaxation is very critical to the understanding of this system. Wang et al. first used a 280 nm absorption change of two tryptophan residues to characterize the protein dielectric environment relaxation near the special dimer (P). Determining the dielectric relaxation kinetics allows one to model the change of the primary electron transfer kinetic rate as a function of the driving force accurately (see the reaction diffusion model section in Chapter 1). In Chapter 4, the dynamic Stark shift characterizes the variation of the interaction energy between the charge separation-induced field and the probe chromophores' transition dipoles. The probe chromophores in this approach include the accessory bacteriochlorophylls on both symmetric branches (B_A and B_B). It utilizes the fact that both cofactors remain in their ground states almost all throughout the electron transfer, and their ground state absorption bands can be used as good spectral indicators of the energy level shift due to the external field. Dielectric relaxation kinetics measured using the dynamic Stark shift may be different from those

measured with tryptophan absorption signals because the dielectric response not only varies with time but also behaves anisotropically in the protein, i.e. $\varepsilon = \varepsilon(\vec{x}, t)$. Investigation of protein dielectric relaxation can then be extended to a consideration of the time domain and the different positions of the protein interior. In principle, the dynamic Stark shift approach can be applied to both the accessory bacteriochlorophylls (B_A and B_B) and the bacteriopheophytins (H_A and H_B), but in practice, the H_A and H_B absorption bands are harder to be separated at room temperature due to line shape broadening and smaller electrochromic shift effects. Analysis of the bacteriopheophytins is also more complex as a result of the A branch's role (H_A) in being a real electron acceptor, which greatly depletes the corresponding ground state population that can be used to characterize the protein relaxation. A more general approach for studying protein relaxation needs to be developed.

A potential alternative for the dynamic Stark shift indicator is the transient circular dichroism (CD) spectra of the chromophores. As described in Chapter 1, the CD spectrum of a molecule is directly associated with the dot-product of its electric dipole and magnetic dipole. Although they have been widely used to characterize the chirality of molecules, CD spectra are more commonly used for finger printing purposes. Different secondary structures of a protein have their unique CD spectra in the UV region and can be used to estimate the content of each secondary structure. The origin of these different CD spectra stems from a geometrically regular arrangement of amino acid blocks, each with electric

dipoles and magnetic dipoles. If the relative magnitude and orientation changes of either dipole are associated with the structural change of the molecule, the CD spectrum inversely can be utilized as a good indicator for those structural changes. The kinetic assay of CD spectra is a long-established technique used to characterize protein folding and unfolding in certain environment. But those applications are mostly on a very slow time scale, for example, several hours. In recent years, some fast transient CD work has emerged and has provided the possibility of exploring the fast changes in either nuclear conformation or electronic state. The transient CD technique was applied to the reaction center system 20 years ago, but has since fallen out of use because of its complexity. Two transient CD spectra corresponding to two electronic states — $P^+H_A^-$ and $P^+Q_A^-$ — have been measured, but no specific conclusions have been made about the protein contribution[214]. Thanks to the advancements in laser technology, the application of transient CD spectra in reaction center protein is being revisited as a tentative trial. The paragraphs that follow detail only a preliminary experimental work. More investigation is required, and even more efforts are needed to interpret and translate the data into an understandable language.

Experiment Setup

There are many setup schemes that can be used to measure the transient CD spectra[214-225]. Recently, Mangot et al. proposed an experiment design that requires only a little modification to the conventional broadband pump-probe setup to

obtain the time-resolved ORD/CD spectra with a satisfactory signal-to-noise ratio. This type of design was adopted in this work[225]. The major modification is in the polarization modulation and detection of the probe light. This is explained in figure 1

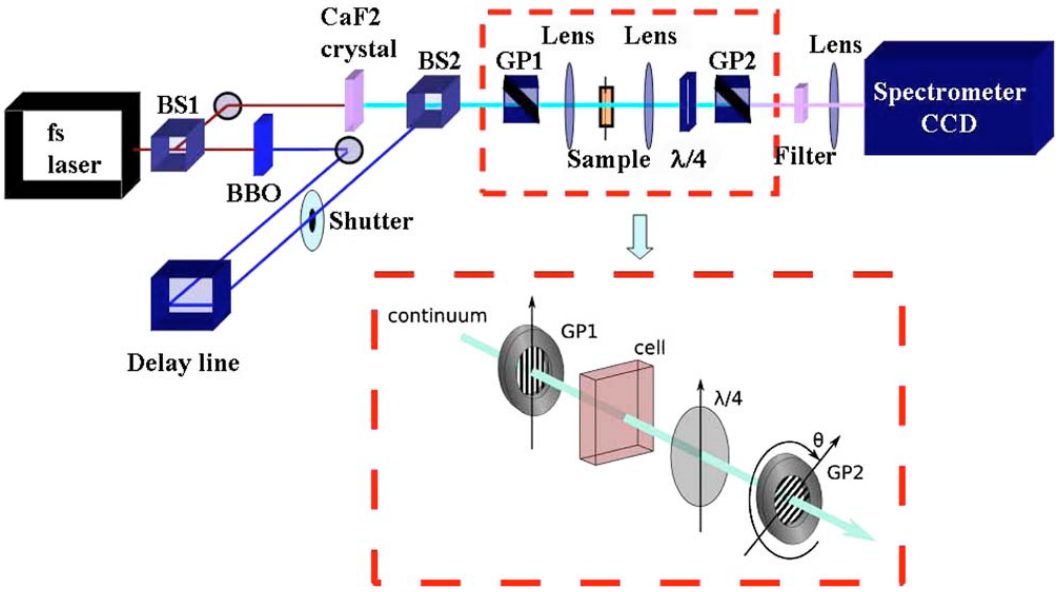

Figure 1: A broadband transient dichroism spectroscopy setup adapted from a pump-probe setup. The optical elements in the red dashed-line box is the ellipsometer scheme. GP1 and GP2 are Glan-Thompson polarizers; BS1 and BS2 are beam spliters, and $\lambda/4$ is the quarter wave plate. Scheme adapted from Mangot et al[225].

The light polarization change in the ellipsometry is explained in figure 2. Incoming linear polarized light, which can be treated as a superposition of a left-handed circular-polarized component and a right-handed circular-polarized components of equal amplitude and phase, is applied to the sample. Different absorption cross-sections for the two circular-polarized components induce a de-polarization of the input linear polarized light, if the sample has any chirality.

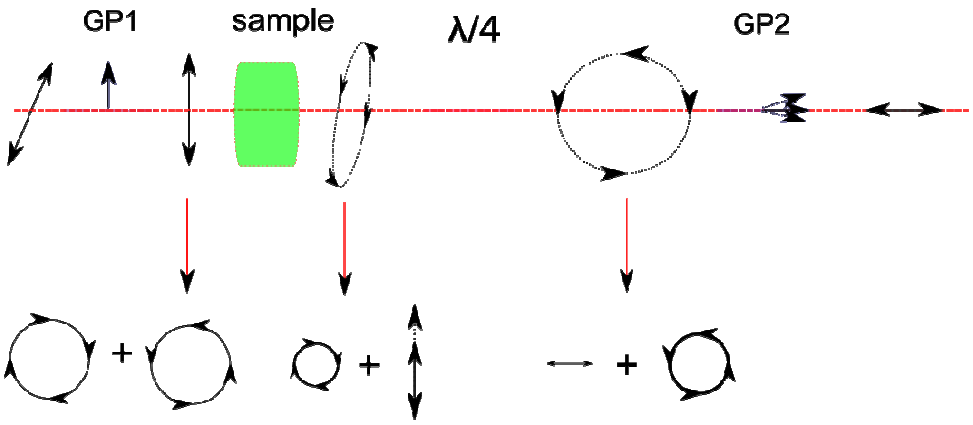

Figure 2: Probe light electric vector polarization change in the ellipsometer.

The de-polarization caused by the sample is then picked up by the quarter-wave plate, and converted into a linear polarized component that is sensitive to the polarization analyzer, GP2, which has a crossing polarizing axis with GP1.

Data analysis

The optical rotatory dispersion (ORD) in a sample is defined as:

$$\delta = 2\pi \frac{(n_L - n_R)}{\lambda} l \qquad (56)$$

where n_L an n_R are the refractive indices of the left- and the right-handed circular polarizations, respectively. The CD in a sample is defined as:

$$\eta = (\alpha_L - \alpha_R) l \qquad (57)$$

where α_L and α_R are the absorption coefficients of the left-handed and right-handed circular polarizations, respectively. The thickness of the sample is

represented by *l*. In the Jones matrix representation, the output light polarization is:

$$E^{out} = M_{Analyzer} M_{Sample} M_{Polarizer} E^{in} \qquad (58)$$

Let the incoming light polarization be:

$$E^{in} = \begin{pmatrix} E_{0x} \\ E_{0y} \end{pmatrix} \qquad (59)$$

and the matrix representing the sample can be approximated by:

$$M_{Sample} = e^{-\alpha l/2} \begin{pmatrix} 1 & -i(\frac{\eta}{4} + i\ \frac{\delta}{2}) \\ i(\frac{\eta}{4} + i\ \frac{\delta}{2}) & 1 \end{pmatrix} \qquad (60)$$

and the matrix representing the analyzer is:

$$M_{Analyzer} = \begin{pmatrix} \theta^2 & \theta \\ \theta & 1-\theta^2 \end{pmatrix} \qquad (61)$$

By ignoring all of the higher order terms, a simple matrix math will result in:

$$I^{out} = I^{in} e^{-(\alpha_L + \alpha_R) l/2} \left[1 - \left(\frac{\delta^2}{4} + \frac{\eta^2}{16} \right) \theta^2 - \delta\theta + \left(\frac{\delta^2}{4} + \frac{\eta^2}{16} \right) \right] \qquad (62)$$

The minimum of the parabola defines the ORD angle as:

$$\theta_{min} = \frac{\delta/2}{1 - \left(\frac{\delta^2}{4} + \frac{\eta^2}{16} \right)} \cong \delta/2 \qquad (63)$$

Similarly, switching the role of δ and η, the CD angle becomes $\theta_{min}; \eta/4$, and the CD coefficient is henceforth:

$$\Delta\varepsilon = \frac{4\pi\theta_{min}}{180 n(10) C_{mol}} \qquad (64)$$

where C_{mol} is the molar concentration. The minimum of the transmission parabola is calculated by scanning the polarization angle of the analyzer in a very small range (-1^{o}~1^{o}). To measure the CD spectrum of the reaction center sample in its ground state, a 2 mm thick fused-quartz cuvette was used to hold the Q_A-depleted reaction center without any stirring. A sample concentration of $OD_{865} = 0.8$ was used. The ground state state CD spectrum measurement does not require any excitation, thus blocking the excitation beam. For each wavelength, the transmission light intensity varies as a function of the polarization angle. The detection of the light polarization is realized by continuously rotating the analyzer with a piezoelectricity controlled motor (5e-5 degree precision). The parabola derived in equation (62) is experimentally determined as in figure 3 .

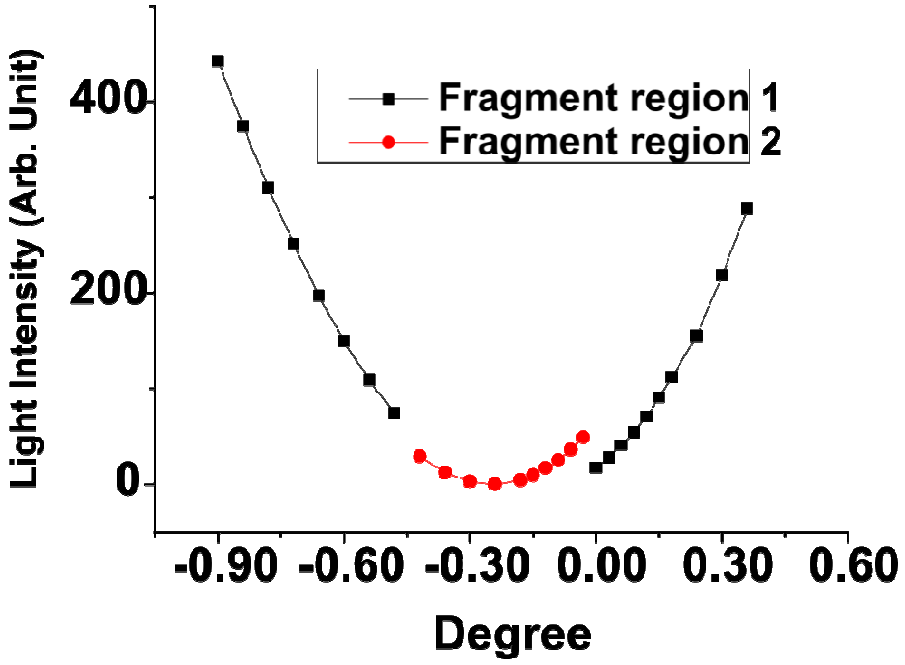

Figure 3: Transmission light intensity as a function of the polarization angle of the scanning polarizer. The parabola is broken into two segments (red and black),

indicating a sudden change of transmission light intensity, possibly due to the light beam alignment issue or to mismatching of the polarizer pair in use (GP1 and GP2).

The whole parabola in our measurement is broken into two segments, which could be associated with a partial cut of the light beam during the polarization analyzer rotation. An imperfect light beam alignment or a mismatch of the polarizer pair (GP1 and GP2) in used, could cause these results. Both polarizers should be Glan-Thompson polarizers (CVI), but only one was available in the lab, and the other one was substituted by a Glan-Tyler polarizer. To solve this problem, only the black segment is fitted to determine its minimum, θ_{min} (the other segment, red part, results in similar spectrum if fitted individually). When the angular minimum has been determined for each individual wavelength, the spectral dependence can then be determined. The ground state CD spectrum is obtained by performing the measurements in two conditions: 1) in the buffer detergent 2) in the reaction center sample. The subtraction of the second spectrum from the first one produces the ground state spectrum (figure 4).

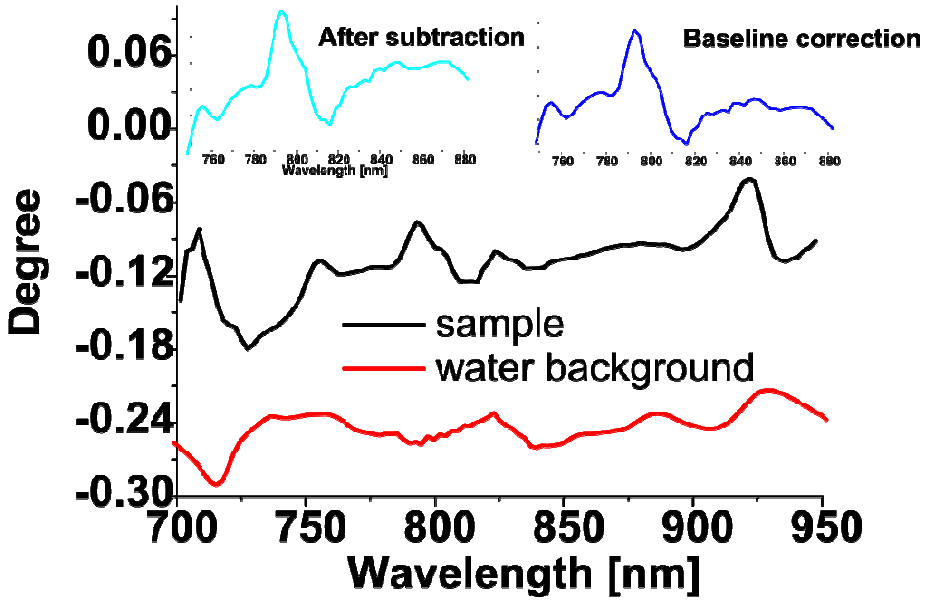

Figure 4: The ground state CD spectrum measured over the 760-880 nm wavelength region by a background subtraction method described in the text. The spectrum was calibrated with a simple baseline correction within a small range of the spectral region, a region where such a procedure is considered applicable for the wavelength dependence of the broadband quarter-wave plate.

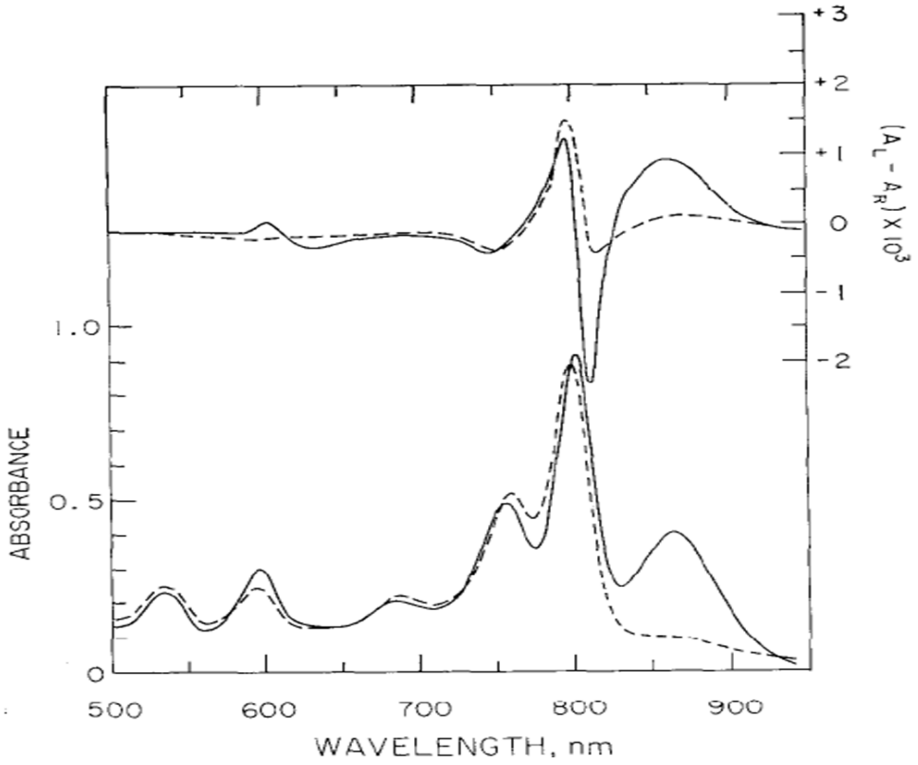

Figure 5: The CD spectra (top of graph) and the ground state absorption spectra (bottom of graph) measured in the 500-950 nm wavelength region for the *Rb. sphaeroides* reaction center R-26 strain in 0.01 M Tris buffer, with pH 7.5, at room temperature. The solid lines represent measurement taken when P is neutral, and the dashed lines represent measurements taken when P is chemically oxidized to P^+ by adding potassium ferricyanide. This figure is adapted from Reed et al[226].

The quarter-wave plate is a Berek compensator (broadband compensator Model 5540, Newport Inc.) with its center wavelength set to 800 nm. Residual wavelength dependence (nearly linear around the center wavelength, but significantly deviates from linearity when moving away) to give an artifact-free spectrum. A rigid treatment should use a racemic sample (chirality molecules of mirror symmetry, equal concentration mixed) to calibrate the wavelength dependence of the Berek compensator. Because access to such a sample was unavailable during current test stage, calibration has been roughly approximated

using a linear function. The final CD spectrum in this test has a large similarity with the previous report, yet those spectral patterns were found in the charge separated state (figure 4 and 5). The reason for this discrepancy could be that the probe light intensity being used was too high, or that the approximated calibration on the Berek compensator was far from perfect.

Extension of the measurement to the transient spectra is much simpler because they usually appear as difference spectra, which originates from the sample changes and greatly reduces the static background interference. The difference spectra record the difference of two θ_{min} before and after light excitation, which requires fitting two parabolas separately; however, the following derivation work shows that this step can be improved with a more robust linear fitting strategy. First, one calculates the exact form of $\Delta\theta_{min}$:

$$\theta_{min}^{before} = \frac{\eta/4}{1-\left(\delta^2 4 + \eta^2 16\right)}$$

$$\theta_{min}^{after} = \frac{(\eta + \Delta\eta)/4}{1-\left(\frac{(\delta + \Delta\delta)^2}{4} + \frac{(\eta + \Delta\eta)^2}{16}\right)}$$

$$\Delta\theta_{min} = \theta_{min}^{after} - \theta_{min}^{before} \qquad \left(or \quad \frac{\partial\theta_{min}}{\partial\eta}\right)$$

$$= \frac{\Delta\eta}{4} + \frac{\eta}{4}\left[\frac{\delta\cdot\Delta\delta}{2} + \frac{\eta\cdot\Delta\eta}{8}\right]$$

$$= \frac{\Delta\eta}{4}$$

If data is being collected using a pump-probe scheme, then only ΔA is being recorded, such that:

$$\Delta A = \left[\left(\frac{(\delta + \Delta\delta)^2}{4} + \frac{(\eta + \Delta\eta)^2}{16}\right)\theta^2 + \frac{(\eta + \Delta\eta)\theta}{2} - \left(\frac{(\delta + \Delta\delta)^2}{4} + \frac{(\eta + \Delta\eta)^2}{16}\right)\right]$$

$$- \left[\left(\frac{\delta^2}{4} + \frac{\eta^2}{16}\right)\theta^2 + \frac{\eta\theta}{2} - \left(\frac{\delta^2}{4} + \frac{\eta^2}{16}\right)\right] \qquad (65)$$

Consider that in practice, θ, δ, η are all very small, $<< 1$, and therefore all the significant terms after the subtraction include the following:

$$\Delta A = \frac{\Delta\eta \cdot \theta}{2} - \left(\frac{\Delta\delta^2}{4} + \frac{\delta \cdot \Delta\delta}{2} + \frac{\Delta\eta^2}{16} + \frac{\eta \cdot \Delta\eta}{8}\right)$$

which is purely a linear function of the polarization angle. Fitting the slope of the linear function, $\Delta A(\theta)$, provides the ΔCD value for that wavelength. Transient CD spectra were measured in rotating wheels, allowing for characterization of the excited state and the following charge separated states ($P^+B_A^-$, $P^+H_A^-$, *and* $P^+Q_A^-$).

Results and Discussion

The measurement of transient CD spectra has been tested on two reaction center samples, the wild type and M210YF mutant. The results are summarized in figure 6.

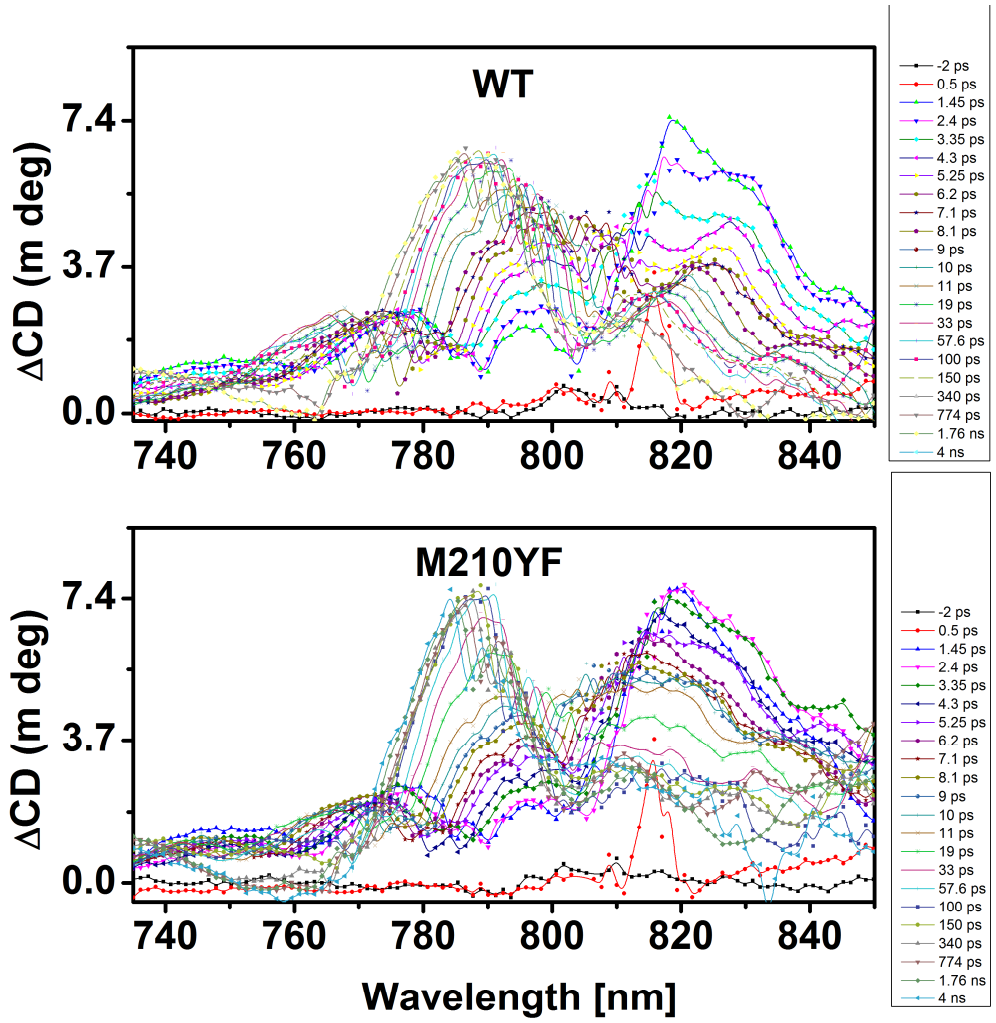

Figure 6: Time resolved CD spectral changes in the wild type reaction center and the M210YF mutant measured in the 740-850 nm wavelength region.

In general, the difference CD spectra of the wild type and M210Y mutant are very similar in shape, barring minor differences in certain shoulder band locations. This is not very surprising, because in the first place, the major charge separation pathways are similar between those two reaction centers, and secondly, the protein dielectric relaxations near the special dimer are shown to be nearly

identical for all of the mutants. In order to understand the CD spectra, a survey into its origin would be beneficial (a brief introduction of the rotatory strength is given in Chapter 1).

The rotatory strength signal change in a pump-probe setup can have two sources: 1)the chromophores that are still in their ground states can have electric dipole and magnetic dipole changes caused by the environment electrostatic fluctuation(external field and nuclear rearrangements) 2) the chromophores that leave from their ground states and enter other electronic states (excited state or charge separated states) have their electric dipole and magnetic dipole changes solely caused by electronic state transition. According to formula (3),(4), and (5) in Chapter 1, for ground state CD signals, the transition goes from ground state to excited state, i.e. for the subscripts *a* and *b* in expression (5)

$$a = gr$$

$$b = ex$$

For non-linear electronic CD signal, the chromophores are in their excited state or charge separated states (including all the relaxed versions), i.e.:

$$a = ex\ ORcs - n\ (n = 1,2,3...)$$

$$b = gr\ ORex - n\ (n = 2,3...)$$

The reverse transition observed in excited state is called “negative rotatory dispersion”, it is predicted by Condon in 1937[227]—“*The question is rather of pure theoretical interest as it is unlikely that a sufficient concentration of excited optically active molecules could be obtained to study the question experimentally*”— when laser has not been invented yet. According to Condon's

paper[227], the positive rotatory dispersion and the negative rotatory dispersion have the following relationship:

$$R_{ba} = -R_{ab} \qquad (66)$$

This expression implies that, unless there is a lower excited state to higher excited state transition occurring in the same wavelength region, the low lying excited state CD spectrum should be mirror the ground state CD spectrum. For the very early time (< 3 ps), when P* dominates, the difference CD signal (ΔCD) , or the difference rotatory strength, ΔR, is $\Delta R = R_{ex,gr} - R_{gr,ex}$, and applying the mirror rule above, one can determine that $R_{gr,ex} = -\frac{\Delta R}{2}$. This relationship indicates that the difference CD spectrum at that moment should mirror the shape of the ground CD spectrum assigned to P, which is the red part of the ground state spectrum among the transitions of all 6 cofactors (figure 7).

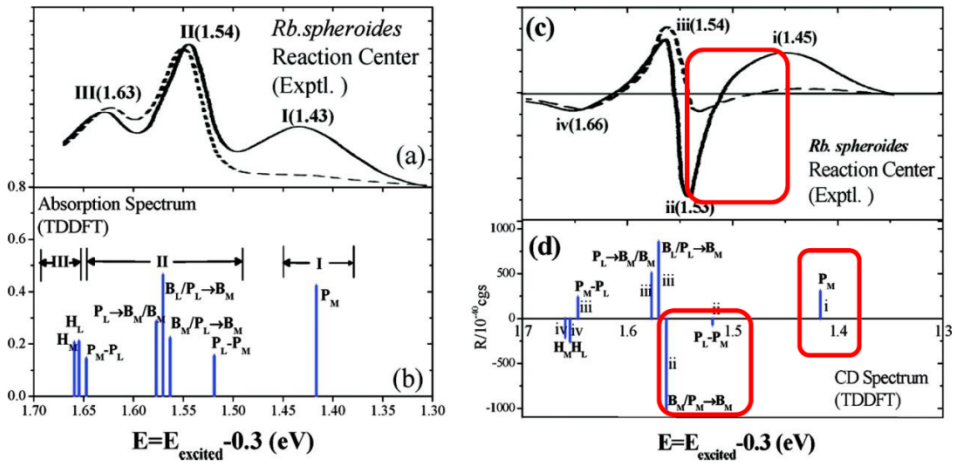

Figure 7: Spectral line assignment in the ground state absorption spectrum and the CD spectrum (from figure 47). The spectral lines are from TDDFT calculations (see text). The electronic transitions associated with P→P* are highlightened by red boxes. Figure is adapted from Ren et al[90].

Figure 7 is reproduced from Ren et al.[90], panel (a) and (c) are the experiment absorption spectrum and CD spectrum respectively, while (b) and (d) are the corresponding first principle calculation using time dependent density functional theory (TDDFT, B3LYP/6-31G basis set was applied on all 6 cofactros). The red rectangular boxes are the spectral regions used to compare with the difference CD signal measured in this work (figure 49 and 50a). Note that the difference CD spectrum at 0.5 ps has a major peak around 1.53 eV which is also found in figure 50a, but in opposite sign.

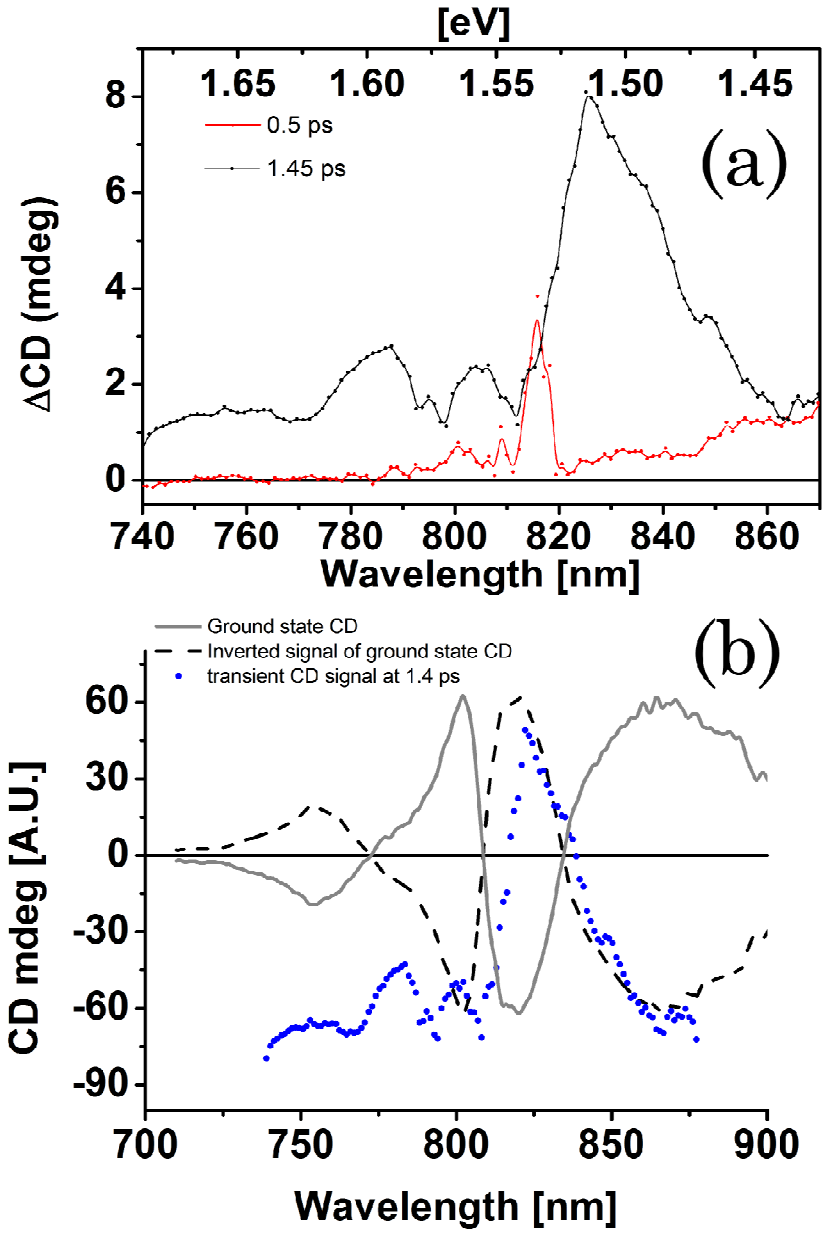

Figure 8: (a) Early time difference CD spectrum measured at 0.5 ps and 1.45 ps for *Rb. sphaeroides* wild type reaction center. The upper scale is in eV, while the bottom scale is in nm. (b) Testing the mirror relationship between the ground CD spectrum (inverted) and the difference CD spectrum at 1.45 ps (vertically translated and scaled). The ground CD spectrum was measured on a commercial CD spectrometer (Model 815, JASCO Inc.) over a 700-900 nm wavelength region.

The later spectral evolution of the charge separated state is more complicated, for example, the major peak in the spectrum at 1.45 ps in figure 8a is red shifted relative to the 0.5 ps spectrum. Despite this, the spectral shape of the 1.45-ps difference CD spectrum does share a large similarity with the inverted ground state CD spectral profile (figure 8b, 820-870 nm). Because there is not an abundant amount of theoretical work addressing the transient CD spectroscopy associated with the charge separated state, the discussion of these results is limited. Perhaps future theoretical/computational work can have further development on this topic, and best utilize the transient CD spectra that have been measured.

Concluding remarks

Electron transfer in proteins is a complex phenomenon that is not well understood. Researchers have approached this issue from different perspectives for many years. The Marcus theory, which is the mainstream nowadays, dominates the understanding without many alternatives. Limitations of the original Marcus theory in bimolecular electron transfer have been recognized for some time, and modifications to the theory continue to develop. Most of those modified versions remain on the analytical or numerical level, and the common act is to adopt set parameters as the input for rate constant prediction. The most common data retrieved from the spectroscopy experiment on electron transfer is the time course of electron transfer kinetics, the rate constant of which does allow for a direct comparison with the simulation data on this part, but such a

comparing method leaves the uncertainty of multiple combination in the parameter space (unless the number of parameter is only one). The difficulty largely comes from the limited sources of the experiment data that are available, making separation of parametes, which is required to test a theoretical model, very difficult. To solve this problem, one possibility is to shift the focus away from the reaction rate, which is currently the meeting point for experiments and computational simulations. Recent simulation techniques, like molecular dynamics simulation based on empirical force field, or *ab initio* quantum chemistry calculations, open the possibility of obtaining various parameters in a realistic system with satisfactory accuracy (the only question is the computing power). If the spectroscopy experiments can provide information about a certain parameter that is coupled to the electron transfer but more than simply the electron transfer process itself, it would be useful to test those theoretical models more effectively.

A theme that can be found throughout all electron transfer studies in this thesis is the role of protein dielectric relaxation after light excitation and the charge separation that follows. Once the system is perturbed (e.g. being excited) from its ground state in a portion of its electron distribution, the response of the atomic system was divided into two parts: the nuclei (heavy positive charges, slow response to polarization) and the electron (negative charge of nearly no mass, fast response to polarization). The corresponding dielectric constants were also separated into two: optical dielectric constant ε_o (high frequency limit, corresponds to electron polarization), and static dielectric constant ε_s (low

frequency limit, corresponds to nuclei polarization). For most electron transfer processes under consideration, the reactions rates are faster than the nuclear relaxation frequency but slower than the electron relaxation frequency. Therefore, the electron transfer rate itself defines a low frequency cut-off for the nuclear relaxation responses in the frequency domain. At this point, the frequency dependence of the dielectric relaxation is significant because its functional form directly determines how it is coupled to the electron transfer.

One of the reasons that the protein electron transfer is difficult is because the nuclei can have a significant polarization inertial which directly lead to a frequency dependence of dielectric relaxation stated above. Such a polarization inertial is associated with the mechanical nature of the protein: it is flexible but not too flexible. From either end, it would be much easier to deal with. If the atoms in a protein are tightly constrained like those in a crystal or in a solid, this is then reduced into some phonon bands,and the electron transfer is dominated by electron-phonon coupling. Protein frozen at very low temperature somehow approaches this limit, as the the atoms loses the thermal activation energy and tend to stay vibrating around the equilibrium position at very low amplitudes. The Marcus model with the Franck-Condon factor in place of the exponential factor is an exact description for such a scenario:

$$k_{ET} = \frac{2\pi}{\eta} H_{RP}^2 \left(\frac{1}{4\pi\lambda_0 K_B T} \right)^{12} (FC) \tag{67}$$

Where FC is the Franck-Condon factor:

$$(FC) = \sum_{\nu'} exp(-S)\frac{S^{\nu'}}{\nu'!} exp\left[-\frac{(\lambda_0 + \nu'\eta\omega + \Delta G^0)^2}{4\lambda_0 K_B T}\right] \quad (68)$$

Here S is the Huang-Rhys factor, and it represents the phonon number for the reorganization energy possessed by each vibrational mode, i.e.:

$$S = \frac{\lambda_f}{\eta\omega}$$

In the opposite case, if a protein is not held by any covalent bonds, the nuclei are free to move like ions in the electrolytes, particularly at high temperature. If the nuclei relaxation is fast enough to be incorporated into the electron transfer time window, a full "thermal equilibrium" is reached within the reaction time scale, which is in accordance with standard Marcus theory. The two extremes mentioned above constitute two types of reorganization energy: one is vibrational (or sometimes called the "fast" one because of the time scale of the nuclei movements) λ_f , and the other one is because of "solvation" (or sometimes called the "slow" one) λ_s . The total reorganization energy is given by $\lambda = \lambda_f + \lambda_s$. The "slow" reorganization energy λ_s is the one that is sensitive to the electron transfer time window, which has been pointed out by Matyushov et al[146, 163]. In general, global translational and rotational motion of reactants are greatly confined by the protein structure scaffolds whereas the motions of free ions in solution are not so restricted. Conformational changes of different collectivities then results in a fairly long memory in the dielectric relaxation kinetics and

behaves as multiple-exponential decays. In the experiments, one of the goals was to obtain this dielectric relaxation decay. In Wang et al's work, the tryptophans around the dimer were used as a probe to follow such a decay, probably via interactions with an induced, local field in close proximity. In the dynamic Stark shift work, the transition dipoles from the accessory BChl-*a* s were used to sense the internal field from $P^+H_A^-$ or $P^+Q_A^-$. Even though the characterization of dielectric realxation by the aforementioned measurements remain at the phenomenological level, for example, the time dependence of the reaction field is simply embodied in seeing a difference compared with the electron transfer kinetics, yet they have the potential to aid in the understanding of protein dielectrics at rapid time scales. By recognizing that the protein matrix generates a reaction field—in addition to the fields formed by chromophore charges in vacuum—the contribution of the polarization intensity to the macroscopic field and its time dependence both show strong correlations with the charge/dipole distribution of the molecule's native geometry.

A first step to exploit the dielectric response can be to prepare certain mutants that re-design the charge/dipole distribution on the native geometry. While this method would not guarantee that the molecular forces are entirely preserved, the effect is assumed to be minor if single-site mutagenesis is being introduced. The contamination on the cofactor free energy level can be reduced by moving the mutation site away from the cofactor binding site. Other environmental factors can also be utilized to modulate the dielectric relaxation kinetics, including: buffer pH, detergent type, salt concentration, viscosity,

temperature, and pressure. This type of experiment design is easy to devise and carry out, but as explained above, as yet none of them can not adequately isolate one Marcus formula parameter at a time. The reorganization energy and its time dependence is in close relation to the dielectric response of the system[80], and experimental manipulation of this term is usually realized by changing the temperature. This practice appears to have a good specificity in the primary electron transfer as shown[84], but does not necessarily in reactions that occur on a longer time scale. A possible solution might be to use a technique that can selectively populate (or depopulate) the phonon density at a certain frequency region, such as a non-linear terahertz excitation experiment. In this type of experiment, a strong terahertz pulse is used to excite a sample by selectively "heating" the protein at a given phonon frequency range, thus overcoming some dynamic barriers and propelling the dielectric relaxation. Such a technique has been used in semi-conductor research before[228, 229], but it is not clear if the energy of the terahertz pulses indirectly generated by the amplified Ti-sapphire laser pulse is enough to achieve a good signal-to-noise ratio in the application here.

REFERENCES

1. K. Lapouge, A. Näveke, A. Gall, et al., Biochemistry **38** (34), 11115-11121 (1999).

2. S. M. Prince, M. Z. Papiz, A. A. Freer, et al., Journal of Molecular Biology **268** (2), 412-423 (1997).

3. P. Jordan, P. Fromme, H. T. Witt, et al., Nature **411** (6840), 909-917 (2001).

4. A. Zouni, H.-T. Witt, J. Kern, et al., Nature **409** (6821), 739-743 (2001).

5. L. Fiedor, A. Kania, B. Myśliwa-Kurdziel, et al., Biochimica et Biophysica Acta (BBA) - Bioenergetics **1777** (12), 1491-1500 (2008).

6. V. Iancu and S.-W. Hla, Proceedings of the National Academy of Sciences **103** (37), 13718-13721 (2006).

7. C. A. Wraight and R. K. Clayton, Biochimica et Biophysica Acta (BBA) - Bioenergetics **333** (2), 246-260 (1974).

8. O. Nanba and K. Satoh, Proceedings of the National Academy of Sciences **84** (1), 109-112 (1987).

9. J. P. Allen, G. Feher, T. O. Yeates, et al., Proceedings of the National Academy of Sciences **84** (17), 6162-6166 (1987).

10. B. K. Pierson and J. P. Thornber, Proceedings of the National Academy of Sciences **80** (1), 80-84 (1983).

11. J. P. Allen, G. Feher, T. O. Yeates, et al., Proceedings of the National Academy of Sciences **85** (22), 8487-8491 (1988).

12. E. C. Kellogg, S. Kolaczkowski, M. R. Wasielewski, et al., Photosynthesis Research **22** (1), 47-59 (1989).

13. C. Kirmaier, D. Holten and W. W. Parson, Biochimica et Biophysica Acta (BBA) - Bioenergetics **810** (1), 49-61 (1985).

14. M. E. Michel-Beyerle, M. Plato, J. Deisenhofer, et al., Biochimica et Biophysica Acta (BBA) - Bioenergetics **932** (0), 52-70 (1988).

15. D. M. Tiede, E. Kellogg and J. Breton, Biochimica et Biophysica Acta (BBA) - Bioenergetics **892** (3), 294-302 (1987).

16. C. A. Hunter and J. K. M. Sanders, Journal of the American Chemical Society **112** (14), 5525-5534 (1990).

17. B. Pullman, *Intermolecular Forces: Proceedings of the Fourteenth Jerusalem Symposium on Quantum Chemistry and Biochemistry Held in Jerusalem, Israel, April 13-16, 1981*. (D Reidel Pub Co, 1981).

18. K. Morokuma, Accounts of Chemical Research **10** (8), 294-300 (1977).

19. A. Warshel and W. W. Parson, Journal of the American Chemical Society **109** (20), 6143-6152 (1987).

20. W. W. Parson and A. Warshel, Journal of the American Chemical Society **109** (20), 6152-6163 (1987).

21. J. D. McElroy, G. Feher and D. C. Mauzerall, Biochimica et Biophysica Acta (BBA) - Bioenergetics **172** (1), 180-183 (1969).

22. M. Bixon, J. Jortner, M. E. Michel-Beyerle, et al., Chemical Physics Letters **140** (6), 626-630 (1987).

23. T. Arlt, S. Schmidt, W. Kaiser, et al., Proceedings of the National Academy of Sciences **90** (24), 11757-11761 (1993).

24. C. K. Chan, T. J. DiMagno, L. X. Chen, et al., Proceedings of the National Academy of Sciences **88** (24), 11202-11206 (1991).

25. A. R. Holzwarth and M. G. Muller, Biochemistry **35** (36), 11820-11831 (1996).

26. H. Wang, Y. Hao, Y. Jiang, et al., The Journal of Physical Chemistry B (2011).

27. K. Gibasiewicz, M. Pajzderska, J. A. Potter, et al., The Journal of Physical Chemistry B **115** (44), 13037-13050 (2011).

28. A. d. and and S. G. Boxer, The Journal of Physical Chemistry B **103** (41), 8786-8789 (1999).

29. A. Vermeglio and R. K. Clayton, Biochimica et Biophysica Acta (BBA) - Bioenergetics **461** (1), 159-165 (1977).

30. C. A. Wraight, Biochimica et Biophysica Acta (BBA) - Bioenergetics **548** (2), 309-327 (1979).

31. R. Debus, G. Feher and M. Okamura, Biochemistry **25** (8), 2276-2287 (1986).

32. W. Lubitz and G. Feher, Applied Magnetic Resonance **17** (1), 1-48 (1999).

33. M. Okamura, R. Isaacson and G. Feher, Proceedings of the National Academy of Sciences **72** (9), 3491 (1975).

34. G. Feher and M. Okamura, Applied Magnetic Resonance **16** (1), 63-100 (1999).

35. M. Okamura, M. Paddock, M. Graige, et al., Biochimica et Biophysica Acta (BBA)-Bioenergetics **1458** (1), 148-163 (2000).

36. M. Graige, G. Feher and M. Okamura, Proceedings of the National Academy of Sciences **95** (20), 11679 (1998).

37. M. Stowell, T. McPhillips, D. Rees, et al., Science **276** (5313), 812-816 (1997).

38. C. A. Wraight, Frontiers in Bioscience **9**, 309-337 (2004).

39. Z. Zhu and M. R. Gunner, Biochemistry **44** (1), 82-96 (2004).

40. D. Kleinfeld, M. Okamura and G. Feher, Biochimica et Biophysica Acta (BBA)-Bioenergetics **766** (1), 126-140 (1984).

41. B. Boso, P. Debrunner, M. Y. Okamura, et al., Biochimica et Biophysica Acta (BBA)-Bioenergetics **638** (1), 173-177 (1981).

42. P. Eisenberger, M. Okamura and G. Feher, Biophysical Journal **37** (2), 523 (1982).

43. G. Bunker, E. A. Stern, R. E. Blankenship, et al., Biophysical Journal **37** (2), 539-551 (1982).

44. W. Butler, R. Calvo, D. Fredkin, et al., Biophysical Journal **45** (5), 947-973 (1984).

45. G. C. Dismukes, H. A. Frank, R. Friesner, et al., Biochimica et Biophysica Acta (BBA)-Bioenergetics **764** (3), 253-271 (1984).

46. A. Young and G. Britton, *Carotenoids in photosynthesis*. (Chapman and Hall Ltd, 1993).

47. Y. Kakitani, R. Fujii, Y. Koyama, et al., Biochemistry **45** (7), 2053-2062 (2006).

48. A. W. Roszak, K. McKendrick, A. T. Gardiner, et al., Structure (London, England : 1993) **12** (5), 765-773 (2004).

49. R. J. Debus, G. Feher and M. Y. Okamura, Biochemistry **24** (10), 2488-2500 (1985).

50. E. J. Bylina, C. Kirmaier, L. McDowell, et al., Nature **336** (6195), 182-184 (1988).

51. B. Heller, D. Holten and C. Kirmaier, Science **269** (5226), 940-945 (1995).

52. E. Katilius, T. Turanchik, S. Lin, et al., The Journal of Physical Chemistry B **103** (35), 7386-7389 (1999).

53. C. Kirmaier and D. Holten, The Journal of Physical Chemistry B **113** (4), 1132-1142 (2009).

54. M. L. Paddock, C. Chang, Q. Xu, et al., Biochemistry **44** (18), 6920-6928 (2005).

55. W. W. Parson, *Modern optical spectroscopy: with examples from biophysics and biochemistry*. (Springer Verlag, 2007).

56. C. N. Rafferty and R. K. Clayton, Biochimica et Biophysica Acta (BBA)-Bioenergetics **546** (2), 189-206 (1979).

57. J. Breton, Biochemical and biophysical research communications **59** (3), 1011-1017 (1974).

58. J. Breton, Biochimica et Biophysica Acta (BBA)-Bioenergetics **810** (2), 235-245 (1985).

59. J. Stark, Nature **92**, 401 (1913).

60. D. N. LeBard and D. V. Matyushov, Phys. Chem. Chem. Phys. **12** (47), 15335-15348 (2010).

61. D. W. Reed, Journal of Biological Chemistry **244** (18), 4936-4941 (1969).

62. A. Grinvald and I. Z. Steinberg, Analytical Biochemistry **59** (2), 583-598 (1974).

63. A. E. W. Knight and B. K. Selinger, Spectrochimica Acta Part A: Molecular Spectroscopy **27** (8), 1223-1234 (1971).

64. C. W. Dong, SIAM journal on numerical analysis, 759-773 (1993).

65. A. N. Tikhonov, V. I. A. Arsenin and F. John, (1977).

66. S. W. Provencher, Computer Physics Communications **27** (3), 213-227 (2006).

67. A. Livesey and J. Brochon, Biophysical Journal **52** (5), 693-706 (1987).

68. P. J. Steinbach, R. Ionescu and C. R. Matthews, Biophysical Journal **82** (4), 2244-2255 (2002).

69. Y. Zhou and X. Zhuang, Biophysical Journal **91** (11), 4045-4053 (2006).

70. E. G. Novikov, A. van Hoek, A. J. W. G. Visser, et al., Optics Communications **166** (1−6), 189-198 (1999).

71. J. Klafter and M. F. Shlesinger, Proceedings of the National Academy of Sciences **83** (4), 848-851 (1986).

72. I. H. M. van Stokkum, D. S. Larsen and R. van Grondelle, Biochimica et Biophysica Acta (BBA)-Bioenergetics **1657** (2), 82-104 (2004).

73. J. M. Beechem, M. Ameloot and L. Brand, (1985).

74. A. R. Holzwarth, edited by J. Amesz and A. J. Hoff (Springer Netherlands, 2004), Vol. 3, pp. 75-92.

75. G. Suter, P. Klein-Bölting, E. Bittersmann, et al., Chem. Phys., in the press (1990).

76. R. A. Marcus, Reviews of Modern Physics **65** (3), 599-610 (1993).

77. Y. Georgievskii, C. P. Hsu and R. Marcus, The Journal of Chemical Physics **110**, 5307 (1999).

78. H. A. Kramers, Physica **7** (4), 284-304 (1940).

79. H. Sumi and R. A. Marcus, The Journal of Chemical Physics **84** (9), 4894-4914 (1986).

80. H. Sumi and R. A. Marcus, The Journal of Chemical Physics **84** (8), 4272-4276 (1986).

81. D. Zhong, S. K. Pal and A. H. Zewail, Chemical Physics Letters **503** (1−3), 1-11 (2011).

82. L. Zhang, Y. Yang, Y.-T. Kao, et al., Journal of the American Chemical Society **131** (30), 10677-10691 (2009).

83. H. Wang, S. Lin, J. P. Allen, et al., Science **316** (5825), 747-750 (2007).

84. H. Y. Wang, S. Lin, E. Katilius, et al., Journal of Physical Chemistry B **113** (3), 818-824 (2009).

85. J. J. Hopfield, Proceedings of the National Academy of Sciences **71** (9), 3640-3644 (1974).

86. D. Frenkel and B. Smit, *Understanding molecular simulation: from algorithms to applications*. (Academic Pr, 2002).

87. L. Verlet, Physical Review **159** (1), 98-103 (1967).

88. A. R. Leach, *Molecular modelling: principles and applications*. (Addison-Wesley Longman Ltd, 2001).

89. A. van Duin, in *Computational Methods in Catalysis and Materials Science* (Wiley-VCH Verlag GmbH & Co. KGaA, 2009), pp. 167-181.

90. Y. Ren, W. Ke, Y. Li, et al., The Journal of Physical Chemistry B **113** (30), 10055-10058 (2009).

91. M. Ceccarelli, P. Procacci and M. Marchi, Journal of Computational Chemistry **24** (2), 129-142 (2003).

92. S. J. Weiner, P. A. Kollman, D. T. Nguyen, et al., Journal of Computational Chemistry **7** (2), 230-252 (1986).

93. W. L. Jorgensen, J. Chandrasekhar, J. D. Madura, et al., The Journal of Chemical Physics **79** (2), 926-935 (1983).

94. C. I. Bayly, P. Cieplak, W. Cornell, et al., The Journal of Physical Chemistry **97** (40), 10269-10280 (1993).

95. J. Koepke, E.-M. Krammer, A. R. Klingen, et al., Journal of Molecular Biology **371** (2), 396-409 (2007).

96. W. Kaplan and T. G. Littlejohn, Briefings in bioinformatics **2** (2), 195-197 (2001).

97. D. Case, (University of California, San Francisco, 2010).

98. J. C. Phillips, R. Braun, W. Wang, et al., Journal of Computational Chemistry **26** (16), 1781-1802 (2005).

99. P. Gast, P. W. Hemelrijk, H. J. Gorkom, et al., European Journal of Biochemistry **239** (3), 805-809 (1996).

100. W. Humphrey, A. Dalke and K. Schulten, Journal of molecular graphics **14** (1), 33-38 (1996).

101. M. Ceccarelli and M. Marchi, The Journal of Physical Chemistry B **107** (6), 1423-1431 (2003).

102. M. R. Gunner, A. Nicholls and B. Honig, The Journal of Physical Chemistry **100** (10), 4277-4291 (1996).

103. M. A. Steffen, K. Lao and S. G. Boxer, Science **264** (5160), 810-816 (1994).

104. J. Mongan, D. A. Case and J. A. McCAMMON, Journal of Computational Chemistry **25** (16), 2038-2048 (2004).

105. U. Börjesson and P. H. Hünenberger, The Journal of Chemical Physics **114**, 9706 (2001).

106. J. Khandogin and C. L. Brooks, Biophysical Journal **89** (1), 141-157 (2005).

107. Y. Song, J. Mao and M. Gunner, Journal of Computational Chemistry **30** (14), 2231-2247 (2009).

108. J. D. Bryngelson, J. N. Onuchic, N. D. Socci, et al., Proteins: Structure, Function, and Bioinformatics **21** (3), 167-195 (1995).

109. H. S. Chan and K. A. Dill, Proteins: Structure, Function, and Bioinformatics **30** (1), 2-33 (1998).

110. Y. Duan and P. A. Kollman, Science **282** (5389), 740-744 (1998).

111. J. L. Klepeis, K. Lindorff-Larsen, R. O. Dror, et al., Current Opinion in Structural Biology **19** (2), 120-127 (2009).

112. D. E. Chandler, J. Hsin, C. B. Harrison, et al., Biophysical Journal **95** (6), 2822-2836 (2008).

113. G. Groenhof, M. Bouxin-Cademartory, B. Hess, et al., Journal of the American Chemical Society **126** (13), 4228-4233 (2004).

114. X. S. Xie, The Journal of Chemical Physics **117** (24), 11024-11032 (2002).

115. H. Neuweiler and M. Sauer, Current Pharmaceutical Biotechnology **5**, 285-298 (2004).

116. C. Hofmann, T. J. Aartsma, H. Michel, et al., Proceedings of the National Academy of Sciences of the United States of America **100** (26), 15534-15538 (2003).

117. K. J. Hellingwerf, J. Hendriks and T. Gensch, The Journal of Physical Chemistry A **107** (8), 1082-1094 (2003).

118. R. R. Birge, Annual Review of Physical Chemistry **41** (1), 683-733 (1990).

119. F. Gai, K. C. Hasson, J. C. McDonald, et al., Science **279** (5358), 1886-1891 (1998).

120. F. Andel, J. C. Lagarias and R. A. Mathies, Biochemistry **35** (50), 15997-16008 (1996).

121. H. N. Chapman, P. Fromme, A. Barty, et al., Nature **470** (7332), 73-77 (2011).

122. F. Schotte, M. Lim, T. A. Jackson, et al., Science **300** (5627), 1944-1947 (2003).

123. H. Ihee, S. Rajagopal, V. Šrajer, et al., Proceedings of the National Academy of Sciences of the United States of America **102** (20), 7145-7150 (2005).

124. R. E. Blankenship, R. Feick, B. D. Bruce, et al., Journal of Cellular Biochemistry **22** (4), 251-261 (1983).

125. J. Deisenhofer, O. Epp, I. Sinning, et al., Journal of Molecular Biology **246** (3), 429-457 (1995).

126. B. Pierson and R. Castenholz, The Prokaryotes−A Handbook on the Biology of Bacteria: Ecophysiology, Isolation, Identification, Applications. Springer-Verlag, Berlin, Heidelberg and New York, 3754−3774 (1992).

127. Y. A. Ovchinnikov, N. G. Abdulaev, B. E. Shmuckler, et al., Febs Letters **232** (2), 364-368 (1988).

128. M. Becker, V. Nagarajan, D. Middendorf, et al., Biochimica Et Biophysica Acta **1057** (3), 299-312 (1991).

129. C. Kirmaier and D. Holten, Photosynthesis Research **13** (3), 225-260 (1987).

130. N. Woodbury and J. Allen, (1995), pp. 527-557.

131. M. Du, S. J. Rosenthal, X. Xie, et al., Proceedings of the National Academy of Sciences **89** (18), 8517-8521 (1992).

132. C. Kirmaier, R. E. Blankenship and D. Holten, Biochimica et Biophysica Acta (BBA) - Bioenergetics **850** (2), 275-285 (1986).

133. M. Volk, G. Aumeier, T. Langenbacher, et al., Journal of Physical Chemistry B **102** (4), 735-751 (1998).

134. A. M. Collins, C. Kirmaier, D. Holten, et al., Biochimica et Biophysica Acta (BBA) - Bioenergetics **1807** (3), 262-269 (2011).

135. Y. Y. Xin, S. Lin and R. E. Blankenship, Journal of Physical Chemistry A **111** (38), 9367-9373 (2007).

136. P. Hamm, K. A. Gray, D. Oesterhelt, et al., Biochimica et biophysica acta. Bioenergetics **1142** (1-2), 99-105 (1993).

137. N. W. Woodbury, W. W. Parson, M. R. Gunner, et al., Biochimica et Biophysica Acta (BBA) - Bioenergetics **851** (1), 6-22 (1986).

138. N. W. T. Woodbury and W. W. Parson, Biochimica et Biophysica Acta (BBA) - Bioenergetics **767** (2), 345-361 (1984).

139. N. J. Cherepy, A. R. Holzwarth and R. A. Mathies, Biochemistry **34** (15), 5288-5293 (1995).

140. S. Dasgupta, T. G. Spiro, C. K. Johnson, et al., Biochemistry **24** (20), 5295-5297 (1985).

141. S. A. Asher and J. Murtaugh, Journal of the American Chemical Society **105** (25), 7244-7251 (1983).

142. G. Schweitzer, M. Hucke, K. Griebenow, et al., Chemical Physics Letters **190** (1-2), 149-154 (1992).

143. W. Doster, S. Cusack and W. Petry, Nature **337** (6209), 754-756 (1989).

144. J. J. Dechter, D. E. Axelson, A. Dekmezian, et al., Journal of Polymer Science: Polymer Physics Edition **20** (4), 641-650 (1982).

145. H. Frauenfelder, G. Chen, J. Berendzen, et al., Proceedings of the National Academy of Sciences **106** (13), 5129-5134 (2009).

146. D. N. LeBard and D. V. Matyushov, The Journal of Physical Chemistry B **113** (36), 12424-12437 (2009).

147. G. Hartwich, H. Lossau, M. E. Michel-Beyerle, et al., The Journal of Physical Chemistry B **102** (19), 3815-3820 (1998).

148. P. Huppman, T. Arlt, H. Penzkofer, et al., **82** (6), 3186-3197 (2002).

149. Y. Jia, T. J. DiMagno, C. K. Chan, et al., The Journal of Physical Chemistry **97** (50), 13180-13191 (1993).

150. E. Katilius, Z. Katiliene, S. Lin, et al., The Journal of Physical Chemistry B **106** (6), 1471-1475 (2002).

151. M. Volk, G. Scheidel, A. Ogrodnik, et al., Biochimica Et Biophysica Acta **1058** (2), 217-224 (1991).

152. M. Pudlak and R. Pincak, Journal of Biological Physics **36** (3), 273-289 (2010).

153. D. Kleinfeld, M. Y. Okamura and G. Feher, Biochemistry **23** (24), 5780-5786 (1984).

154. F. Muh, J. C. Williams, J. P. Allen, et al., Biochemistry **37** (38), 13066-13074 (1998).

155. J. M. Peloquin, C. A. Violette, H. A. Frank, et al., Biochemistry **29** (20), 4892-4898 (1990).

156. A. Ivancich, M. Lutz and T. A. Mattioli, Biochemistry **36** (11), 3242-3253 (1997).

157. C.-K. Chan, L. X-Q Chen, T. J. DiMagno, et al., Chemical Physics Letters **176** (3-4), 366-372 (1991).

158. A. K. W. Taguchi, S. Lin, J. A. Jackson, et al., Biochemistry **39** (48), 14787-14798 (2000).

159. E. Bellacchio and K. Sauer, The Journal of Physical Chemistry B **103** (12), 2279-2290 (1999).

160. D. N. LeBard and D. V. Matyushov, Physical Review E **78** (6), 061901 (2008).

161. B. N. Dominy, D. Perl, F. X. Schmid, et al., Journal of Molecular Biology **319** (2), 541-554 (2002).

162. D. Matyushov and A. Morozov, Arxiv preprint arXiv:1011.1023 (2010).

163. D. N. LeBard, V. Kapko and D. V. Matyushov, The Journal of Physical Chemistry B **112** (33), 10322-10342 (2008).

164. A. G. Yakovlev, L. G. Vasilieva, A. Y. Shkuropatov, et al., The Journal of Physical Chemistry A **107** (40), 8330-8338 (2003).

165. R. A. Marcus, The Journal of Chemical Physics **24** (5), 979-989 (1956).

166. B. Bagchi, Annu. Rep. Prog. Chem., Sect. C: Phys. Chem. **99** (0), 127-175 (2003).

167. H. Wang, S. Lin, E. Katilius, et al., The Journal of Physical Chemistry B **113** (3), 818-824 (2008).

168. K. Gibasiewicz and M. Pajzderska, The Journal of Physical Chemistry B **112** (6), 1858-1865 (2008).

169. A. L. M. Haffa, S. Lin, E. Katilius, et al., The Journal of Physical Chemistry B **106** (29), 7376-7384 (2002).

170. J. O. Goldsmith and S. G. Boxer, Biochimica et Biophysica Acta (BBA)-Bioenergetics **1276** (3), 171-175 (1996).

171. A. L. M. Haffa, S. Lin, J. C. Williams, et al., The Journal of Physical Chemistry B **108** (1), 4-7 (2003).

172. R. E. Georgescu, E. G. Alexov and M. R. Gunner, Biophysical journal **83** (4), 1731-1748 (2002).

173. Y. Song, J. Mao and M. R. Gunner, Journal of Computational Chemistry **30** (14), 2231-2247 (2009).

174. A. Nicholls and B. Honig, Journal of Computational Chemistry **12** (4), 435-445 (1991).

175. J. Breton, J. Martin, J. Lambry, et al., Structure and Function of Bacterial Photosynthetic Reaction Centers, 293-302 (1990).

176. L. M. McDowell, D. Gaul, C. Kirmaier, et al., Biochemistry **30** (34), 8315-8322 (1991).

177. C. Kirmaier, D. Holten, E. J. Bylina, et al., Proceedings of the National Academy of Sciences **85** (20), 7562 (1988).

178. C. Kirmaier, D. Holten and W. W. Parson, Biochimica et Biophysica Acta (BBA) - Bioenergetics **810** (1), 33-48 (1985).

179. C.-K. Tang, J. C. Williams, A. K. W. Taguchi, et al., Biochemistry **38** (27), 8794-8799 (1999).

180. M. Volk, G. Aumeier, T. Langenbacher, et al., The Journal of Physical Chemistry B **102** (4), 735-751 (1998).

181. C. Kirmaier, D. Gaul, R. DeBey, et al., Science **251** (4996), 922-927 (1991).

182. T. Arlt, B. Dohse, S. Schmidt, et al., Biochemistry **35** (28), 9235-9244 (1996).

183. C. Kirmaier, L. Laporte, C. C. Schenck, et al., The Journal of Physical Chemistry **99** (21), 8910-8917 (1995).

184. K. Gibasiewicz, M. Pajzderska, M. Ziółek, et al., The Journal of Physical Chemistry B **113** (31), 11023-11031 (2009).

185. A. Ogrodnik, W. Keupp, M. Volk, et al., The Journal of Physical Chemistry **98** (13), 3432-3439 (1994).

186. J. M. Peloquin, J. C. Williams, X. Lin, et al., Biochemistry **33** (26), 8089-8100 (1994).

187. V. Nagarajan, W. W. Parson, D. Davis, et al., Biochemistry **32** (46), 12324-12336 (1993).

188. W. Holzapfel, U. Finkele, W. Kaiser, et al., Chemical Physics Letters **160** (1), 1-7 (1989).

189. I. H. M. van Stokkum, D. S. Larsen and R. van Grondelle, Biochimica et Biophysica Acta (BBA) - Bioenergetics **1657** (2−3), 82-104 (2004).

190. I. H. M. van Stokkum, L. M. P. Beekman, M. R. Jones, et al., Biochemistry **36** (38), 11360-11368 (1997).

191. L. Laporte, C. Kirmaier, C. C. Schenck, et al., Chemical Physics **197** (3), 225-237 (1995).

192. G. R. Grimsley, J. M. Scholtz and C. N. Pace, Protein Science **18** (1), 247-251 (2009).

193. M. H. M. Olsson, C. R. Søndergaard, M. Rostkowski, et al., Journal of Chemical Theory and Computation **7** (2), 525-537 (2011).

194. C. R. Søndergaard, M. H. M. Olsson, M. Rostkowski, et al., Journal of Chemical Theory and Computation **7** (7), 2284-2295 (2011).

195. N. P. Pawlowicz, R. van Grondelle, I. H. M. van Stokkum, et al., Biophysical journal **95** (3), 1268-1284 (2008).

196. W. Liptay, Excited states **1**, 129-229 (1974).

197. W. Liptay, Berichte der Bunsengesellschaft für physikalische Chemie **80** (3), 207-217 (1976).

198. G. U. Bublitz and S. G. Boxer, Annual Review of Physical Chemistry **48** (1), 213-242 (1997).

199. M. Lösche, G. Feher and M. Y. Okamura, Proceedings of the National Academy of Sciences **84** (21), 7537-7541 (1987).

200. D. J. Lockhart and S. G. Boxer, Biochemistry **26** (3), 664-668 (1987).

201. S. L. Hammes, L. Mazzola, S. G. Boxer, et al., Proceedings of the National Academy of Sciences **87** (15), 5682 (1990).

202. D. S. Gottfried, M. A. Steffen and S. G. Boxer, Science **251** (4994), 662-665 (1991).

203. D. W. Pierce and S. G. Boxer, Biophysical Journal **68** (4), 1583-1591 (1995).

204. G. Bublitz, B. A. King and S. G. Boxer, Journal of the American Chemical Society **120** (36), 9370-9371 (1998).

205. L. N. Silverman, D. Spry, S. G. Boxer, et al., The Journal of Physical Chemistry A **112** (41), 10244-10249 (2008).

206. A. T. Fafarman, P. A. Sigala, J. P. Schwans, et al., Proceedings of the National Academy of Sciences **109** (6), E299-E308 (2012).

207. M. Lösche, G. Feher and M. Okamura, Proceedings of the National Academy of Sciences **84** (21), 7537 (1987).

208. H. Labhart, in *Advances in Chemical Physics* (John Wiley & Sons, Inc., 2007), pp. 179-204.

209. S. Krawczyk and A. Daniluk, Chemical Physics Letters **236** (4−5), 431-437 (1995).

210. I. Chang, Nonemissive Electrooptic Displays, 155-196 (1976).

211. J. R. Bolton, R. K. Clayton and D. W. Reed, Photochemistry and Photobiology **9** (3), 209-218 (1969).

212. B. Neupane, P. Jaschke, R. Saer, et al., The Journal of Physical Chemistry B **116** (10), 3457-3466 (2012).

213. K. Lao, L. J. Moore, H. Zhou, et al., The Journal of Physical Chemistry **99** (2), 496-500 (1995).

214. X. Xie and J. D. Simon, Biochimica et Biophysica Acta (BBA)-Bioenergetics **1057** (1), 131-139 (1991).

215. A. Trifonov, I. Buchvarov, A. Lohr, et al., Review of Scientific Instruments **81**, 043104 (2010).

216. D. S. Kliger, E. Chen and R. A. Goldbeck, Comprehensive Chiroptical Spectroscopy, 179-201 (2012).

217. H. Rhee and M. Cho, Comprehensive Chiroptical Spectroscopy, 203-219 (2012).

218. C. Provenzano, P. Pagliusi, A. Mazzulla, et al., Opt. Lett. **35** (11), 1822-1824 (2010).

219. D.-H. Kwon, P. L. Werner and D. H. Werner, Opt. Express **16** (16), 11802-11807 (2008).

220. T. Harada, Y. Miyoshi and R. Kuroda, Review of Scientific Instruments **80** (4), 046101-046103 (2009).

221. Y. Shindo, S. Shouno and S. Maeda, Review of Scientific Instruments **66** (4), 3079-3080 (1995).

222. Y.-X. Wen, E. Chen, J. W. Lewis, et al., Review of Scientific Instruments **67** (9), 3010-3016 (1996).

223. R. M. Esquerra, J. W. Lewis and D. S. Kliger, Review of Scientific Instruments **68** (3), 1372-1376 (1997).

224. S. Wenzel and V. Buss, Review of Scientific Instruments **68** (4), 1886-1888 (1997).

225. L. Mangot, G. Taupier, M. Romeo, et al., Optics letters **35** (3), 381-383 (2010).

226. D. W. Reed and B. Ke, Journal of Biological Chemistry **248** (9), 3041-3045 (1973).

227. E. Condon, Reviews of Modern Physics **9** (4), 432-457 (1937).

228. C. Luo, K. Reimann, M. Woerner, et al., Applied Physics A: Materials Science & Processing **78** (4), 435-440 (2004).

229. R. M. Koehl, S. Adachi and K. A. Nelson, The Journal of Physical Chemistry A **103** (49), 10260-10267 (1999).

APPENDIX A

ATOMIC CHARGE OF THE SPECIAL DIMER (CHARGE=+1.0)

The +1.0 atomic charge of the special dimer P is distributed onto the bacteriochlorophylls on two branches (P_L and P_M) in a ~2:1 ratio. The structural coordinates of the entire dimer (both bacteriochlorophylls) have been use as the input for open shell DFT calculation (charge=1.0, multiplicity=2), using B3LYP hybrid functional together with a 6-31G* basis set. The optimization and ESP potential calculation was carried out by Gaussian 09, B01. RESP charge fit was perfomred by resp module in Ambertool (written by Ian Gould). The molecular dynamics simulation force field parameter files in AMBER format is listed as below:

```
RESIDUE  plc ( Total Charge =   0.609748 )
atoms
group
mg     K0     0.711893
group
cha    K3     -0.096411
group
chb    K2    -0.186973
hb     J5     0.154731
group
chc    K2    -0.102474
hc     J5     0.121535
group
chd    K2    -0.109348
hd     J5     0.108136
group
na     ns      -0.022585
c1a    K5    0.020146
c4a    K5    -0.057924
group
c2a    L5     -0.022919
h2a    hc      0.080121
group
c3a    L5     0.000101
h3a    hc     0.093630
group
cma    L7    -0.107684
hma1   hc      0.054246
hma2   hc      0.054246
hma3   hc      0.054246
```

```
group
caa     L6     -0.104705
haa1    hc       0.046234
haa2    hc       0.046234
group
cba     L6     -0.051064
hba1    hc       0.051880
hba2    hc       0.051880
group
cga     L1      0.502934
o1a     L3     -0.422202
group
o2a     L2     -0.450324
group
nb      K1     -0.109056
c1b     K9     -0.028966
c4b     K6      -0.067562
group
c2b     K4      0.022597
c3b     K4     -0.070693
group
cmb     L7     -0.272128
hmb1    hc       0.114155
hmb2    hc       0.114155
hmb3    hc       0.114155
group
cab     L4      0.387564
obb     L3     -0.350158
group
cbb     L7     -0.210450
hbb1    hc       0.082206
hbb2    hc       0.082206
hbb3    hc       0.082206
group
nc      ns       -0.141438
c1c     K5     -0.027702
c4c     K5     -0.059348
group
c2c     L5      -0.007328
h2c     hc      0.091450
group
c3c     L5      -0.010567
h3c     hc       0.097648
group
cmc     L7     -0.151274
hmc1    hc       0.066117
hmc2    hc       0.066117
hmc3    hc       0.066117
group
cac     L6      0.004813
```

```
hac1   hc      0.025859
hac2   hc      0.025859
group
cbc    L7    -0.114326
hbc1   hc      0.038648
hbc2   hc      0.038648
hbc3   hc      0.038648
group
nd     K1     -0.162042
c1d    K7    -0.041400
c4d    K8    -0.118405
group
c2d    K4     0.064306
c3d    K4    -0.011474
group
cmd    L7    -0.193103
hmd1   hc      0.097948
hmd2   hc      0.097948
hmd3   hc      0.097948
group
cad    L0     0.354734
obd    L3    -0.381439
group
cbd    L5    -0.064705
hbd    hc      0.109492
group
cgd    L1     0.551745
o1d    L3    -0.388899
group
o2d    L2    -0.361371
group
ced    L7     -0.000148
hed1   hc      0.083986
hed2   hc      0.083986
hed3   hc      0.083986
#
group
c1     L6     0.492381
h11    hc     -0.038739
h12    hc     -0.038739
group
c2     J0    -0.342
h21    J5     0.133
group
c3     L9     0.055
group
c4     L7    -0.301
h41    hc      0.092666
h42    hc      0.092667
h43    hc      0.092667
```

```
group
c5     L6     0.098
h51    hc      0.0075
h52    hc      0.0075
group
c6     L6    -0.18
h61    hc      0.09
h62    hc      0.09
group
c7     L6    -0.18
h71    hc      0.09
h72    hc      0.09
group
c8     L5    -0.09
h81    hc      0.09
group
c9     L7    -0.27
h91    hc      0.09
h92    hc      0.09
h93    hc      0.09
group
c10    L6    -0.18
h101   hc      0.09
h102   hc      0.09
group
c11    L6    -0.18
h111   hc      0.09
h112   hc      0.09
group
c12    L6    -0.18
h121   hc      0.09
h122   hc      0.09
group
c13    L5    -0.09
h131   hc      0.09
group
c14    L7    -0.27
h141   hc      0.09
h142   hc      0.09
h143   hc      0.09
group
c15    L6    -0.18
h151   hc      0.09
h152   hc      0.09
group
c16    L6    -0.18
h161   hc      0.09
h162   hc      0.09
group
c17    L6    -0.18
```

```
h171   hc      0.09
h172   hc      0.09
group
c18    L5    -0.09
h181   hc      0.09
group
c19    L7    -0.27
h191   hc      0.09
h192   hc      0.09
h193   hc      0.09
group
c20    L7    -0.27
h201   hc      0.09
h202   hc      0.09
h203   hc      0.09
end


bonds
nb   mg     nc   mg     nd   mg     na   mg
nb   c1b    c1b  c2b    c2b  c3b    c3b  c4b
c4b  nb
nc   c1c    c1c  c2c    c2c  c3c    c3c  c4c
c4c  nc
nd   c1d    c1d  c2d    c2d  c3d    c3d  c4d
c4d  nd
na   c1a    c1a  c2a    c2a  c3a    c3a  c4a
c4a  na
c4b  chc    chc  c1c    c4c  chd    chd  c1d
c4d  cha    cha  c1a    c4a  chb    chb  c1b
chb  hb     chc  hc     chd  hd
c2b  cmb    cmb  hmb1   cmb  hmb2   cmb  hmb3
c3b  cab    cab  obb
cab  cbb    cbb  hbb1   cbb  hbb2   cbb  hbb3
c2c  h2c    c2c  cmc
cmc  hmc1   cmc  hmc2   cmc  hmc3
c3c  h3c    c3c  cac    cac  hac1   cac  hac2
cac  cbc    cbc  hbc1   cbc  hbc2   cbc  hbc3
c2d  cmd    cmd  hmd1   cmd  hmd2   cmd  hmd3
c3d  cad    cad  obd     cad  cbd    cbd  cha
cbd  hbd    cbd  cgd    cgd  o1d    cgd  o2d
o2d  ced    ced  hed1   ced  hed2   ced  hed3
c3a  h3a   c3a  cma
cma  hma1   cma  hma2   cma  hma3
c2a  h2a   c2a  caa    caa  haa1   caa  haa2
caa  cba    cba  hba1   cba  hba2
cba  cga    cga  o1a    cga  o2a
o2a  c1     c1   h11    c1   h12
#
c1   c2     c2   h21    c2   c3
```

```
c3   c4     c4   h41    c4   h42    c4   h43
c3   c5     c5   h51    c5   h52
c5   c6     c6   h61    c6   h62
c6   c7     c7   h71    c7   h72
c7   c8     c8   h81
c8   c9     c9   h91    c9   h92    c9   h93
c8   c10    c10  h101   c10  h102
c10  c11    c11  h111   c11  h112
c11  c12    c12  h121   c12  h122
c12  c13    c13  h131
c13  c14    c14  h141   c14  h142   c14  h143
c13  c15    c15  h151   c15  h152
c15  c16    c16  h161   c16  h162
c16  c17    c17  h171   c17  h172
c17  c18    c18  h181
c18  c19    c19  h191   c19  h192   c19  h193
c18  c20    c20  h201   c20  h202   c20  h203
end

imphd
#
c1b  c4b  nb   mg
c2b  nb   c1b  chb
c1b  c3b  c2b  cmb
c4b  c2b  c3b  cab
c3b  nb   c4b  chc
#
c1c  nc   c4c  mg
nc   c2c  c1c  chc
nc   c3c  c4c  chd
#
c1d  c4d  nd   mg
c2d  nd   c1d  chd
c1d  c3d  c2d  cmd
c4d  c2d  c3d  cad
c3d  nd   c4d  cha
#
c1a  na   c4a  mg
na   c2a  c1a  cha
na   c3a  c4a  chb
#
c4d  cbd  cha  c1a
c1b  c4a  chb  hb
c1c  c4b  chc  hc
c1d  c4c  chd  hd
#
c3b  cbb  cab  obb
c3d  cbd  cad  obd
cbd  cgd  o1d  o2d
cba  cga  o1a  o2a
```

```
#
c3   c1   h21  c2
c5   c2   c4   c3
end

termatom * *
RESIDUE_END

RESIDUE  pmc ( Total Charge =   0.39025 )
atoms
group
mg     K0     0.756135
group
cha    K3     -0.039836
group
chb    K2    -0.134066
hb     J5     0.105199
group
chc    K2    -0.123113
hc     J5     0.103454
group
chd    K2    -0.102564
hd     J5     0.133066
group
na     ns      -0.091492
c1a    K5    -0.060072
c4a    K5    -0.048160
group
c2a    L5     -0.041136
h2a    hc      0.110103
group
c3a    L5     0.000205
h3a    hc     0.087423
group
cma    L7    -0.149653
hma1   hc      0.069955
hma2   hc      0.069955
hma3   hc      0.069955
group
caa    L6    -0.137319
haa1   hc      0.025921
haa2   hc      0.088476
group
cba    L6    -0.020510
hba1   hc      0.032095
hba2   hc      0.032095
group
cga    L1     0.634271
o1a    L3    -0.498079
group
```

```
o2a     L2     -0.534018
group
nb      K1     -0.086385
c1b     K9     -0.069196
c4b     K6      -0.126226
group
c2b     K4      0.017122
c3b     K4     -0.007016
group
cmb     L7     -0.071088
hmb1    hc       0.055701
hmb2    hc       0.055701
hmb3    hc       0.055701
group
cab     L4      0.293220
obb     L3     -0.355384
group
cbb     L7     -0.045590
hbb1    hc       0.046112
hbb2    hc       0.046112
hbb3    hc       0.046112
group
nc      ns       -0.103566
c1c     K5     -0.020869
c4c     K5     -0.099310
group
c2c     L5      -0.027434
h2c     hc      0.088556
group
c3c     L5      0.024166
h3c     hc       0.077026
group
cmc     L7     -0.199462
hmc1    hc       0.073207
hmc2    hc       0.073207
hmc3    hc       0.073207
group
cac     L6      0.016825
hac1    hc       0.015495
hac2    hc       0.015495
group
cbc     L7     -0.135142
hbc1    hc       0.041522
hbc2    hc       0.041522
hbc3    hc       0.041522
group
nd      K1      -0.231396
c1d     K7     -0.006634
c4d     K8     -0.119222
group
```

```
c2d    K4     0.030211
c3d    K4    -0.000845
group
cmd    L7    -0.225584
hmd1   hc      0.108863
hmd2   hc      0.108863
hmd3   hc      0.108863
group
cad    L0     0.288650
obd    L3    -0.345192
group
cbd    L5    -0.044320
hbd    hc      0.065713
group
cgd    L1     0.623730
o1d    L3    -0.470385
group
o2d    L2    -0.336361
group
ced    L7     -0.025965
hed1   hc      0.093710
hed2   hc      0.093710
hed3   hc      0.093710
#
group
c1     L6     0.551234
h11    hc     -0.048128
h12    hc     -0.048128
group
c2     J0    -0.342
h21    J5     0.133
group
c3     L9     0.055
group
c4     L7    -0.301
h41    hc      0.092666
h42    hc      0.092667
h43    hc      0.092667
group
c5     L6     0.098
h51    hc      0.0075
h52    hc      0.0075
group
c6     L6    -0.18
h61    hc      0.09
h62    hc      0.09
group
c7     L6    -0.18
h71    hc      0.09
h72    hc      0.09
```

```
group
c8     L5    -0.09
h81    hc      0.09
group
c9     L7    -0.27
h91    hc      0.09
h92    hc      0.09
h93    hc      0.09
group
c10    L6    -0.18
h101   hc      0.09
h102   hc      0.09
group
c11    L6    -0.18
h111   hc      0.09
h112   hc      0.09
group
c12    L6    -0.18
h121   hc      0.09
h122   hc      0.09
group
c13    L5    -0.09
h131   hc      0.09
group
c14    L7    -0.27
h141   hc      0.09
h142   hc      0.09
h143   hc      0.09
group
c15    L6    -0.18
h151   hc      0.09
h152   hc      0.09
group
c16    L6    -0.18
h161   hc      0.09
h162   hc      0.09
group
c17    L6    -0.18
h171   hc      0.09
h172   hc      0.09
group
c18    L5    -0.09
h181   hc      0.09
group
c19    L7    -0.27
h191   hc      0.09
h192   hc      0.09
h193   hc      0.09
group
c20    L7    -0.27
```

```
h201   hc       0.09
h202   hc       0.09
h203   hc       0.09
end


bonds
nb   mg     nc   mg     nd   mg     na   mg
nb   c1b    c1b  c2b    c2b  c3b    c3b  c4b
c4b  nb
nc   c1c    c1c  c2c    c2c  c3c    c3c  c4c
c4c  nc
nd   c1d    c1d  c2d    c2d  c3d    c3d  c4d
c4d  nd
na   c1a    c1a  c2a    c2a  c3a    c3a  c4a
c4a  na
c4b  chc    chc  c1c    c4c  chd    chd  c1d
c4d  cha    cha  c1a    c4a  chb    chb  c1b
chb  hb     chc  hc     chd  hd
c2b  cmb    cmb  hmb1   cmb  hmb2   cmb  hmb3
c3b  cab    cab  obb
cab  cbb    cbb  hbb1   cbb  hbb2   cbb  hbb3
c2c  h2c    c2c  cmc
cmc  hmc1   cmc  hmc2   cmc  hmc3
c3c  h3c    c3c  cac    cac  hac1   cac  hac2
cac  cbc    cbc  hbc1   cbc  hbc2   cbc  hbc3
c2d  cmd    cmd  hmd1   cmd  hmd2   cmd  hmd3
c3d  cad    cad  obd     cad  cbd    cbd  cha
cbd  hbd    cbd  cgd    cgd  o1d    cgd  o2d
o2d  ced    ced  hed1   ced  hed2   ced  hed3
c3a  h3a   c3a  cma
cma  hma1   cma  hma2   cma  hma3
c2a  h2a   c2a  caa    caa  haa1   caa  haa2
caa  cba    cba  hba1   cba  hba2
cba  cga    cga  o1a    cga  o2a
o2a  c1     c1   h11    c1   h12
#
c1   c2     c2   h21    c2   c3
c3   c4     c4   h41    c4   h42    c4   h43
c3   c5     c5   h51    c5   h52
c5   c6     c6   h61    c6   h62
c6   c7     c7   h71    c7   h72
c7   c8     c8   h81
c8   c9     c9   h91    c9   h92    c9   h93
c8   c10    c10  h101   c10  h102
c10  c11    c11  h111   c11  h112
c11  c12    c12  h121   c12  h122
c12  c13    c13  h131
c13  c14    c14  h141   c14  h142   c14  h143
c13  c15    c15  h151   c15  h152
```

```
c15  c16    c16  h161   c16  h162
c16  c17    c17  h171   c17  h172
c17  c18    c18  h181
c18  c19    c19  h191   c19  h192   c19  h193
c18  c20    c20  h201   c20  h202   c20  h203
end

imphd
#
c1b  c4b  nb   mg
c2b  nb   c1b  chb
c1b  c3b  c2b  cmb
c4b  c2b  c3b  cab
c3b  nb   c4b  chc
#
c1c  nc   c4c  mg
nc   c2c  c1c  chc
nc   c3c  c4c  chd
#
c1d  c4d  nd   mg
c2d  nd   c1d  chd
c1d  c3d  c2d  cmd
c4d  c2d  c3d  cad
c3d  nd   c4d  cha
#
c1a  na   c4a  mg
na   c2a  c1a  cha
na   c3a  c4a  chb
#
c4d  cbd  cha  c1a
c1b  c4a  chb  hb
c1c  c4b  chc  hc
c1d  c4c  chd  hd
#
c3b  cbb  cab  obb
c3d  cbd  cad  obd
cbd  cgd  o1d  o2d
cba  cga  o1a  o2a
#
c3   c1   h21  c2
c5   c2   c4   c3
end

termatom * *
RESIDUE_END
```

APPENDIX B

DEFINITION OF RMSD

Root Mean Squared Deviation (RMSD)

The RMSD between two structures is defined as

$$RMSD_{\alpha}(t) = \sqrt{\frac{\sum_{\alpha=1}^{N_\alpha}(\overrightarrow{r_\alpha}(t) - \left\langle \overrightarrow{r_\alpha} \right\rangle)^2}{N_\alpha}}$$

Where α is referring to the certain atom within the structure being compared (atom index), N_α is the total atom number of the subset. $\overrightarrow{r_\alpha(t)}$ is the position vector of atom α at certain moment. $\left\langle \overrightarrow{r_\alpha} \right\rangle$ is the position vector average over the simulation time, i.e. if time is discretized, it is expressed as follows:

$$\left\langle \overrightarrow{r_\alpha} \right\rangle = \frac{1}{N_t}\sum_{j=1}^{N_t} \overrightarrow{r_\alpha}(t_j)$$

In this thesis, the average position vector $\left\langle \overrightarrow{r_\alpha} \right\rangle$ is replaced by the initially crystal structure or an optimized mutated structure before the simulation, that is:

$$RMSD_{\alpha}(t) = \sqrt{\frac{\sum_{\alpha=1}^{N_\alpha}(\overrightarrow{r_\alpha}(t) - \overrightarrow{r_0})^2}{N_\alpha}}$$

BIOGRAPHICAL SKETCH

The author was born in 1982. By the time he wrote this thesis, he was 30 years old. He first received a B.S degree in applied physics in Nanjing University of Science and Technology (Nanjing, China). Then he entered Fudan University (Shanghai, China) and worked for his master's in condensed matter physics. He received a M.S. degree there in 2007. Also in 2007, he came to USA as a physics PhD student and chose to work with Dr. Neal Woodbury in the photosynthetic electron transfer field.